Primitive Magmas of the Earth and Moon: A Petrologic Investigation of Magma Genesis and Evolution

by

JAY ARTHUR BARR

B.A. Geology
Colgate University, 2004

Submitted to the Department of

EARTH, ATMOSPHERIC AND PLANETARY SCIENCES

In Partial Fulfillment of the Requirements for the Degree of

DOCTOR OF PHILOSOPHY

In

GEOCHEMISTRY

at the

MASSACHUSETTS INSTITUTE OF TECHNOLOGY

SEPTEMBER 2010

Signature of Author _____
Department of Earth, Atmosheric and Planetary Sciences
August 9, 2010

Certified by _____
Timothy L. Grove
Thesis Supervisor

Accepted by _____
Maria T. Zuber
Department Chairperson

Primitive Magmas of the Earth and Moon: A Petrologic Investigation of Magma Genesis and Evolution

by

JAY ARTHUR BARR

Submitted to the Department of Earth, Atmospheric and Planetary Sciences
on September 6, 2010 in Partial Fulfillment of the
Requirements for the Degree of Doctor of Philosophy in
Geochemistry

ABSTRACT

Field studies, major and trace element geochemistry, isotopes, petrography, phase equilibrium experiments and thermodynamics are used investigate and understand primitive melts from the Earth and the Moon. Chapter 1 investigates spinifex orthopyroxene compositions from the komatiites of Commondale, South Africa, and uses phase equilibrium experiments to illustrate that the Commondale Komatiites were hydrous magmas when they were emplaced. Hydrous komatiites provide evidence for the existence of subduction zone volcanism during the Archean, and decreases the temperature required to explain komatiites volcanism, which is the major physical evidence used to determine the mantle potential temperature of the Archean. Chapter 2 uses phase equilibrium experiments investigate the origin of the Apollo 15 green glasses from the Moon. Garnet-lherzolite saturated experiments are used to calibrate a melting algorithm used to estimate the chemical compositions of melts of a primordial lunar mantle. Mixing models are used to reproduce the Apollo 15 green glass compositions. These models are consistent with primordial melts assimilating late stage lunar magma ocean cumulates to produce the green glasses. This provides evidence for the magma overturn hypothesis, as well as evidence that the lunar magma ocean may not have been whole moon. Chapter 3 uses phenocryst petrology, Os-isotopes, major and trace element geochemistry and petrography to argue for the formation of primitive magnesian andesites of Mt. Shasta and Mt. Lassen as primary mantle melts. Recent proposals that primitive magnesian andesites form by mixing dacites with subvolcanic peridotite are disproven. Samples of these lavas from newly discovered localities provide clear evidence for a mantle origin for these melts. Understanding the primitive melts present in the Cascade volcanoes will yield greater insight into the mantle processes involved in the plumbing of the sub-arc mantle. Chapter 4 develops a ternary regular solution model for Au-Pd-Fe alloys and uses this with Fe-exchange experiments to model the dependence of alloy composition on the oxygen fugacity. Au-Pd alloy capsules are essential to hydrous phase equilibrium studies at high-pressure and high-temperature, and the use of this model allows for the quantification of the oxygen fugacity of these experiments without compromising sample volume.

Thesis Supervisor: Timothy Grove
Title: Professor of Geology

Acknowledgements

My graduate career has benefitted greatly from interactions with outstanding faculty, researchers at MIT and WHOI. Among these individuals I owe particular gratitude to members of my thesis committee: Lindy Elkins-Tanton, Sam Bowring, Dan Shim, Marc Hirschmann (U. Minn.), and Tim Grove. Fred Frey and Nobu Shimizu provided valuable assistance during my pre-generals years, and Oliver Jagoutz, Ben Weiss, Tanja Bosak, and Taylor Perron who have provided a wonderful source of enthusiasm and lively discussion about a variety of geologic topics. Many postdocs have also helped me along my way. Etienne Medard proved to be a wonderful source of experimental petrology knowledge as well as enthusiasm for mineralogy. The years spent working along side him greatly helped in shaping my careful and meticulous laboratory habits. He was a great friend and a great mentor. Time spent with Pierre Bouihol, Matt Rioux, Brent Grocholski, Nicole Keller, Romain Meyer, Zhengrong Wang, Javier Santillan, and Sandeep Rekhi were always entertaining and enjoyable. Discussions and assistance rendered by Jim Crowley, Frank Dudas and Jahan Ramezani have been of great value and it has always been a pleasure having them around. I must also thank Sam Bowring and Oliver Jagoutz for the field trip opportunities they provided to me while I was supposed to be diligently working in the lab. I also owe great thanks to William Peck and especially Karen Harpp of my alma mater, Colgate University, who played instrumental roles in me making it to MIT. Thank you always. I am also indebted to the assistance and insights of colleagues Richard Carlson and Julie Donnelly-Nolan, who have contributed to some of the research presented here.

Many thanks are also owed to the wonderful administrative staff in the EAPS department. Roberta Allard, Jacqui Taylor, Carol Sprague, Pat Walsh, and Vicki McKenna have been wonderful throughout my time in the department. My greatest of this thanks going to Carol Zayotti for many engaging discussions that allowed me to express my opinions on worldly matters, but always had an equally, or in many cases more informed opinion of what was actually going on. Her continually positive disposition was always refreshing no matter how my week was going.

I owe many thanks to my fellow students for their time and friendship: Mike Krawczynski, Noah McLean, Christy Till, Seth Burgess, Terry Blackburn, Krystal Catalli, Scott Burdick, Kyle Bradley, Nate Dixon, Lindsay Hays, Chris Waters, Anna Monders, Einat Lev, Kat Potter, Anita Ganesan, Alex Evans, Peter Sugimura, Jimmy Elsenbeck, Rosalee Lamm, Blair Schoen, Evelyn Mervine, Peter Meleney, Danny McPhee, Peter James Denedy-Frank, Peter James, Grant Farmer, Ben Black, and Maureen Long. In particular I must thank Noah McLean for always being there for tossing around the disc, late night ABP runs, jogs around the river and for just always being there. Mike Krawczynski and Christy Till have been two of the greatest labmates a fellow graduate student could imagine. Mike, thanks for talking sports, science, tech, and life with me and thank you for your undying enthusiasm for science and teaching. You will go far and I owe much of my interest in planetary science to you.

I owe untold gratitude to Tim Grove for his guidance as my advisor. He took quite a chance accepting me into the lab with little igneous petrology experience and I will always be grateful. Throughout our time together I have always felt like I had a great friend as well as a great mentor overseeing my progress. I never loathed working on the sailboat or providing an able hand as crew, and have always enjoyed your unique insight into science and life. I learned lessons far beyond research science while working with you, and I will be a better scientist and person because of it. I will miss fixing things in the lab with you, looking at experiments on the probes, discussing recent papers and just sitting down for lunch. You have two great sons and a wonderful wife, and I have been extremely fortunate to have been able to study under your watchful eye. Thank you for your time, knowledge and your wonderful hospitality. You are a gentleman and a scholar.

My family, Theresa, Gerald, Jesse and Jacob have assisted me along my way to this milestone in my life. My parents did the best job they could to raise my brothers and I the right way and they gave up so much to do so. It is an unrequitable debt, but they should know that it has made a difference. Jesse and Jacob are amazing brothers and I am so incredibly proud of who they are and proud to be their brother. May Gob bless all of your lives with success and fulfillment.

Table of Contents

Introduction

In order to understand volcanic processes in the solar system, samples of primitive melt products must be recognized and sampled. Primitive lavas can provide crucial information about the modes of melting, crystallization, and magmatic evolution that operate in the interiors and on the surfaces of planetary bodies. Experimental petrology plays an important role in deciphering the information preserved by primitive magmatic products. This work looks at some of the most enigmatic primitive magmas in our solar system, including Archean komatiites, lunar ultramafic glasses, and primitive magnesian andesites. These chapters focus on using experiments and petrography to determine how source mineralogy, melting and assimilation, magma mixing, volatiles and emplacement conditions have been involved in the production of these primitive samples. The final chapter helps to improve our understanding of how to quantify oxygen fugacity in high-temperature hydrous experiments in order to more fully constrain the multitude of variables that affect the outcomes of petrologic experiments.

Chapter 1 examines the emplacement conditions of the Commondale komatiites from South Africa. The Commondale Komatiite liquid composition has ~32 wt% MgO and an anhydrous liquidus temperature of 1550 °C. The minor element chemistry of the most primitive orthopyroxenes require crystallization in undercooled conditions, however the Mg# of the natural orthopyroxenes also require the Commondale melts to be emplaced under hydrous conditions. The hydrous emplacement conditions are similar to those found for the Barberton komatiites of Parman et al. (1997), and the study of Wilson (2003) demonstrates that the Commondale komatiites have geochemical signatures similar to modern boninites.

Chapter 2 is an investigation of the generation of the Apollo 15 green glasses from the Moon. Olivine and orthopyroxene were found on the liquidus multiple-phase saturation points for compositions that span the range of CaO and Al_2O_3 compositions found in the group A green glasses (Elkins-Tanton et al., 2003). Additional experiments were performed with altered group A compositions in order to saturate with a garnet-lherzolite mineral assemblage. These experiments were used to calibrate a melt prediction

model used to estimate the composition of melts of a primordial lunar mantle. Models of the assimilation process suggested by Elkins-Tanton et al. (2003) produced the group A and group C green glasses with mixtures of late-stage magma ocean cumulates and primordial lunar mantle melts. Additionally, experiments on a group A composition, plus 10% olivine, was found to saturate with a garnet-lherzolite at high pressure. This may indicate that the low-Ti glasses of Apollo 15 may have formed by melting of subsolidus reequilibrated Fe-rich magma ocean cumulates that had garnet and clinopyroxene prior to the onset of melting. Evidence of the possible role of primordial lunar mantle melts in the generation of mare ultramafic glasses would indicate that the lunar magma ocean was not whole moon, and may provide a fertile, easily melted, source for melts during the mare period.

Chapter 3 reexamines the phenocryst petrology and geochemistry of the primitive magnesian andesites of Mt. Shasta to determine if the magma is a melt of the mantle or a mixture of other Mt. Shasta magmas. The suggestion by Streck et al. (2007) that the primitive magnesian andesite studied by Anderson (1976) and Baker et al. (1994) is a mixture of dacite, basalt and peridotite was shown to be incorrect. The primitive olivines thought to be the evidence for peridotite were shown to be in equilibrium with a new more primitive, unmixed sample from a newly identified locality at Mt. Shasta. Additionally, the Os isotopic signature of the primitive magnesian andesite precludes any significant interaction with a sub-volcanic peridotite. Instead, the compositions of the most primitive magnesian andesite shows evidence of being produced by mantle melting. The recent work of Wood and Turner (2009) argues that primitive magnesian andesites are produced by melting of harzburgites, and their results indicate that the primitive magnesian andesites of Mt. Shasta and Mt. Lassen require high magmatic H_2O contents to be produced at pressures consistent with mantle melting beneath the southern Cascades of northern California.

Chapter 4 does not examine a primitive magma, but instead focuses on the use of AuPd alloy capsules often used in hydrous, high-temperature and high-pressure experiments on primitive magmas. Fe-loss to AuPd alloy capsules was examined in a series of experiments designed to equilibrate basaltic and andesitic melts with AuPdFe alloys. These experiments were used with a ternary solution model,

produced from previous work on the three binary alloys, to determine the dependence of the exchange reaction on temperature and oxygen fugacity. The dependence is then used to calculate the oxygen fugacity of AuPd alloy capsule piston cylinder experiments that were run without a buffer. This approach allows the oxygen fugacity to be quantified in experiments that otherwise could not have provide an independent estimate of the oxygen fugacity.

Bibliography

Anderson, A.T., 1976, Magma-mixing: Petrological process and volcanological tool: Journal of Volcanological and Geophysical Research, v. 1, p. 3-33.

Baker, M.B., Grove, T.L., and Price, R.C., 1994, Primitive basalts and andesites from the Mt. Shasta region, N. California: products of varying melt fraction and water content: Contributions to Mineralogy and Petrology, v. 118, p. 111-129.

Elkins Tanton, L.T., Chatterjee, N., and Grove, T.L., 2003, Experimental and petrological constraints on lunar differentiation from the Apollo 15 green picritic glasses: Meteoritics and Planetary Science, v. 38, p. 515-527.

Parman, S. W., Dann, J. C., Grove, T. L., de Wit, M. J., 1997. Emplacement conditions of komatiite magmas from the 3.49 Ga Komati Formation, Barberton Greenstone Belt, South Africa. Earth Planet. Sci. Lett 150, 303-323.

Streck, M.J., Leeman, W.P., and Chesley, J., 2007, High-magnesian andesite from Mount Shasta: A product of magma mixing and contamination, not a primitive mantle melt: Geology, v. 35, p. 351-354.

Wilson, A. H., 2003. A new class of silica enriched, highly depleted komatiites in the southern Kaapvaal Craton, South Africa. Precam. Res. 127, 125-141.

Wood, B.J., and Turner, S.P., 2009, Origin of primitive high-Mg andesite: Constraints from natural examples and experiments: Earth and Planetary Science Letters, v. 283, p. 59-66.

Chapter 1: Hydrous Komatiites from Commondale, South Africa: An Experimental Study

Abstract

This study examines the emplacement conditions of komatiites in the 3.33 Ga Commondale Ultramafic Suite in South Africa. The komatiites of Commondale are unlike any other komatiites in both their physical structure and chemical nature. Komatiite unit chill margins preserve original komatiite liquid compositions with an Mg# of 0.91, MgO = 31.9 wt%, Al_2O_3 wt% / TiO_2 = 80 (wt. %), and SiO_2 content of 49.7wt%. A common feature throughout the komatiite sequence is the presence of orthopyroxene spinifex, where original orthopyroxene crystals are still preserved. The compositional information preserved in the most primitive of the natural pyroxenes present in these spinifex zones (Mg# = 0.92), provides insight into the original emplacement conditions of the komatiites. This study used anhydrous and hydrous equilibrium experiments, along with disequilibrium cooling-rate experiments, to quantify the crystallization conditions of the Commondale komatiites. The anhydrous, 1-atm liquidus was found at 1550°C, with Fo97 olivine being the initial crystallizing phase, followed by spinel and then by protoenstatite, Mg# 0.95, at 1335°C. The phase relations were also examined at 200 MPa under H_2O saturated conditions. The addition of ~ 4 wt. % H_2O lowers the appearance temperature of the initial pyroxene by 210°C, thereby producing orthopyroxene with a Mg# closer to that of the most primitive preserved orthopyroxenes found in the komatiites. Additionally, dynamic cooling-rate experiments show that the natural pyroxenes preserve a chemical signature indicative of crystallization and cooling within an inflated flow complex. Estimates of the pre-eruptive H_2O content for the Commondale komatiites are between ~ 2 and 4.3 wt. % H_2O in the liquid. This range is similar to that estimated for 3.5 Ga komatiites of the Barberton Mountainland and may indicate formation of both suites in similar tectonic environments.

Introduction

Komatiites are the most ultramafic melts ever to have been erupted on the Earth's surface, some with MgO contents >30 wt%. Komatiites were first identified in the Barberton Mountainland of South Africa (Viljoen and Viljoen, 1969). Although primarily occurring in terrains of Archean and Early Proterozoic age (de Wit and Ashwal, 1997), there are some rare occurrences of Paleozoic age (Echeverria, 1980; Hynes and Francis, 1982).

Characterized by spinifex textured mineral phases, primarily olivine or pyroxenes, and MgO contents >18 wt%, komatiites have long been thought to be a product of melting at great depths (greater than 400km) in hot mantle plumes (Nesbitt and Sun, 1976). The conclusions of many investigators is that komatiites represent geologic conditions in the Archean that were dramatically different than those of the present day, where plate tectonics would have played only a minor role compared to mantle plume volcanism (e.g. Nisbet, 1982; Arndt, 2003; Bedard, 2003; Grove and Parman, 2004; Parman and Grove, 2005).

Other hypotheses have been presented to account for the ultramafic nature of some komatiites, one of which involves melting of hydrous oceanic mantle in a subduction zone (Allegre, 1982). The idea of forming some komatiites in a tectonic environment similar to modern subduction zones was revived by more recent studies that illustrated the need for H_2O to explain the spinifex morphology and petrology of Barberton komatiites (e.g. Grove et al., 1996; Parman et al., 1997; Grove et al., 2002; Wilson et al., 2003; Grove and Parman, 2004). Like modern basalts, Archean komatiites are likely to have formed in a variety of tectonic settings and likely had different H_2O contents. Work by Berry et al. (2008) on komatiites from Belingwe indicate crystallization under anhydrous or nearly anhydrous conditions, whereas other studies find hydrous emplacement conditions to be necessary for the Barberton komatiites (Parman et al., 1997).

Experimental studies have shown that H_2O is needed to reproduce the petrology of the Barberton komatiites, which preserve primary pyroxenes whose compositions necessitate the presence of H_2O (~4.2 wt%) during crystallization (Parman et al., 1997). The presence of H_2O is also needed to produce the

nucleation and growth environment required to form spinifex textures. When the results of cooling rate experiments are combined with estimates of the cooling histories experienced within thick units at Barberton (Grove and Parman, 2006), it appears that H_2O must have been present in the melt during solidification beneath a thick pile of inflated flows in order to form spinifex textures. The high pre-eruptive water content determined by the experimental study of Parman et al. (1997) has been disputed based on field observations and arguments concerning H_2O saturation at atmospheric pressures (Arndt et al., 1998). However, subsequent work has shown these criticisms to be invalid. Arndt et al. (1998) noted the conspicuous absence of vesicular komatiites, but careful field observations and mapping by Dann (2001) highlighted the presence of vesicular komatiites in the Komati Formation of the Barberton Greenstone Belt. Also, Parman et al. (2001) and Grove and Parman (2004) disputed the assumption that komatiites must be anhydrous due to emplacement at shallow pressures, since work by Ohenstetter and Brown (1996) found hydrous natural boninites glasses with H_2O contents up to ~7 wt%. These hydrous glasses represent quenched high-Mg# magma that retained its volatile content even though it was emplaced at low pressures. In addition to these studies, a more recent examination of a 3.3 Ga occurrence of komatiites near Commondale, South Africa has shown that the chemistry of the komatiite flows show a relationship to boninites, which are hydrous lavas produced in modern subduction environments (Wilson, 2003; Wilson et al., 2003).

Previous studies by Wilson (2003) and Wilson et al. (2003) describe, both physically and chemically, the komatiitic units of the 3.3 Ga komatiite suite of Commondale, South Africa. They contain a number of different lithologies: olivine cumulates, olivine and pyroxene spinifex zones, brecciated chill margins, and cross cutting zones of spinifex representing expelled residual liquids. Data from cooling units, including the sampling depths are shown in Figure 3 of Wilson (2003), and indicate thicknesses of 6 and 13 meters for the sampled units, with the spinifex zones greater than a meter from either chill margin. The olivine cumulates and the chill margins display chemical trends that are very distinct from the komatiites of Munro Township and Barberton. Wilson (2003) also illustrated that the Commondale

samples appear to have more of a chemical affinity to boninites than that of other komatiites (See Figures 4. and 7.; Wilson, 2003).

Surface samples of the Commondale komatiites show variable extents of metamorphism to talc and tremolite, and chlorite, however some samples still preserve >20% original igneous minerals, with Fo96 olivine and Mg# = 0.92 orthopyroxene (Wilson, 2003; this study). As illustrated by the Barberton studies, pyroxene compositional evidence can provide crucial insight into the pre-eruptive H_2O content of komatiite melts. The focus of this study is to investigate the emplacement conditions recorded by the pyroxenes in the Commondale komatiites, and to evaluate the role of water in their formation.

Analytical Methods

The pyroxene in the Commondale lavas and the experimental run products were analyzed by WDS with the MIT five-spectrometer JEOL 733 Superprobe. The on-line data reduction utilized the CITZAF correction package, which used the atomic number correction of Duncumb and Reed, Heinrich's tabulation of absorption coefficients, and the fluorescence correction of Reed to obtain a quantitative analysis (Armstrong, 1995). All analyses were performed with a 15 kV accelerating voltage and a 10 nA beam current. For experimentally produced glasses, the beam was defocused to 10 microns and Na was counted for 5 seconds at the beginning of the analysis. Other elements were measured for up to 40 seconds, depending on abundance level. For all other phases, a 2 micron spot size was used. Analytical precision was similar to that achieved by Gaetani and Grove (1998) on the MIT electron microprobe. H_2O contents of hydrous glasses were analyzed by ion microprobe. See Medard and Grove (2008) for procedure and discussion of analytical precision of the ion microprobe analyses.

Commondale Spinifex and Liquid Characterization

A comprehensive description of the regional and local geology of the Commondale Ultramafic Suite is presented by Wilson (2003). This study examined samples of orthopyroxene spinifex collected

from surface exposures, where contact relations had been determined by detailed mapping. In the Commondale Ultramafic Suite, orthopyroxene spinifex occurs as coarse spinifex units inside inflated lobe or sheet flows (Wilson, 2003) and as thin, 3 to 5 cm wide, parallel veins intruding olivine cumulate units (Figure 1). The groundmass surrounding the original igneous orthopyroxene spinifex comprises fine grained talc, tremolite, and minor amounts of magnetite. Olivine cumulate units, containing orthopyroxene-spinifex veins, exhibit intercumulus orthopyroxene needles, 0.5 cm x 0.05 cm (Figure 1). Wilson (2003) identified preserved igneous olivine from diamond drill core samples, however, the olivine cumulate samples obtained from surface outcrops for this study have all suffered low-temperature alteration and do not retain primary igneous olivine compositions. The coarse spinifex units lack evidence of olivine ever having been present, but contain well preserved orthopyroxene spinifex exhibiting a wide variety of morphologies. The variety of spinifex morphologies found in a single sample illustrates how many different forms of spinifex can result from the same thermal history (Figure 2). The orthopyroxene spinifex needles in the coarse spinifex units consist of 7 to 10 cm long, up to 0.5 cm wide, internally skeletal prisms with equant to rectangular cross sections. Long-axis sections and equant cross sections of orthopyroxene spinifex can be found adjacent to each other throughout the coarse spinifex units, exhibiting a lack of a preferred orientation produced by the spinifex growth conditions. Detailed interpretation of individual spinifex morphologies is not the focus of this study, but any attempt to do so must be consistent with crystallizing all forms within the same unit. Both the coarse spinifex units and the spinifex veins examined in this study exhibit the same range in chemical composition and are considered to have originated from the same magmatic conditions, differing only in their local emplacement environment.

Petrology of the Commondale Pyroxene Spinifex

Cross sections of the pyroxene grains show smooth normal zoning profiles, with core Mg#'s ranging from 0.90 to 0.92 and the rims reaching Mg#'s of 0.84 to 0.87. Similar zoning profiles are seen in Cr_2O_3 wt% and CaO wt% (Figure 3 and Figure 4). This consistent zoning profile is less apparent in Al_2O_3

wt%. The pyroxene crystals do not show evidence of sector zoning optically or chemically. The samples analyzed in this study are from a spinifex zone that is >15 cm thick and contains no olivine. Representative analyses of the most magnesian pyroxene compositions are found in Table 1. Because of the internally skeletal nature of the pyroxene, it is often difficult to tell which grain cross-sections intersect the cores of the orthopyroxenes. Edge to edge traverses were made across many pyroxene grains in order to locate the most magnesian cores of the pyroxene spinifex.

Experimental Liquid Composition

In order to perform relevant phase equilibrium experiments a representative liquid composition must be extracted from the complicated lithologies that make up the Commondale komatiite flows. The Commondale flow units do not exhibit flow structures typical of other komatiites (Wilson, 2003), however chill margins are easily identifiable at the boundaries of flow units in many locations. The chill margins are fine grained, sometimes brecciated, and have undergone low temperature metamorphism similar to the spinifex samples mentioned above. Because the Commondale flows are thought to be inflated flows or sills, see section 6.5 below, the chill margins are the best possible samples to use in the determination of the original liquid composition. For this study, the average composition of 13 chill margin analyses was used as the experimental starting composition (Table 2). These chill margins were identified in drill core from the Commondale sequence. Samples were taken over the depth range of ~16 m and ~120 m (unpublished database; Wilson, 2003). To ensure the chill margins were not significantly altered, they were compared to the compositional variation exhibited by the entire suite of Commondale lavas. The chills exhibit characteristics that are consistent with their representing the original liquid compositions. The FeO wt% and SiO_2 wt% contents of the Commondale liquid is distinctly different than those of other komatiites. Wilson (2003) and Wilson et al. (2003) explain that these features, seen consistently throughout the entire Commondale komatiite suite, are a result of the melts being generated from a previously depleted source, suggestive of melting in the mantle wedge of a subduction zone. Therefore, the chemical composition derived from the average of the chill margins is thought to represent

the intrinsic chemistry of Commondale komatiite magma and not syn- or post-emplacement chemical alteration.

Experimental Methods

Starting Composition

The starting material was made from a mixture of high purity oxides, which were ground under ethanol in an agate mortar and pestle to a homogeneous powder mixture (Kinzler, 1997). A sample of the starting material was melted and quenched to a glass in a non-reactive, graphite capsule at high pressure to ensure the correct composition had been achieved.

0.1 MPa Isothermal and Cooling Rate Experiments

Experiments at 0.1 MPa were performed at MIT in a vertical-tube DelTech quenching furnace, with a CO_2-H_2 gas atmosphere. The oxygen fugacity was monitored using a ZrO_2-CaO oxygen cell, and was kept near the quartz-fayalite-magnetite buffer. The sample material for these experiments consisted of ~50 mg of the oxide mixture that had been mixed with polyvinyl alcohol (DuPont Elvanol) and pressed into a pellet. This pellet was then sintered on to an iron-platinum alloy loop, which had been previously annealed with 4-6 wt% Fe to help prevent Fe loss to the alloy during the experiment. When possible, loops that had previously been run with the sample composition were used to further minimize the possibility of Fe loss. The sample temperature was measured using a Pt-$Pt_{90}Rh_{10}$ thermocouple calibrated to the melting points of NaCl, Au, and Pd. The thermocouple was placed in the hotspot of the furnace, where the thermal gradient is <1°C. The sample was suspended alongside the thermocouple, so they were at the same level within the furnace, minimizing the difference between the temperature of the sample and the reading of the thermocouple. The reproducibility and measurement of this arrangement is to better than 5°C.

Both isothermal and constant cooling rate experiments were performed under anhydrous conditions at 0.1 MPa. For the isothermal experiments, the furnaces were allowed to thermally equilibrate at the target temperature before the samples were inserted. When the run was finished it was drop-quenched into water. The samples for the cooling rate experiments were loaded into the furnace when it had equilibrated at 1550°C, and were then cooled at 10°C/hr or 100°C/hr until they reached ~1130°C. They were then drop-quenched into water.

200 MPa Water Saturated Experiments

Experiments were performed at MIT in a Zr-Hf-Mo alloy (ZHM) cold-seal gas pressure vessel, heated in a vertical-tube DelTech furnace. Temperature was measured using a Pt-$Pt_{90}Rh_{10}$ thermocouple calibrated in the same manner as the 0.1 MPa experiments. The thermocouple was positioned on the exterior of the pressure vessel at the same level as the sample on the interior. The difference between the exterior temperature and the sample temperature was calibrated numerous times using two thermocouples. The reproducibility and measurement of this arrangement is to ±7°C. The experiments were carried out at H_2O saturated conditions over the pressure range of 180 to 210 MPa. The pressure was measured using a Heise gauge. The experimental run assembly consisted of an outer capsule made of $Au_{80}Pd_{20}$ alloy that held the sample capsule, 20 µl of H_2O, and two platinum buffer capsules filled with a mixture of powdered Ni and NiO. This outer capsule was welded shut and weighed before and after being heated to 100°C for 5 minutes, to check for leaks. The sample capsule was made of $Au_{80}Pd_{20}$ for the highest temperature experiment and $Au_{90}Pd_{10}$ for the others. This was done to minimize the amount of Fe loss to the capsule for the experiments that were run at conditions below the melting point of $Au_{90}Pd_{10}$. The starting material was placed inside the sample capsule along with 3 µl of H_2O and crimped loosely shut. A mixture of Methane and Argon were used to pressurize the sample. The mixture of gases buffered the H_2 fugacity on the exterior of the capsule near the Ni-NiO buffer, which in turn helped prevent loss of H_2O from within the capsule due to H_2 diffusion through the walls of the outer capsule.

Evaluation of Equilibrium

Achievement of equilibrium is essential for the isothermal experiments to be successful. Experiments were mass balanced, via linear regression of the mineral and glass compositions, against the original starting composition to determine if there had been any significant elemental loss, specifically Fe. Also, the olivine Fe-Mg K_D was calculated to determine if equilibrium had been achieved; K_D = ~0.3. In the hydrous experiments, the presence of liquid water in the capsule along with both buffering species still present was also necessary for the experiment to be deemed a success. The cooling rate experiments were performed on iron - platinum alloy loops that had been used for previous isothermal experiments that did not show Fe loss.

Experimental Results

0.1 MPa Isothermal Experiments

Results of the isothermal experiments at 0.1 MPa are presented in Tables 2 and 3. Olivine (Fo_{97}, Fe-Mg K_D = 0.30), is the liquidus phase and begins to crystallize at 1550°C. Chrome spinel joins the crystallization sequence following olivine, between 1410°C and 1350°C. At 1345°C protoenstatite appears in the equilibrium assemblage. Protoenstatite is identified by the pervasively fractured grains, caused by the conversion of protoenstatite to clinoenstatite upon quench of the experiment. This initial pyroxene has Mg# of 0.95 and Wo (Ca/(Ca+Mg+Fe); molar cations) content of 0.005. By 1275°C the equilibrium pyroxene changed from protoenstatite to orthoenstatite with an Mg # = 0.94. As mentioned above, the Commondale liquid composition is unique when compared to other komatiites, however the consistency of the most primitive olivine composition and that of our liquidus olivine, both Fo97, illustrates that our chosen experimental liquid composition preserves the Fe-Mg character of the primitive Commondale komatiite magmas. It should also be noted that many olivine-liquid geothermometers lack direct experimental calibration at temperatures above 1300°C at low pressures. The experiments of this

study can be integrated into the calibration of existing geothermometers to allow for more accurate prediction of temperature and olivine composition calculations for high temperature applications.

0.1 MPa Cooling Rate Experiments

The results of the 10°C/hr and 100°C/hr cooling rate experiments performed at 0.1 MPa are shown in Figure 5. These experiments were performed to investigate the influence of cooling rate on the initial crystallizing pyroxene under dynamic conditions. Because these experiments were run over such a large temperature interval, the exact temperatures of phase appearance could not be determined. However, by analyzing the cores of the compositionally zoned pyroxenes, the composition of the earliest pyroxenes can be determined. For the 10°C/hr run the Mg# of the most primitive pyroxenes is 0.94 and for the 100°C/hr the Mg# is 0.93. The effect of increased cooling rate is to suppress the appearance of the pyroxene relative to olivine, so it crystallizes with a lower Mg#. Crystallizing low-Ca pyroxene under disequilibrium conditions is known to affect the minor element partitioning (e.g. Walker et al., 1976; Grove and Bence, 1977) and can clearly be seen in the abundances of Cr_2O_3, Al_2O_3, and CaO. The amount of Cr_2O_3 is >2.4 wt% in the most primitive cooling rate pyroxenes, with Al_2O_3 >4.5 wt% and CaO >1.2 wt%. The increase in the abundance of these elements with increased cooling rate is similar to the effects of cooling rate on pigeonite composition observed by Grove and Bence (1977).

200 MPa Water Saturated Experiments

Experiments run under H_2O-saturated conditions were performed at pressures of 180 to 210 MPa. The liquidus phase is olivine; however, the liquidus temperature could not be determined because it would be above the melting temperature of the $Au_{80}Pd_{20}$ sample capsules and exceed the maximum temperature that can be achieved in the pressure vessel. The highest temperature experiment, 1275°C at 210 MPa, contains Fo96 olivine (Fe-Mg K_D = 0.30). The H_2O content of this experiment is ~4.5 wt%, and based on models of the effect of H_2O on olivine liquidus suppression (Medard and Grove, 2008), the

expected liquidus would be ~1420°C. At 200 MPa the initial pyroxenes crystallize at 1135°C, and they are needlelike orthopyroxene with an Mg# of 0.93 (Table 2 and Figure 5). This is 210°C lower than the anhydrous 0.1 MPa experiments and is similar to the phase appearance suppression seen in the study of the Barberton komatiites of Parman et al. (1997), which exhibited a suppression of ~200°C at 200 MPa (Figure 6).

Discussion

Disequilibrium Pyroxene Growth

Spinifex texture has traditionally been characterized as a quench texture due to the rapid cooling of komatiites from extremely high liquidus temperatures (e.g. Green et al., 1975). In olivine-spinifex komatiites, olivine is the sole crystallizing phase and forms the spinifex texture. However, many locations contain pyroxene-spinifex units consisting primarily of clinopyroxene spinifex, including the Upper Komati Formation (Dann, 2000). In the case of the Commondale komatiites, orthopyroxene spinifex is equally abundant and often occurs in flows that do not contain olivine spinifex. The traditional explanation of spinifex forming as a quench texture can not explain the formation of the orthopyroxene spinifex of this study, since it does not appear until the lava has cooled to more than 200°C below the liquidus, under anhydrous conditions, and there is a distinct lack of olivine, spinifex or otherwise, in many of the orthopyroxene spinifex zones. However, minor element compositions of the orthopyroxene spinifex grains indicate a disequilibrium growth history.

The cores of the orthopyroxene spinifex crystals have a maximum Mg# of 0.92, with Cr_2O_3 ~2.5 wt%, CaO ~0.75 and Al_2O_3 ~3 wt% (Figures 3 and 4, Table 1). Compared to the experimentally produced pyroxenes at 1-atm, the first natural pyroxenes to crystallize from the magma have a lower Mg# and higher abundances of Cr_2O_3, CaO and Al_2O_3. Initial pyroxenes of the cooling rate experiments show Cr_2O_3 wt% contents similar to the natural pyroxenes, however, the Mg#'s, Al_2O_3 wt%, and CaO wt% of the cooling rate pyroxenes are still too high to match the pyroxenes in the natural samples. Increasing the

cooling rate would serve to further decrease the Mg#, but this would also increase the Al_2O_3 wt% and CaO wt%. Furthermore, the natural orthopyroxenes were sampled from the interior of a flow unit, approximately 0.5 m from the boundary, where cooling rates are expected to be less than 0.5°C/hr. The natural pyroxenes experienced cooling histories that would be slower than those imposed experimentally, so faster cooling rates can not be used to explain the crystallization of the lower Mg# natural pyroxenes.

Despite the inability of high cooling rates to explain the natural orthopyroxene compositions, some of the compositional trends in the disequilibrium experiments are mimicked in the natural pyroxenes. Correlations between Cr_2O_3, CaO, and Mg# in the cooling rate pyroxenes are strikingly similar to the trends exhibited in the natural pyroxenes (Figure 4). The similarities in the observed slopes of these trends, between the 100°C/hr and 10°C/hr experiments, suggest the trend is not rate dependent and would also result from cooling at a much slower rate, more like what is expected for a spinifex zone in the slowly cooled interior of a komatiite unit. The correlation between these elements is similar to that observed in dynamic crystallization studies of pigeonite in a lunar basalt composition (Grove and Bence, 1977). Grove and Bence (1977) found that incompatible elements like Al_2O_3 and CaO increased in abundance in the pyroxene as cooling rate increased and crystallization departed further from equilibrium. Grove and Bence (1977) also observed that the partition coefficient for the compatible element Cr remained high at faster cooling rates. This is counter to the behavior of other compatible elements with faster cooling. Their partition coefficients approach unity. The explanation for Cr partitioning remaining high may be that it is preferentially incorporated into the orthopyroxene structure to charge balance the higher amounts of Al^{3+} that is partitioning into the crystal. Thus at slower cooling rates this disequilibrium effect still persists.

Petrologic Evidence for Hydrous Crystallization Conditions

A slower cooling rate would serve to grow a pyroxene with similarly high Cr_2O_3 wt% and Al_2O_3 wt% and slower cooling would also increase the Mg# of the initial pyroxene. However, the natural pyroxenes need the high Cr_2O_3 wt% and Al_2O_3 wt% at still lower Mg#'s (Figure 5). In order to explain

these compositions, the role of H_2O in the melt was considered, which would have the effect of suppressing pyroxene crystallization. By depressing the appearance temperature of the initial pyroxene, relative to the olivine liquidus, the melt would crystallize olivine over a larger temperature interval, which would lower the Mg# of the initial pyroxene. This effect is observed in the 2 kbar H_2O saturated experiments, which contain ~4.5 wt% H_2O (Figure 5). In these experiments the initial equilibrium pyroxene Mg# has dropped from 0.95, for the anhydrous experiments, to 0.93 in the H_2O saturated experiment. Combined with the slow cooling disequilibrium effect discussed above, hydrous komatiite lavas would produce orthopyroxene with a lower Mg# but still high Cr_2O_3 and Al_2O_3 contents, like those preserved in the Commondale komatiites.

Estimation of Pre-Eruptive H_2O

The H_2O saturated experiment that best reproduced the natural pyroxenes, contained ~4.5 wt% H_2O (ComW-7). To produce the melt composition of this experiment, the starting composition needs to fractionate 51% olivine. If the melt contained ~4.5 wt% H_2O after this extensive fractionation, then the minimum original H_2O content, at the liquidus, would be ~2.3 wt%. In the hydrous experiment, the Mg# of the initial pyroxenes remained more Mg-rich than the most primitive natural pyroxene, indicating that even more water could have been present. Assuming a linear relationship between the Mg# of the initial pyroxene and the H_2O content of the melt, an extrapolation can be made to correct the H_2O content to the Mg# of the initial natural pyroxene. This estimate produces a melt with ~7.7 wt% H_2O when pyroxene began to crystallize, which means a minimum H_2O content of ~4 wt% at the liquidus. Combined with variable amounts of undercooling of 10°C/hr or less, it is possible to produce the natural pyroxenes by crystallization from a lava with between ~2.3 - 4.0 wt% H_2O (Figure 7).

Similarity to Barberton Komatiites

Evidence for hydrous crystallization conditions for komatiites is not without precedent. The presence of hydrous komatiite lavas was well established for Barberton komatiites in the study of Parman et al. (1997). Their work examined the influence of water on pyroxene compositions to investigate the emplacement conditions of typical Barberton olivine-spinifex komatiite lavas. The study showed that anhydrous cooling rate and equilibrium experiments crystallized pigeonite prior to augite, however the Barberton komatiites contain augites with high Mg# and high Wo content cores, and no low-Ca pyroxene. Cooling rate experiments showed that rapid cooling did succeed in suppressing the Mg# of the initial pyroxenes from the high values produced in the equilibrium anhydrous experiments to values closer to those of the natural samples (Parman et al., 1997). The cooling rates required to completely suppress the crystallization of low-Ca pyroxene would be very rapid, a characteristic of the cooling conditions in the outer few mm of a cooling lava flow. Such crystallization conditions would not operate within the flow interior where the pyroxenes are preserved. However, H_2O saturated experiments successfully produced the initial pyroxene compositions found in the Barberton komatiites, and showed suppression of low-Ca pyroxene crystallization to a much lower temperature. The H_2O required to produce the pyroxene compositions of the Barberton komatiites, estimated at a minimum of ~4.2 wt% H_2O at the time of pyroxene crystallization (Parman et al., 1997), is similar to the values obtained in this study for the Commondale komatiites.

Despite the differences in the compositions of the Commondale and Barberton komatiites, the petrologic evidence in both suites implicates the need for similarly high pre-eruptive H_2O contents to produce the preserved mineralogy. Several studies have been published that dispute the presence of H_2O in komatiites from Barberton (e.g. Arndt et al., 1998). However, as mentioned above the alternative explanations provided in these studies fail to accommodate the preserved petrology and mineralogy of the komatiites.

Implications for Spinifex Growth

Recent studies on the formation of olivine spinifex textures by Shore and Fowler (1999) and Faure et al. (2006) suggest, respectively, that olivine spinifex grows in a specific orientation due to the anisotropic thermal conductivity of olivine or the presence of large thermal gradients during crystallization of komatiite flows. It is unclear if these arguments can be applied to pyroxene spinifex. In the Commondale komatiites, orthopyroxenes with similar Mg#'s, showing contemporaneous growth, are commonly found to have grown perpendicular to each other. This exemplifies the lack of a preferred growth orientation, which is a necessary consequence of both of the growth mechanisms suggested in the two aforementioned studies.

Any attempt to explain the factors that lead to spinifex growth in komatiites must account for the presence of not only olivine spinifex, but also clinopyroxene (e.g. Dann, 2000 and Dann and Grove, 2007) and orthopyroxene spinifex, as observed at Commondale. Because spinifex is an observed habit in all three of these minerals it is expected to be less a consequence of a specific mineralogical property and more related to the crystal growth environment, similar to the thermal gradient explanation of Faure et al. (2006). Recent work by Houlé et al. (personal communication) have concluded that spinifex bearing flows from the Abitibi belt are inflated flows or sills, similar to those described by Grove et al. (1996), Dann (2001), and Dann and Grove (2007) for the Barberton komatiites. Perhaps the thermal boundary conditions of an inflated flow or sill would allow a hydrous komatiite to cool slowly enough to allow growth of the pyroxenes found in the Commondale komatiites. In particular, an inflated flow would provide the best scenario to preserve orthopyroxene, clinopyroxene, and olivine spinifex, as it would allow multiple generations of liquids to utilize the same conduit. Successive lavas coming from the same magma chamber could have undergone variable differentiation, thereby producing lavas that are near saturation with orthopyroxene when they are erupted into the conduit system. Alternatively, the orthopyroxene spinifex could result from enhanced crystallization due to the degassing of the komatiite lava as it flows into the distal recesses of a conduit system. These both would allow for olivine and pyroxene spinifex to occur in the same units with olivine cumulates, just as it is seen in the Commondale

ultramafic suite, Barberton Mountainland, and in the Abitibi greenstone belt. This would also preserve anhydrous, degassed, komatiitic basalts and hydrous komatiite lavas in the same formation.

Conclusions

The Commondale komatiite liquid composition contains ~32 wt% MgO and ~ 50 wt% SiO_2. With such a primitive liquid, under anhydrous conditions, protoenstatite is the initial pyroxene rather than orthoenstatite, which is found preserved in the natural komatiites. Furthermore, under anhydrous conditions pyroxene begins to crystallize too early, thereby producing a pyroxene with a higher Mg# than the natural pyroxenes. Hydrous experiments allow the initial pyroxene to crystallize at a much lower temperature, ~210°C less than anhydrous, which serves to produce pyroxene with a lower Mg#. Additionally, the preserved minor element composition of the Commondale orthopyroxenes indicates crystallization in a cooling or degassing environment similar to those expected in inflated komatiite flows. The estimated H_2O contents for the Commondale and Barberton komatiites are similarly high (at ~4 wt% H_2O for the liquid), and are most consistent with formation in a subduction zone setting, similar to that of modern day boninites.

Bibliography

Allègre, C.J., 1982. Genesis of Archean komatiites in a wet ultramafic subducted plate. In: Arndt, N.T., Nisbet, E.G. (Eds.), Komatiites. Springer-Verlag, Berlin, pp. 495-500.

Armstrong, J. T., 1995. Citzaf - a package of correction programs for the quantitative Electron Microbeam X-Ray-Analysis of thick polished materials, thin-films, and particles. Micro. Analys. 4, 177-200.

Arndt, N. T., Ginibre, C., Chauvel, C., Alberede, F., Cheadle, M., Herzberg, C., Jenner, G., Lahaye, Y., 1998. Were komatiites wet? Geology 26, 739-742.

Arndt, N. T., 2003. Komatiites, kimberlites and boninites. J. Geophys. Res. 108, 2293.

Barr, J. A. and Grove, T. L., 2006. Investigating the Depth of Komatiite Melting Using Experimentally Determined Olivine and Orthopyroxene Melt Reaction Coefficients. EOS Trans. Am. Geophys. Un. 87, 52: Fall Meet. Suppl., Abstract V24B-05.

Bedard, J., Brouillette, P., Madore, L. and Berclaz, A., 2003. Archean cratonization and deformation in the northern Superior Province, Canada: an evaluation of plate tectonic versus vertical tectonic models. Precam. Res. 127, 61-87.

Berry, A.., Danyushevsky, L., O'Neill, H., Newville, M. and Sutton, S., 2008. Oxidation state of iron in komatiitic melt inclusions indicates hot Archean mantle. Nature 455, 960-963.

Dann, J. C., 2000. The 3.5 Ga Komati Formation, Barberton Greenstone Belt, South Africa, Part I: New maps and magmatic architecture. S. Afr. J. Geol. 103, 47-68.

Dann, J. C., 2001. Vesicular komatiites, 3.5 Ga Komati Formation, Barberton Greenstone Belt, South Africa: inflation of submarine lavas and origin of spinifex zones. Bull. Volcanol. 63, 462-481.

Dann, J. C. and Grove, T. L., 2007. Volcanology of the Barberton Greenstone Belt, South Africa: Inflation and evolution of flow fields, in: M. J. van Kranendonk, R. H. Smithies, V. C. Bennett, (Eds.), Precambrian Ophiolites and related rocks, Developments in Precambrian Geology; 15. Elsevier, Amesterdam; London. pp. 527-570.

de Wit, M. J. and Ashwal, L. D., 1997. Convergence towards divergent models of greenstone belts, in:de Wit, M. J. and Ashwal, L. D., (Eds.), Greenstone Belts. New York, Oxford University Press: ix - xix.

Echeverria, L. M., 1980. Tertiary or Mesozoic Komatiites from Gorgona Island, Colombia - Field Relations and Geochemistry. Contrib. Mineral. Petrol. 73, 253-266.

Faure, F., Arndt, N., Libourel, G., 2006. Formation of Spinifex Texture in Komatiites: an Experimental Study. J. Petrol. 47, 1591-1610.

Gaetani, G. A. and Grove T. L., 1998. The influence of water on melting of mantle peridotite. Contrib. Mineral. Petrol. 131, 323-346.

Green, D. H., Nicholls, I. A., Viljoen, M. J. and Viljoen, R. P., 1975. Experimental Demonstration of the Existence of Peridotitic Liquids in Earliest Archean Magmatism. Geology 3, 11-14.

Grove, T. L. and Bence, A. E., 1977. Experimental study of pyroxene-liquid interaction in quarts-normative basalt 15597. Proc. Lunar Planet. Sci. Conf. 8th, 1549-1579.

Grove, T. L., Gaetani, G. A., Parman, S. W., 1996. Origin of olivine spinifex textures in 3.49 Ga komatiite magmas from the Barberton Mountainland, South Africa. EOS, Trans. Am. Geophys. Un. 77, 281.

Grove, T. L. and Parman, S. W., 2004. Thermal evolution of the Earth as recorded by komatiites. Earth Planet. Sci. Lett. 219, 173-187.

Grove, T. L. and Parman, S. W., 2006. The development of spinifex textures in komatiites. GAC/MAC An. Meet. 31, Montreal, Canada.

Grove, T. L., Parman, S. W., Bowring, S. A., Price, R. C., Baker, M. B., 2002. The role of an H_2O-rich fluid component in the generation of primitive basaltic andesites and andesites from the Mt. Shasta region, N California. Contrib. Mineral. Petrol. 142, 375-396.

Hynes, A. and Francis, D., 1982. Komatiitic basalts of the Cape Smith foldbelt, New Quebec, Canada, in: Arndt, N. T. and Nisbet, E. G. (Eds.), Komatiites. Berlin, Springer-Verlag, pp. 159-170.

Kinzler, R. J., 1997. Melting of mantle peridotite at pressures approaching the spinel to garnet transition: Application to mid-ocean ridge basalt petrogenesis. J. Geophys. Res. 102, 853-874.

Medard, E. and Grove, T. L., 2008. The effect of H_2O on the olivine liquidus of basaltic melts: experiments and thermodynamic models. Contrib. Mineral. Petrol. 155, 417-432.

Nesbitt, R. W. and Sun, S. S., 1976. Geochemical features of some Archaean spinifex-textured peridotites and magnesian and low-magnesian tholeiites. Earth Planet. Sci. Lett. 31, 433-453.

Nisbet, E. G., 1982. The tectonic setting and petrogenesis of komatiites, in: Arndt, N. T. and Nisbet, E. G. (Eds.), Komatiites. Berlin, Springer-Verlag, pp. 501-520.

Ohnenstetter, D., and Brown, W., 1996. Compositional variation and primary water contents of differentiated interstitial and included glasses in boninites, Contrib. Mineral. Petrol. 123, 117-137.

Parman, S. W., Dann, J. C., Grove, T. L., de Wit, M. J., 1997. Emplacement conditions of komatiite magmas from the 3.49 Ga Komati Formation, Barberton Greenstone Belt, South Africa. Earth Planet. Sci. Lett 150, 303-323.

Parman, S. W., Grove, T. L., Dann, J. C., 2001. The production of Barberton komatiites in an Archean subduction zone. Geophys. Res. Lett. 28, 2513-2516.

Parman, S. W. and Grove, T. L., 2005. Komatiites in the plume debate, in: Foulger, G. R., Natland, J. H., Presnall, D. C., and Anderson, D. L., (Eds.), Geological Society of America Special Paper 388. Geol. Soc. of Am., pp 249-256.

Shore, M. and Fowler, A. D., 1999. The origin of spinifex texture in komatiites. Nature 397, 691-694.

Viljoen, M. J. and Viljoen, R. P., 1969. The geology and geochemistry of the Lower Ultramafic Unit of the Onverwacht Group and a proposed new class of igneous rocks: Upper Mantle Project. Spec. Pub. - Geol. Soc. of S. Afr. 2, 55-85.

Walker, D., Kirkpatrick, R. J., Longhi, J., Hays, J. F., 1976. Crystallization history of lunar picritic basalt sample 12002: Phase-equilibria and cooling-rate studies. Geol. Soc. of Am. Bull. 87, 5: 646-656.

Wilson, A. H., 2003. A new class of silica enriched, highly depleted komatiites in the southern Kaapvaal Craton, South Africa. Precam. Res. 127, 125-141.

Wilson, A. H., Shirey, S. B., Carlson, R. W., 2003. Archean ultra-depleted komatiites formed by hydrous melting of cratonic mantle. Nature 423, 858-861.

Table 1. Spinifex pyroxene core compositions from Commondale Komatiites

Grain #	SiO_2	TiO_2	Al_2O_3	Cr_2O_3	FeO	MnO	MgO	CaO	Na_2O	Total	Mg#
139	53.88	0.03	3.66	3.01	5.58	0.18	32.39	0.79	0.01	99.53	0.91
51	54.56	0.04	2.88	2.98	5.70	0.16	33.00	0.67	0.01	99.98	0.91
73	54.69	0.04	2.98	2.95	5.40	0.09	32.95	0.70	0.00	99.80	0.91
52	54.76	0.04	3.05	2.89	5.54	0.16	33.27	0.66	0.01	100.37	0.91
140	53.85	0.00	3.54	2.82	6.04	0.11	32.47	0.77	0.00	99.60	0.91
53	54.62	0.04	3.01	2.81	5.39	0.12	32.61	0.67	0.01	99.28	0.91
74	54.95	0.05	2.69	2.79	5.82	0.08	32.73	0.65	0.01	99.78	0.91
14	56.02	0.02	2.85	2.61	5.64	0.10	33.05	0.71	0.02	101.01	0.91
54	55.14	0.03	2.87	2.60	5.60	0.15	33.12	0.70	0.02	100.23	0.91
141	54.41	0.02	2.87	2.57	5.58	0.14	32.39	0.78	0.02	98.79	0.91
17	54.60	0.02	3.23	2.51	5.81	0.11	32.33	0.71	0.04	99.36	0.91
13	54.21	0.01	2.95	2.47	6.18	0.12	32.66	0.80	0.00	99.41	0.91
55	55.39	0.08	2.88	2.41	5.66	0.14	33.25	0.75	0.02	100.58	0.91
18	54.80	0.01	3.34	2.41	6.18	0.11	32.51	0.72	0.04	100.11	0.91
75	55.28	0.05	2.22	2.41	7.34	0.09	32.20	0.66	0.02	100.27	0.91

Table 2. Electron microprobe analyses of experimental run products.

Experiment	Phase	SiO_2	TiO_2	Al_2O_3	Cr_2O_3	FeO	MnO	MgO	CaO	Na_2O	NiO	Total	Mg#
Starting Composition		49.68	0.09	7.20	0.51	5.73	0.13	31.90	4.26	0.36	0.15	100.01	0.91
Com1-1	gl (9)[a]	53.5(2)[b]	0.09(5)	9.96(5)	0.37(4)	6.41(13)	0.13(3)	23.3(1)	5.81(4)	0.35(3)	0.04(1)	100.11	0.87
	ol (7)	41.1(2)	0.01(1)	0.07(1)	0.28(2)	4.90(13)	0.10(3)	53.3(3)	0.13(1)	n/a	0.11(2)	100.00	0.95
Com1-2	gl (9)	55.6(2)	0.10(4)	11.5(1)	0.23(4)	6.12(15)	0.12(2)	18.9(1)	6.67(8)	0.33(4)	0.03(2)	99.74	0.85
	ol (20)	41.4(3)	0.01(1)	0.06(1)	0.24(2)	5.56(14)	0.10(1)	52.3(5)	0.14(1)	n/a	0.08(3)	99.91	0.94
	sp (9)	0.39(23)	0.05(2)	14.1(7)	58.2(9)	8.79(21)	0.15(3)	18.3(9)	0.10(6)	n/a	0.03(3)	100.18	0.79
Com1-4	gl (9)	54.4(2)	0.12(6)	13.7(2)	0.14(3)	6.09(18)	0.13(2)	15.8(1)	8.29(8)	0.41(6)	0.04(1)	99.27	0.82
	ol (8)	41.1(2)	0.01(1)	0.05(3)	0.18(2)	6.44(31)	0.13(3)	52.0(5)	0.16(1)	n/a	0.21(3)	100.27	0.94
	px (9)	57.3(5)	0.02(3)	1.31(34)	0.60(12)	3.90(21)	0.08(2)	36.2(4)	0.34(9)	0.05(6)	n/a	99.80	0.94
	sp (6)	0.49(22)	0.07(1)	20.3(9)	50.3(4)	9.51(17)	0.14(2)	18.7(5)	0.14(2)	n/a	0.08(2)	99.72	0.78
Com1-5	gl (10)	51.3(1)	0.06(4)	8.02(7)	0.39(4)	6.10(21)	0.11(2)	28.9(1)	4.68(5)	0.21(6)	0.08(2)	99.99	0.89
	ol (10)	41.7(2)	0.01(1)	0.07(1)	0.24(2)	3.77(10)	0.06(1)	54.7(2)	0.13(1)	n/a	0.20(4)	100.94	0.96
Com1-6	gl (9)	50.1(1)	0.07(3)	7.14(5)	0.37(4)	6.55(12)	0.10(2)	31.4(2)	4.17(5)	0.15(5)	0.06(1)	100.23	0.90
Com1-7	gl (10)	54.6(4)	0.15(3)	15.0(1)	0.13(6)	5.77(22)	0.14(5)	14.4(2)	8.98(13)	0.38(8)	0.03(3)	99.72	0.82
	ol (8)	41.3(4)	0.01(1)	0.05(3)	0.17(3)	6.33(19)	0.12(1)	51.5(4)	0.18(2)	n/a	0.22(4)	99.82	0.94
	px (10)	57.8(4)	0.02(1)	1.37(33)	0.52(6)	3.89(12)	0.08(1)	35.8(4)	0.38(11)	0.05(3)	n/a	99.98	0.94
	sp (5)	0.31(19)	0.05(1)	22.5(5)	48.2(2)	9.03(18)	0.17(2)	19.0(2)	0.14(4)	n/a	0.10(2)	99.62	0.79
Com1-11	gl (12)	50.6(1)	0.10(3)	7.58(6)	0.51(10)	6.22(19)	0.14(3)	30.6(1)	4.60(5)	0.24(2)	0.10(3)	100.61	0.90
	ol (7)	41.4(2)	0.01(1)	0.08(1)	0.23(2)	3.43(8)	0.06(1)	55.0(2)	0.13(2)	n/a	0.24(2)	100.55	0.97

Table 2. cont.

Experiment	Phase	SiO_2	TiO_2	Al_2O_3	Cr_2O_3	FeO	MnO	MgO	CaO	Na_2O	NiO	Total	Mg#
Com1-12	gl (12)	54.8(4)	0.20(5)	13.5(2)	0.20(4)	6.22(21)	0.18(5)	16.2(2)	8.30(8)	0.46(4)	0.04(3)	100.13	0.82
	ol (10)	41.2(4)	0.00(0)	0.10(3)	0.21(8)	5.90(11)	0.11(2)	52.1(5)	0.18(2)	n/a	0.28(3)	100.14	0.94
	px (7)	57.9(6)	0.00(0)	1.33(25)	0.68(10)	3.68(13)	0.08(2)	36.8(32)	0.31(1)	0.00(0)	n/a	100.83	0.95
	sp (4)	0.44(23)	0.06(1)	19.1(3)	51.3(8)	9.70(15)	0.15(3)	18.5(5)	0.18(5)	n/a	0.15(2)	99.57	0.77
Com1-13	gl (12)	54.6(4)	0.15(4)	12.5(3)	0.29(9)	6.44(27)	0.16(3)	17.6(5)	7.64(12)	0.42(6)	0.05(3)	99.94	0.83
	ol (15)	41.3(4)	0.00(0)	0.09(2)	0.21(5)	5.45(43)	0.11(2	52.2(7)	0.16(2)	n/a	0.26(7)	99.85	0.94
	px (9)	58.4(5)	0.01(1)	1.00(23)	0.59(7)	3.16(18)	0.07(2)	36.9(3)	0.29(4)	0.03(2)	n/a	100.45	0.95
	sp[c]												
ComW-1	gl (6)[d]	52.5(1)	0.10(4)	11.2(2)	0.21(2)	4.55(22)	0.13(2)	19.4(1)	6.58(17)	0.28(6)	0.01(1)	94.93	0.88
	ol (8)	41.4(3)	0.00(0)	0.03(1)	0.14(1)	4.34(9)	0.09(2)	54.4(3)	0.12(1)	n/a	0.13(4)	100.67	0.96
ComW-7	gl (5)[d]	54.5(2)	0.09(3)	16.0(2)	0.05(3)	4.26(14)	0.10(3)	10.7(2)	9.45(8)	0.40(4)	0.02(1)	95.54	0.82
	ol (9)	41.3(2)	0.01(1)	0.04(1)	0.08(1)	6.49(27)	0.15(2)	51.5(2)	0.13(1)	n/a	0.25(3)	99.92	0.93
	px (16)	57.3(4)	0.04(1)	1.80(26)	0.78(7)	4.54(20)	0.13(5)	34.9(5)	1.00(18)	0.01(1)	n/a	100.49	0.93
	sp[c]												

n/a = not analyzed

[a] = number of analyses

[b] = one standard deviation based on multiple analyses, expressed in terms of the least significant figure

[c] = too small to analyze

[d] = H_2O contents determined by ion microprobe (see text for procedural reference): ComW-1 = 5.04 wt%; ComW-7 = 4.48 wt%

Table 3. Summary of experiments performed in the current study. Compositional information for the phases produced is in Table 2. Fe loss is wt% relative to the starting material. Phase abbreviations are gl=glass, ol=olivine, sp=spinel, px=pyroxene. Negative Fe loss indicates Fe gain.

Experiment	Pressure (MPa)	Temperature (°C)	Phases Present	Olivine Fe-Mg K_D	% Fe loss	Run time (hrs)
Com1-1	0.01	1410	gl, ol	0.33	-4	24
Com1-2	0.01	1350	gl, ol, sp	0.33	-4	72
Com1-4	0.01	1300	gl, ol, sp, px	0.32	-4	50
Com1-5	0.01	1500	gl, ol	0.33	0	3
Com1-6	0.01	1550	gl	n/a	-14	2
Com1-7	0.01	1275	gl, ol, sp, px	0.31	0	120
Com1-11	0.01	1530	gl, ol	0.30	-5	2
Com1-12	0.01	1320	gl, ol, sp, px	0.30	-1	19
Com1-13	0.01	1340	gl, ol, sp, px	0.28	-2	14.5
ComCR-1	0.01	1550 -- 1130	gl, ol, sp, px	n/a	n/a	~4
ComCR-2	0.01	1550 -- 1130	gl, ol, sp, px	n/a	n/a	~45
ComW-1	2.1	1275	gl, ol, sp	0.34	20	3
ComW-2	2.0	1200	gl, ol, sp	n/a	n/a	5
ComW-3	2.0	1160	gl, ol, sp	n/a	n/a	5
ComW-5[a]	2.0	1130	gl, ol, sp	n/a	n/a	7
ComW-7	1.8	1125	gl, ol, sp, px	0.32	7	5

[a] Ni was not present in the buffer, but Fe loss would prematurely stabilize px so this experiment can

n/a = not analyzed

Figure Captions

Figure 1. Orthopyroxene Spinifex Veins **A.** Sample of an olivine cumulate unit with 7 veinlets of orthopyroxene spinifex. The veins are continuous through the sample and create a set or parallel planes of spinifex. **B.** Thin section view of preserved igneous orthopyroxene spinifex from a spinifex vein from the sample shown in A. **C.** Thin section view of the olivine cumulate from sample shown in A. The olivines show black alteration at the edges and along internal fractures, and small pieces of spinifex orthopyroxene occur with the metamorphic groundmass in the interstices of the olivine grains.

Figure 2. Orthopyroxene Spinifex Morphologies **A.** Hand sample of typical coarse orthopyroxene spinifex unit **B.** Curved spinifex **C.** Subparallel spinifex **D.** Radiating spinifex **E.** Perpendicular spinifex: long-axis sections of spinifex can be seen running from the upper left to lower right, and in between are cross sections of spinifex needles that were growing nearly perpendicular to the thin section view **F.** Branching spinifex. All varieties of spinifex are found in a single 7.62 cm x 12.7 cm thin section of the hand sample shown in A. All types of the spinifex were analyzed in search of the most primitive composition, and in particular the cross sections shown in E are some of the grains used in the current study.

Figure 3. Cross sections of the preserved Commondale pyroxenes show chemical zoning. Shown are microprobe analyses of a diagonal transect of one such grain. Analyses were performed at a regular interval, from edge to edge of the grain. Gaps in the data represent cracks in the grain from which data was unattainable. All microprobe analyses shown had oxide totals between 101.50 and 98.50, and cation totals between 4.015 and 3.985.

Figure 4. The crystal chemistry preserved by the Commondale pyroxenes show initial nucleation of Mg# 0.92 cores, with high Cr_2O_3, Al_2O_3, and CaO. This is followed by further growth in a fractional or near-fractional crystallization environment.

Figure 5. Orthopyroxene compositions from disequilibrium crystallization experiments, 10°C/hr and 100°C/hr, are shown in part A and compositions from equilibrium anhydrous and H_2O saturated experiments are shown in part B. **A.** The cores of the experimental pyroxenes are the high Mg# ends of the arrays. The trends seen in the Cr_2O_3 values illustrate the disequilibrium nucleation followed by a fractional or near-fractional crystallization trend produced during undercooling. As seen by the CaO values, any increase in the cooling rate would not achieve the natural pyroxene minor element compositions even if the initial Mg# was produced. **B.** The effect of H_2O is to lower the temperature at which the first pyroxene appears, thus increasing the minor element content and decreasing the Mg#. The "H_2O Sat" point represents the first equilibrium pyroxene in the 2 kbar H_2O saturated experiments. The "Anhy" point represents the first pyroxene to crystallize in the 1-atm, anhydrous experiments.

Figure 6. Experimentally determined, H_2O-saturated phase appearances for olivine and low-Ca pyroxene are shown for this study as well as for Barberton komatiites (Parman et. al., 1997). The initial low-Ca pyroxene for the Commondale composition (this study) is a protoenstatite at 1-atm and orthoenstatite at 0.2 GPa. The low-Ca pyroxene for the Barberton experiments is pigeonite. The phase boundary for the low-Ca pyroxenes exhibit a suppression in appearance temperature as pressure increases due to the pressure dependant nature of H_2O solubility; requires more H_2O to remain saturated. The Anhydrous olivine liquidus of the Commondale komatiites is known from high pressure experiments (Barr and Grove, 2006). The Hydrous Liquidi are calculated

according to the method of Medard and Grove (2008), because they are above the melting temperatures of experimental capsule alloys.

Figure 7. Shown are the relative effects of disequilibrium nucleation due to undercooling and equilibrium nucleation in an H_2O saturated melt. In combination, H_2O + undercooling, the compositions of the preserved natural pyroxenes can be reproduced. The "10°C/hr" point represents the average of the core compositions of the pyroxenes produced in the disequilibrium experiment. The "More Undercooling" and "Less Undercooling" represent estimated affects for cooling rates less than 10°C/hr.

Figure 1.

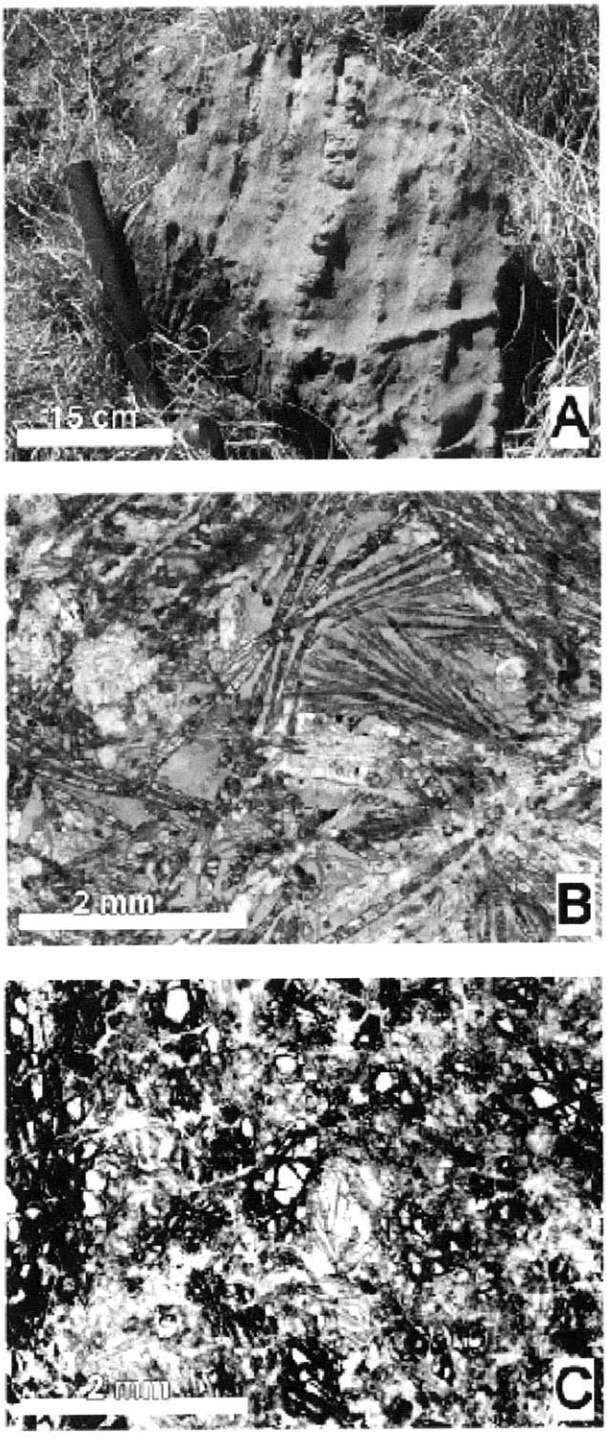

Figure 2.

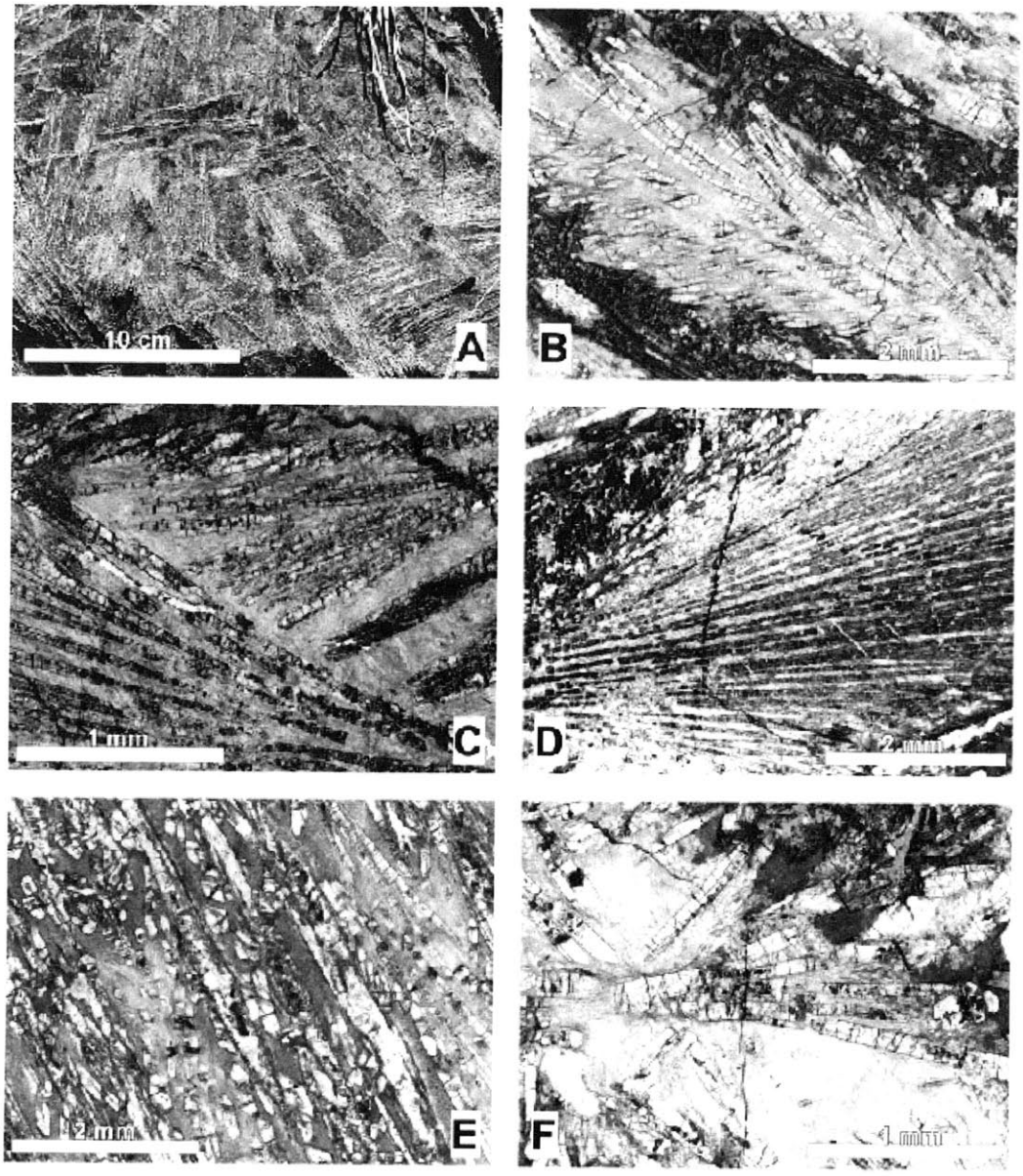

Figure 3.

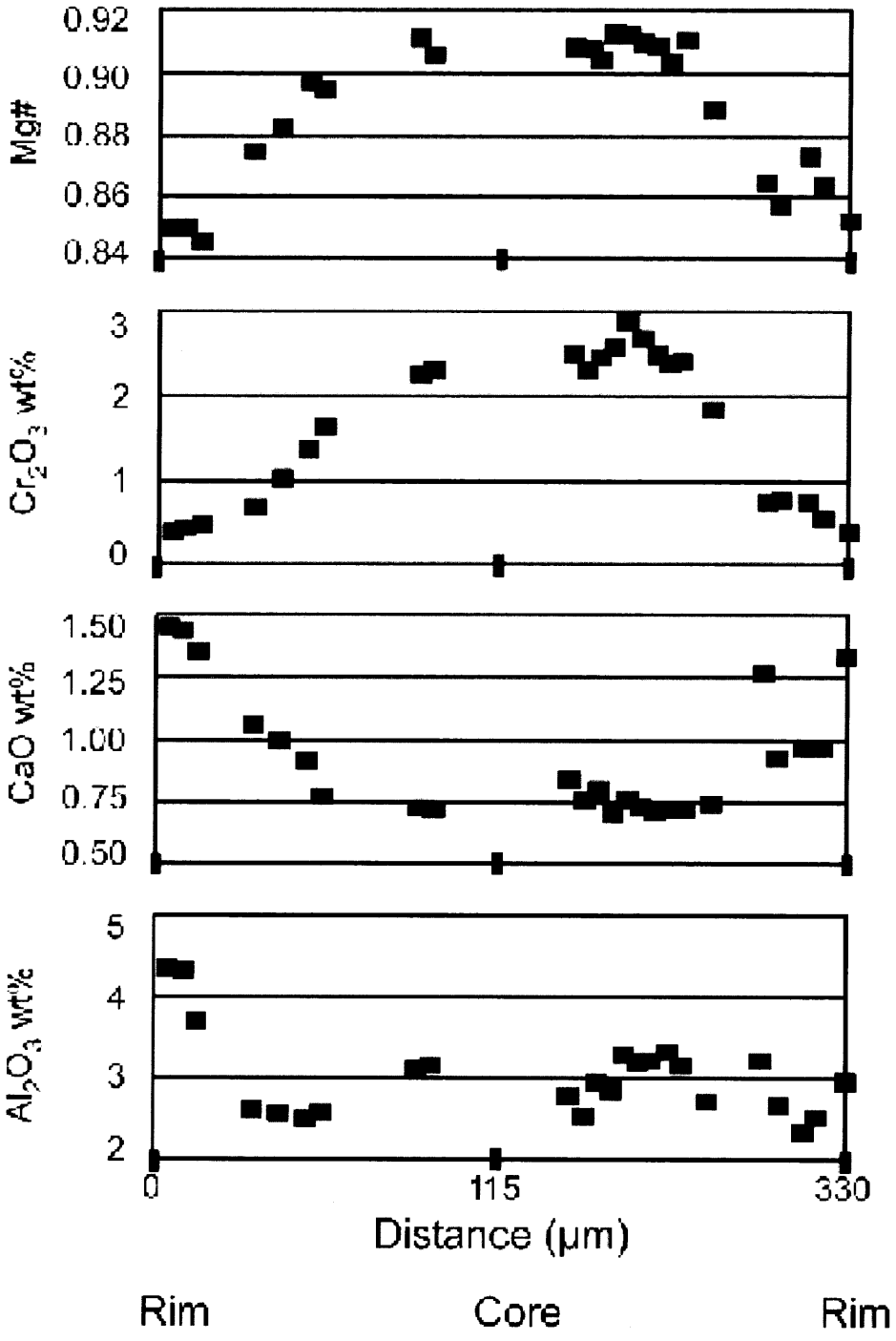
Mg#
0.92
0.90
0.88
0.86
0.84
Cr_2O_3 wt%
3
2
1
0
CaO wt%
1.50
1.25
1.00
0.75
0.50
Al_2O_3 wt%
5
4
3
2
0
115
330
Distance (μm)
Rim
Core
Rim

Figure 4.

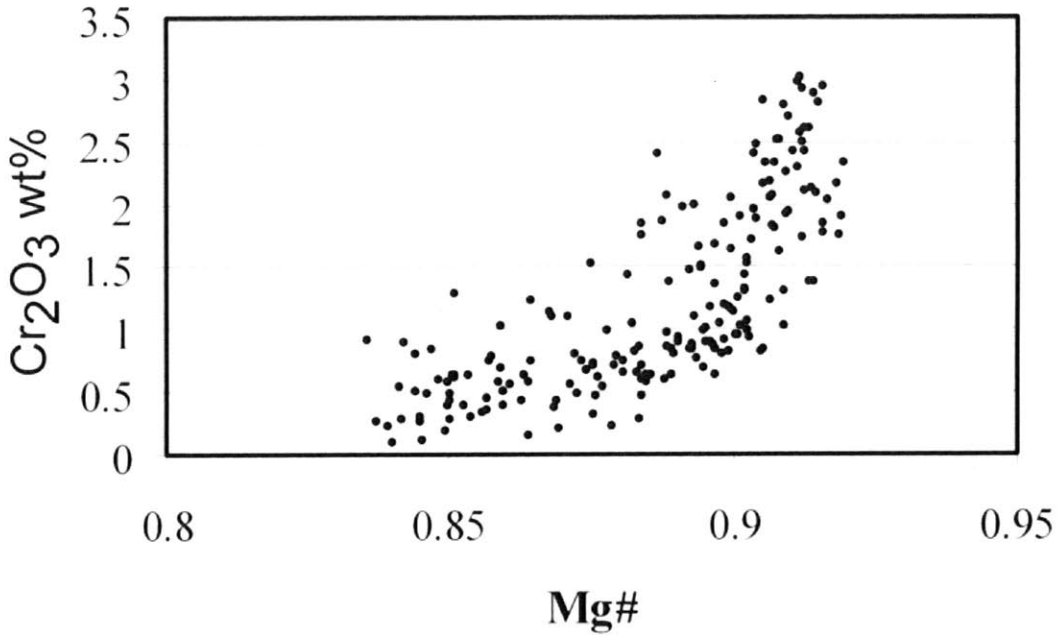
3.5
3
2.5
2
1.5
1
0.5
0
Cr2O3 wt%
0.8
0.85
0.9
0.95
Mg#

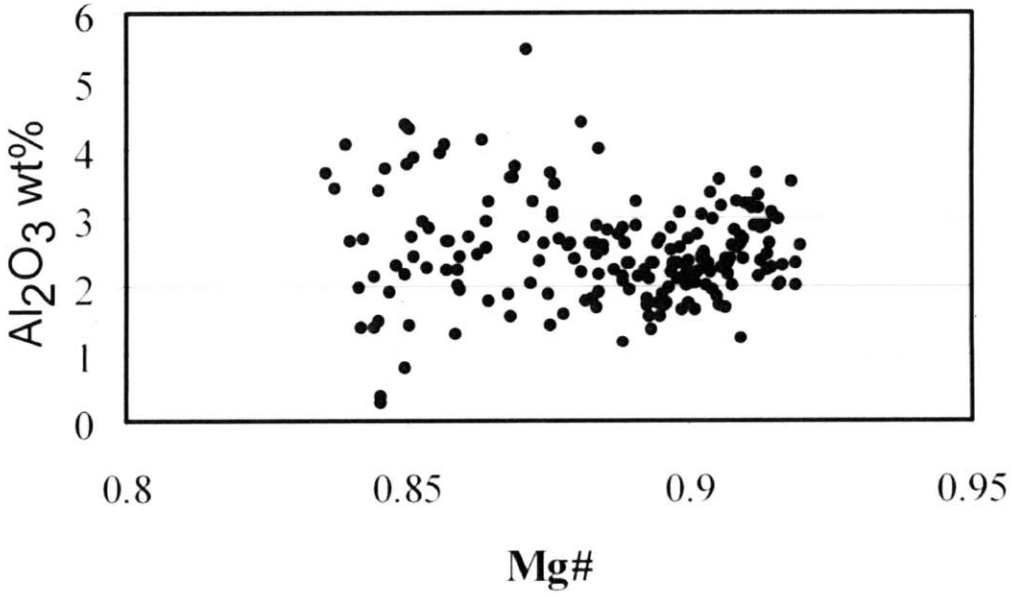
6
5
4
3
2
1
0
Al2O3 wt%
0.8
0.85
0.9
0.95
Mg#

Figure 4. cont.

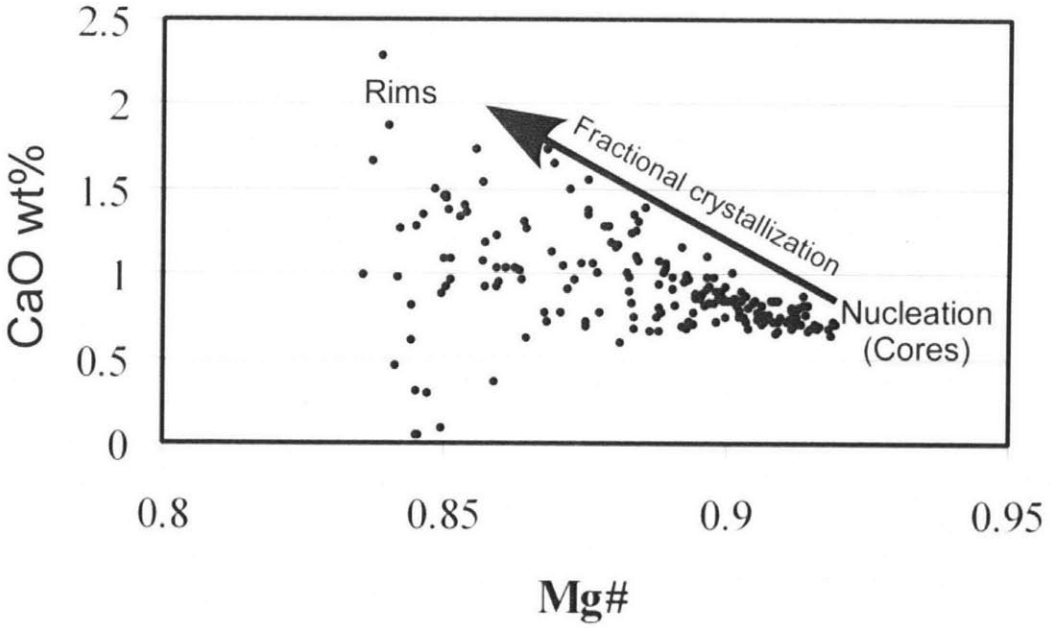

Figure 5a.

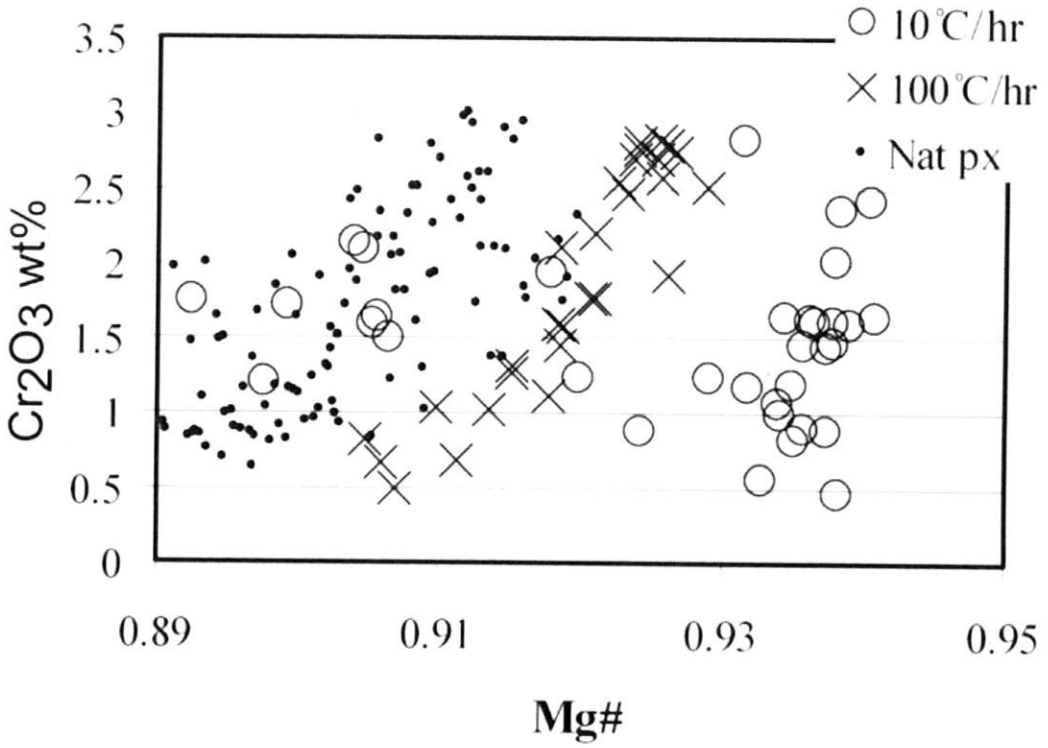
10°C/hr
100°C/hr
Nat px
3.5
3
2.5
2
1.5
1
0.5
0
Cr2O3 wt%
0.89
0.91
0.93
0.95
Mg#

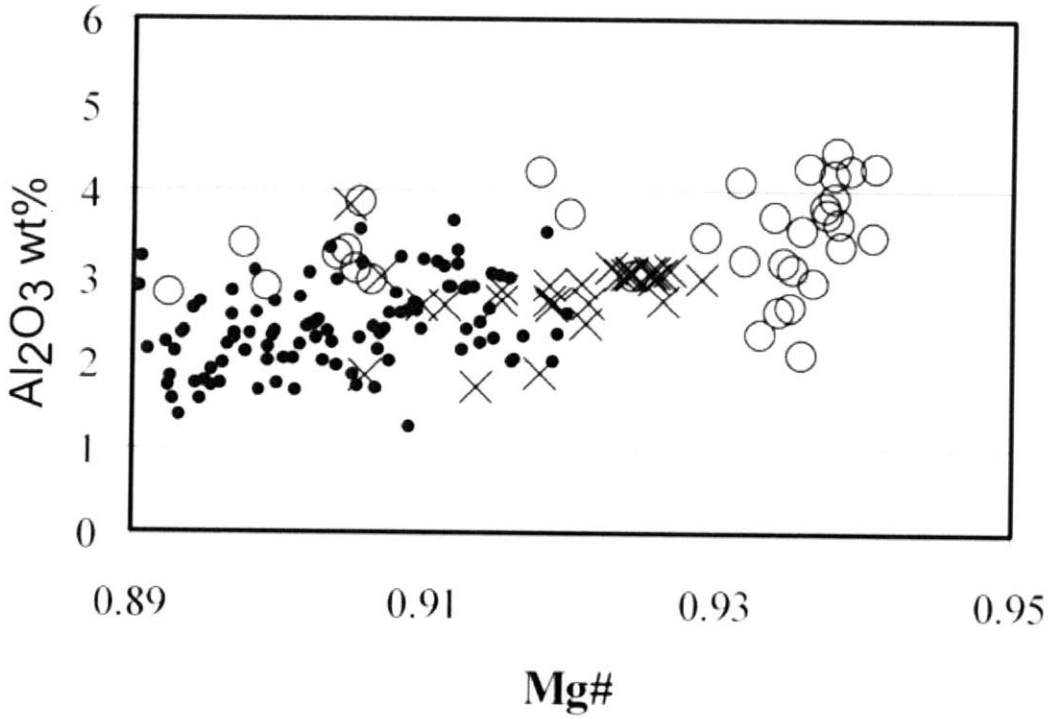
6
5
4
3
2
1
0
Al2O3 wt%
0.89
0.91
0.93
0.95
Mg#

Figure 5a. cont.

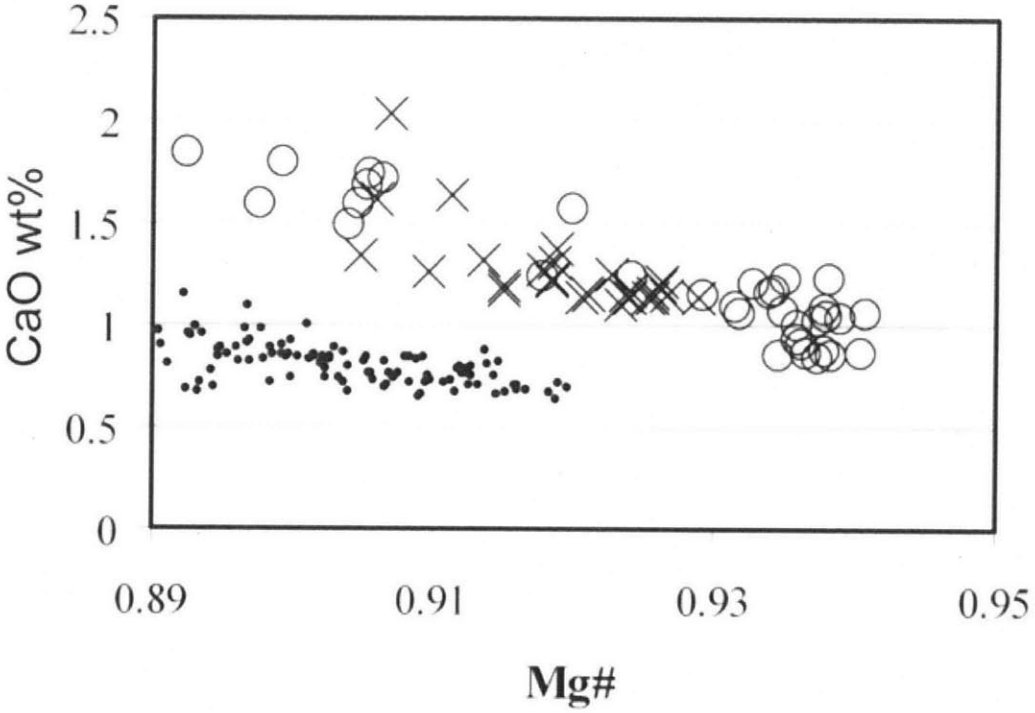

Figure 5b.

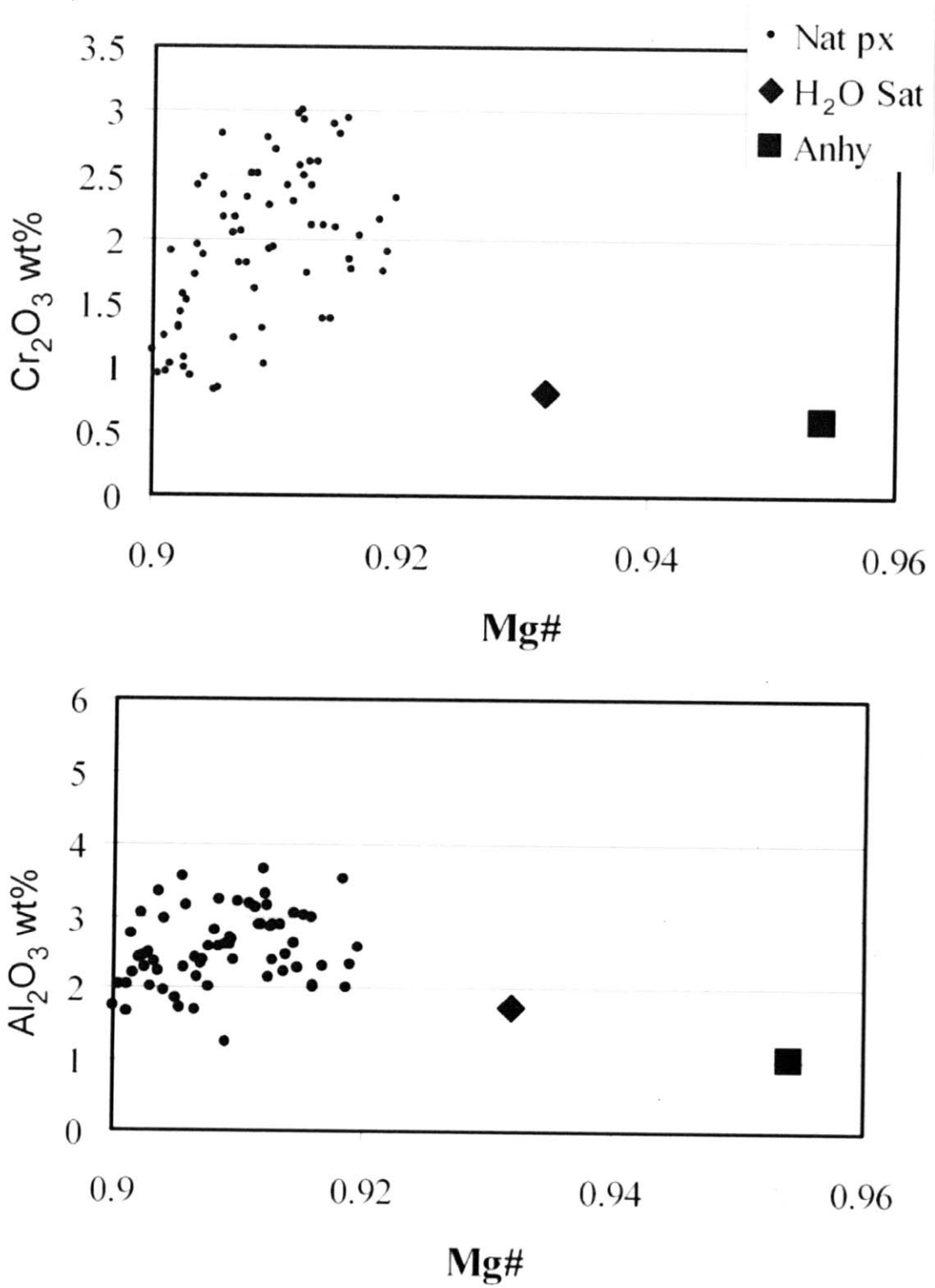
Nat px
H2O Sat
Anhy
3.5
3
2.5
2
1.5
1
0.5
0
Cr2O3 wt%
0.9
0.92
0.94
0.96
Mg#
6
5
4
3
2
1
0
Al2O3 wt%
0.9
0.92
0.94
0.96
Mg#

Figure 5b. cont.

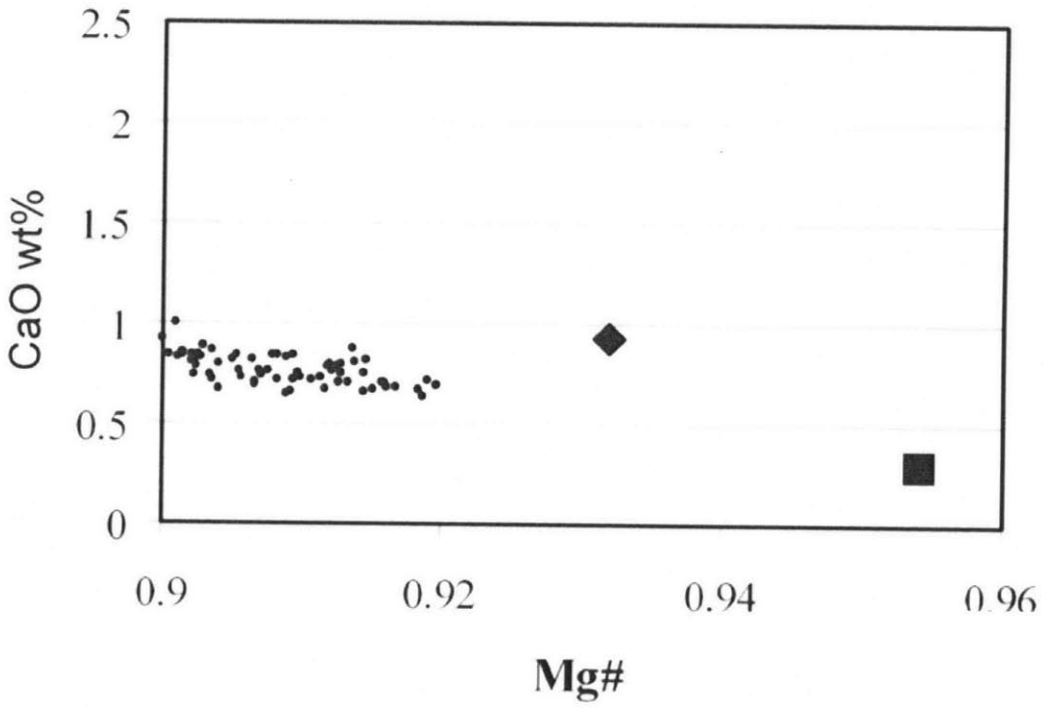

Figure 6.

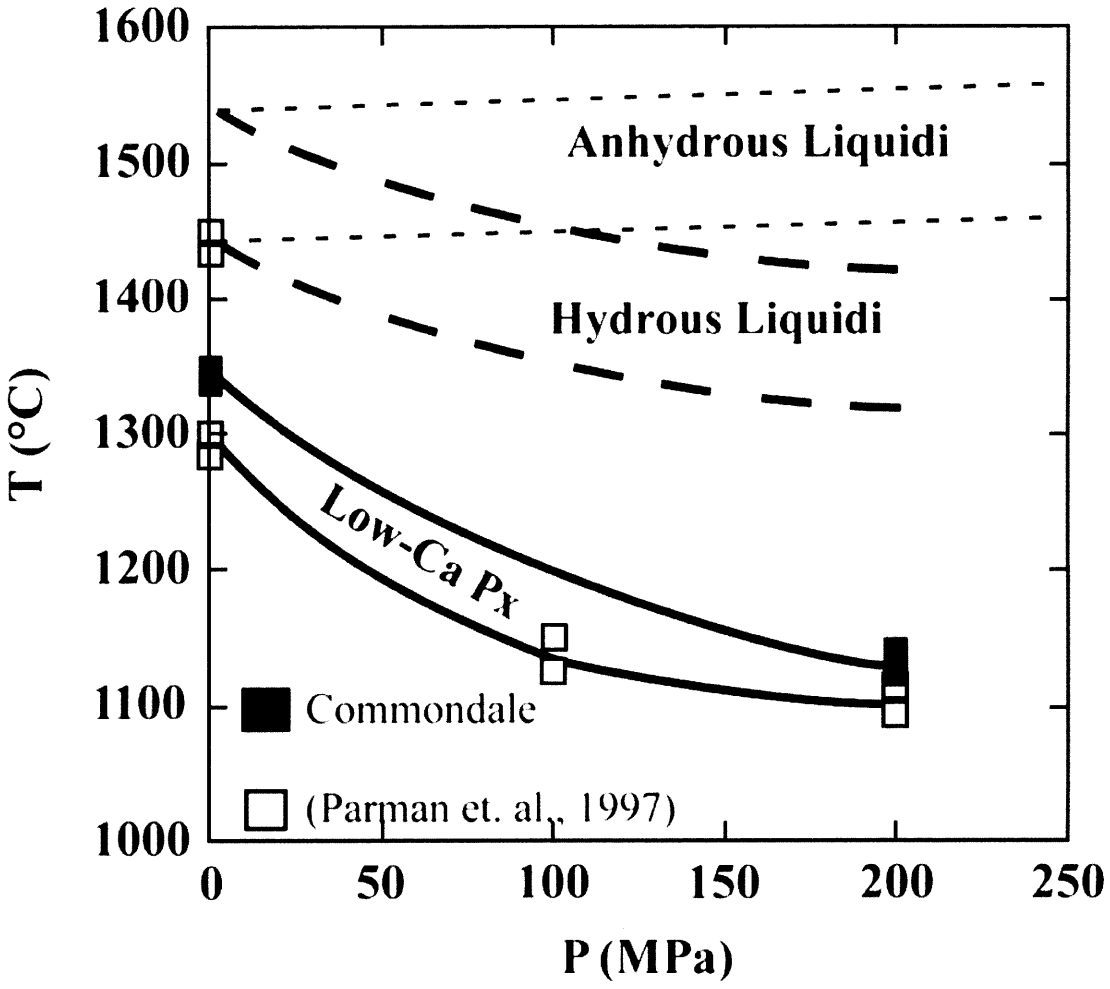
1600
1500
1400
1300
1200
1100
1000
T (°C)
0
50
100
150
200
250
P (MPa)
Anhydrous Liquidi
Hydrous Liquidi
Low-Ca Px
Commondale
(Parman et. al., 1997)

Figure 7.

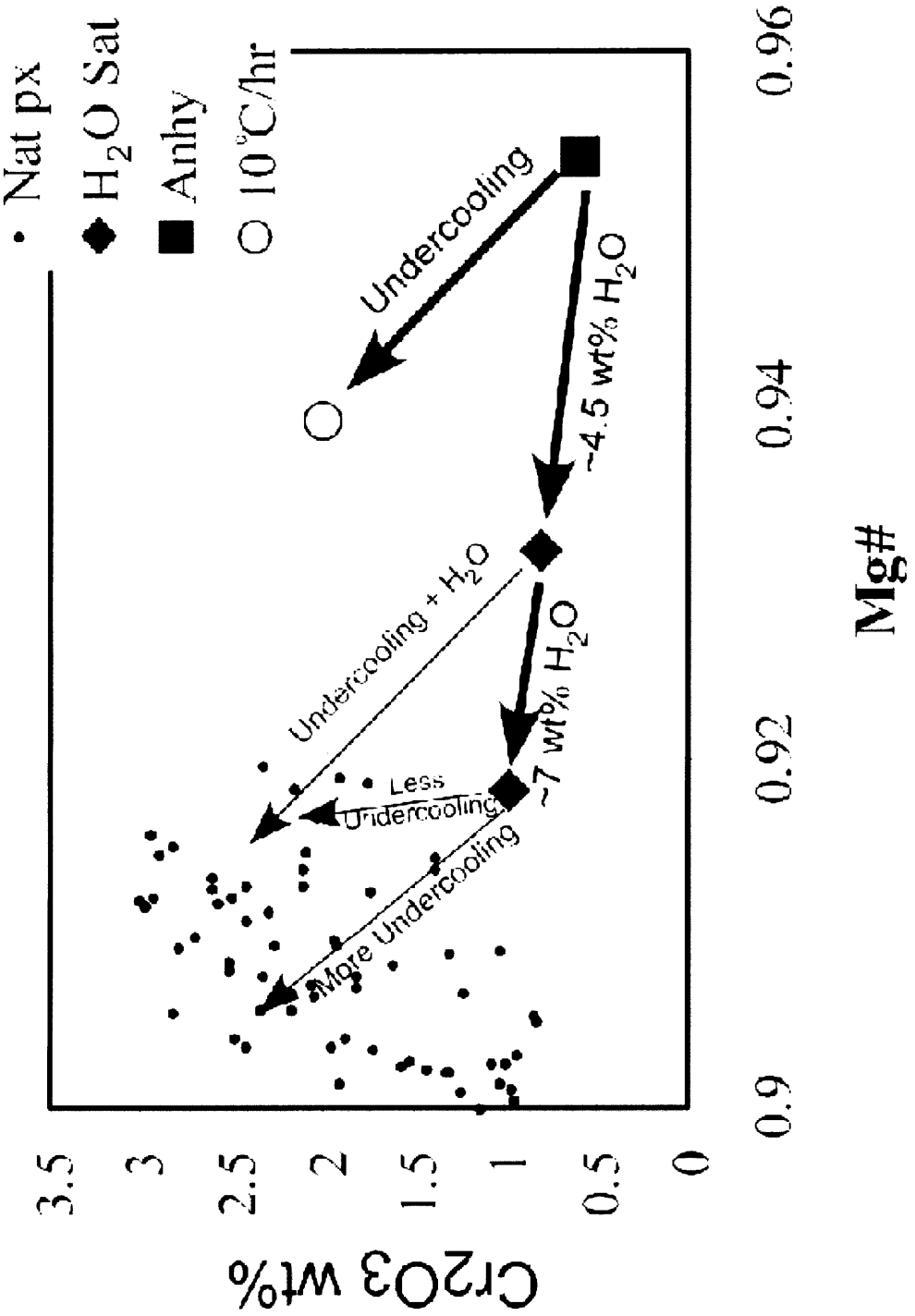
• Nat px
◆ H_2O Sat
■ Anhy
○ 10°C/hr
Undercooling
~4.5 wt% H_2O
Undercooling + H_2O
~7 wt% H_2O
Less Undercooling
More Undercooling
Cr2O3 wt%
3.5
3
2.5
2
1.5
1
0.5
0
0.9
0.92
0.94
0.96
Mg#

Chapter 2: Experimental Petrology of the Apollo 15 Group A Green Glasses and the Role of Garnet in the Ultramafic Glass Source

Abstract

Phase equilibrium experiments have been performed on two compositional end members of the Apollo 15 Group A ultramafic green glass, the most abundantly occurring glass composition found in the Apollo 15 green glass pyroclastic deposit (15426) at Hadley Rille station 6. Both compositions have a liquidus multiple phase saturation point with olivine and orthopyroxene at 1520°C and 2.1 GPa. Experiments were also performed on high-Al and high-Ca analog mixtures and mixtures of the green glass compositions with natural minerals (olivine, orthopyroxene and garnet) added to saturate experimental liquids with olivine, orthopyroxene, high-Ca clinopyroxene and garnet. Three liquids in equilibrium with a garnet-lherzolite residual assemblage were produced at 2.35 GPa, 1440 °C and 1420°C and at 2.6 GPa, 1460 °C. These garnet-saturated melts provide inputs into a model that can be used to predict the compositional characteristics of generated partial melts of deep primitive lunar mantle. Petrogenetic models that produce the Apollo 15 group A green glass are constructed using a combination of the evidence from experimental petrology, major element and trace element geochemistry. The Apollo 15 Group A glasses, are relatively iron rich (Mg# ~ 61) with low Ni contents (~200 ppm) and a negative Eu anomaly. Successful models require mixtures of primary magma, derived by melting primordial lunar mantle in the garnet stability field, and evolved pyroxenitic magma ocean cumulates. Additionally, other garnet-bearing lithologies may be melted to high extents to form the Apollo 15 green glasses, however these lithologies represent subsolidus reequilibration of shallow magma ocean cumulates that have been transported to greater depths during overturn. These cumulates would include plagioclase and/or a trapped liquid component. Melts of primordial lunar mantle may help provide heat to these overturned cumulates to facilitate melting.

Introduction

This study focuses on the compositional variability contained in the Apollo 15 group A green glasses, as defined by Delano (1979, 1986). Delano (1979) recognized 3 distinct compositional grouping in the green glass sample from station 6 at the Hadley Rille site: A, B and C. The Apollo 15A green glasses are the most abundant glass type and span a limited and coherent range of compositions. They are ultramafic and contain from 17.1 to 17.6 wt.% MgO and 19.5 to 20 wt.% FeO. In comparison to the other Apollo 15 green glass groups of Delano (1986), they show a wider variation in CaO (8.35 to 8.5 wt. %) and Al_2O_3 (7.2 to 7.6 wt. %). This study presents high-temperature, high-pressure experimental results for two compositions chosen from the 15A glasses that span the range of CaO and Al_2O_3 variability and on mixtures of the Group A glasses with analog compositions and mineral phases. These mix experiments were performed to better understand the constraints of high-pressure phase relations and melting reactions.

Several models of the potential processes that led to the formation of the ultramafic glasses have been proposed and are summarized by Elkins-Tanton et al. (2003). Longhi (1992) presents evidence for the involvement of primitive lunar mantle in the origin of low-Ti ultramafic glasses; however, their origin also appears to require the remelting or assimilation of cumulates of a solidified lunar magma ocean (LMO) (Galbreath et al., 1990; Shearer and Papike, 1993; Shearer et al., 1996). The ultramafic glass melting event, although not precisely constrained (Meyer et al., 1975 and Nunes et al., 1974), occurred approximately 500 to 1000 million years after the cessation of magma ocean solidification. Thus, the origin of the ultramafic glasses requires a high temperature source deep in the moon long after magma ocean solidification. Thermal models (Solomon and Longhi, 1977) predict that the deep interior of the lunar mantle will be molten at this time, so a deep primordial melt is a possible component.

The evidence for garnet in the source region of lunar ultramafic glasses comes from several studies. Neal (2001) investigated the trace element signatures of a variety of mare volcanic products and summarized existing data from lunar ultramafic glasses. The high-Ti basalts and glasses show the influence of ilmenite on their trace element signatures; however the high-Ti glasses also exhibited the

influence of garnet on their trace element signatures; specifically those with Sm/Yb greater than KREEP. Siderophile and chalcophile element compositions also suggest that the source region of the ultramafic glasses had not been involved in the melting event that formed the LMO (Neal, 2001). These same elemental signatures were not observed for the low-Ti glasses, which had trace element signatures consistent with derivation from early LMO cumulates. A further investigation of the garnet signature in mare glasses, including a wider array of garnet influenced elements, was conducted by Neal and Shearer (2004). This study came to similar conclusions, finding the influence of residual garnet in the source for some of the high-Ti ultramafic glasses but not in the source of the low-Ti glasses.

Seismic evidence for the presence of garnet has been proposed from the re-examination of the Apollo seismic data. Khan et al. (2000) and Nakamura (1983) interpret the seismic velocity structure down to 500 km as the solidified magma ocean. An increase in seismic velocity between 500 and 560 km is consistent with a phase transition to a garnet-bearing source in the deeper lunar mantle. One interpretation is that this is primordial lunar mantle. Nakamura (1983) and Khan et al. (2000) interpret the Apollo seismic data to show evidence for regions of partial melt below 1000 km in the deep lunar interior at the present time. Solomon and Longhi (1977) predict this region of partial melt in the deep lunar interior based on their thermal models of the lunar interior that include primordial lunar mantle below the LMO.

Elkins-Tanton et al. (2003) reported garnet as a near-liquidus phase in experiments on an Apollo 15A green glass that was synthesized based on an early electron microprobe analysis from the Apollo 15 green glass sample. This analysis had lower FeO and higher Al_2O_3 and SiO_2 than the subsequent reanalyzed glasses of Delano (1986) and Elkins-Tanton et al. (2003). The presence of garnet in experiments on this bulk composition led to this study.

The LMO will crystallize from the bottom up, regardless of initial depth, and the magma does not saturate with an aluminous phase until the very latest stages of crystallization. The stable aluminous phase at shallow depths is plagioclase feldspar, which floats to form the lunar anorthositic crust. Because of these considerations, models of LMO crystallization have not included garnet as a crystallizing (e.g.

Snyder et al., 1992). Recent studies of the crystallization of bulk lunar compositions have shown that the absence of garnet in the LMO crystallization sequence is correct (e.g. Elardo and Draper, 2009).

The agreement between the seismic data and the thermal models provide circumstantial evidence that the lunar magma ocean did not include the entire lunar mantle, and thus left a primordial mantle at depth. The geochemical data on the high-Ti ultramafic glasses indicates that this primordial lunar mantle includes garnet, and is thus similar in lithology to the garnet lherzolite lithology found in the earth's mantle. The current study will investigate the composition of melts of this primordial lunar mantle and investigate the possible influence these melts had on the derivation of low-Ti mare ultramafic glasses.

Experimental Methods

Experiments on low-Ti green glass compositions from the Apollo 15A glasses, designated by Delano (1979, 1986), were performed in order to investigate the pressure, temperature and phase assemblage of liquidus multiple phase saturation for this compositional group. Analog compositions were also investigated in order to understand the crystallization sequence and to produce experiments that were saturated with a garnet lherzolite phase assemblage (olivine (olv) + orthopyroxene (opx) + clinopyroxene (cpx) + garnet (grt)), with bulk compositions for the experiments similar to lunar ultramafic glasses. The results of these garnet lherzolite saturated experiments can be combined with literature results for garnet lherzolite saturated melts on terrestrial compositions to calibrate a mantle melting model in the garnet stability field. This model can then be used to predict the composition of melts of a primordial lunar mantle to be used in mixing calculations later in the study.

This study was performed in the laboratory for Experimental Petrology at MIT. Starting compositions A15-57 and A15-07 span the CaO and Al_2O_3 compositional variability exhibited by the Apollo 15 green glasses (Table 1). The starting composition A15-07-26 represents a high-CaO and high-Al_2O_3 analog composition to that of A15-07 to investigate the influence of garnet on high-pressure melting relations. These compositions were created by mixing high purity oxides to recreate a given

composition. The oxides were combined in an agate mortar and then ground under ethanol to ensure homogeneity of the mixture. The mixtures were then preconditioned at 1000°C and an fO_2 of the Fe-FeO buffer (Huebner, 1971) in a DelTech vertical gas-mixing furnace (see methods of Barr et al., 2009). This is performed to react the synthetic oxides to anhydrous compounds that will not be hydroscopic under laboratory conditions. Subsequently the conditioned oxide mixtures were stored in a desiccator until use. Starting compositions A15-50/50 and A15-75/25 represent mixtures of green glass compositions and the A15-07-26 composition with 50% A15-07 and 75% A15-57, respectively. A15-09-1 and A15-09-2 were made by mixing green glass starting materials with crystalline mineral phases. A15-09-1 was created by mixing the preconditioned A15-07 oxide mixture with 10% Kragero orthopyroxene and 10% TMO garnet (Table 1). A15-09-2 was created by mixing the preconditioned oxide mix of A15-57 with 10% Fo_{81}olivine, created by mixing synthetic fayalite and forsterite.

Experiments were performed in a ½" Boyd-England style end-loaded piston cylinder apparatus (Boyd and England, 1960) using the hot piston-in technique (Johannes et al., 1971). Each experiment was run in a graphite capsule as per the methods of Barr and Grove (2010). Prior to assembling the experiment, the capsule, packed with starting material, and all MgO spacers were dried in a desiccated drying oven at 120°C for >24 hrs. Immediately prior to beginning the experiment, the material was removed from the oven and cooled to room temperature in a desiccator. The capsule was surrounded by a dense Al_2O_3 sleeve and centered within a graphite furnace using crushable MgO (for capsule diagram see Medard et al., 2008). The experiments utilized sintered witherite pressure cells. This run assembly has been calibrated against the reaction: anorthite + gehlenite + corundum = Ca-tschermak pyroxene (Hays, 1966) and found to require no pressure correction. Pressures are thought to be accurate to ±50 MPa. The temperature was measured by a Type D thermocouple, with no pressure correction applied to the emf. Temperatures are thought to be accurate to ± 10 °C. The studies of Barr and Grove (2010) and Medard et al. (2008) have found that the ambient oxygen fugacity of the above mentioned run assembly is at least one log unit below the quartz – fayalite – magnetite buffer (QFM – 1). Experiments were pressurized to 1 GPa at room temperature, and then the temperature was raised to 865 °C at 100 °C/min. The experiment

was held at these conditions for 6 minutes, then the pressure was increased to the desired value and the temperature was raised to the final run conditions at 50 °C/min. The sample was held at isothermal conditions for the duration of the experiment (Table 2). Experimental durations ranged from 5 to 50 hours. Experimental liquids were quenched in two manners in this study. The first method was by terminating the power to the experiment at the end of the run, producing fast cooling rates that preserved mineral phases and compositions but allowed the glass to devitrify to fine grained crystallites. The second method involved simultaneous decompression to ~ 1 GPa and power termination, which was successful in quenching experimental liquids to glass.

Compositions of the minerals and glasses were analyzed using wavelength dispersive spectrometry on the 5-spectrometer JEOL 733 electron microprobes at the electron microprobe facility at MIT. Natural and synthetic primary and secondary standards were used, and the CITZAF online data correction package was used for all analyses (Armstrong, 1995). The atomic number correction of Duncumb and Reed, Heinrich's tabulation of absorption coefficients, and the fluorescence correction of Reed were used to obtain a quantitative analysis. Analyses were performed with a 15kV accelerating voltage and a beam current of 10nA, utilizing a beam spot size of ~2μm. All glasses analyzed in this study used a 10μm defocused beam, 10nA beam current and 15kV accelerating voltage as per the routine analytical procedure of the facility (e.g. Barr et al., 2009 and Elkins-Tanton et al., 2003). As mentioned above, quenching experiments did not always produce vitreous glass, in which case the liquid crystallized to fine-grained, feathery masses of quench crystals. These areas were measured using the same broad-beam analytical procedure as the glasses, producing glass compositions of similar quality as the well quenched liquids. Mineral and glass analyses are reported in Table 3.

Results

Phase Relations

The high-pressure phase relations for the two green glass compositions and the five green glass analog compositions that were experimentally determined in this study are tabulated in Table 2 and shown in Figure 1. The composition A15-57 was taken from the compositions of Apollo 15 Green Glass Group A from the study of Elkins-Tanton et al. (2003), which used the group nomenclature of Delano (1986). The composition A15-07 represents another composition Group A glass composition with higher CaO wt% and Al_2O_3 wt% than the A15-57 composition. The phase diagrams for these two compositions are show in Figure 1. Both compositions have olv + opx on the liquidus at the MSP, and both compositions show similar MSP pressures and temperatures (~2.1 GPa and ~1520°C). This result confirms the suggestion of Elkins-Tanton et al. (2003) that the trend of the Apollo 15 group A glasses could have been formed by melting an olv+opx source over a small pressure range. Cpx appears in the crystallization assemblage at temperatures below the liquidus at pressures higher than the MSP, although the possible occurrence of cpx at lower pressures and lower temperatures, similar to the phase relations of the 15C compositions of Elkins-Tanton et al. (2003), can not be ruled out. The 15A glass composition investigated by Elkins-Tanton et al. (2003) found garnet as a saturating phase at pressures of 2.5 GPa and temperatures similar to that of the MSP (~2.2 GPa and ~1520°C), however garnet was not found in the experiments for the two Group A green glass compositions of this study.

The experimental composition A15-07-26 represents a modified version of the A15-07 green glass composition, with higher CaO wt% and Al_2O_3 wt% and retaining the same Mg# (0.64) (Table 1). This composition was estimated to be in equilibrium with garnet lherzolite at 2.6 GPa, using the algorithm of Ebert and Grove (2005). The A15-07-26 composition has olv on the liquidus at 2.6 GPa, with cpx and grt appearing together at 1430°C. The composition also showed saturation with olv + cpx + grt at 2.8 GPa and 1460°C. Orthopyroxene was not observed in the experiments performed using the A15-07-26 composition.

Experiments on the A15-50/50 composition were performed at 2.6 GPa, with one experiment at 2.8 GPa, and experiments on the A15-75/25 composition were performed at 2.3 GPa. Olv was followed by cpx and then by grt in the experiments on A15-50/50. Experiment C416 illustrates the same olv + cpx + grt phase assemblage at 2.8 GPa also. Opx was not observed in any of the experiments on A15-50/50. The experiments on the A15-75/25 resembled the experiments on A15-07, with opx on the liquidus at 2.3 GPa followed by olv. Experiment C428 shows the loss of opx as a crystallizing phase and the appearance of cpx. The disappearance of opx following saturation with cpx is also seen in the lower temperature experiments on A15-57 at 2.3 GPa. Garnet becomes a saturating phase in the A15-75/25 experiments following the appearance of cpx. This suggests that perhaps the green glass compositions could also be saturated with grt at sufficiently low temperatures at 2.3 GPa, however it may be in the subsolidus region.

Work on the above compositions illustrated the need to saturate the green glass composition with grt and opx, which led to the creation of composition A15-09-1, which is A15-07 plus 10% opx and 10% grt. Experiments using this composition were run at 2.35 GPa and 2.4 GPa, with temperatures between 1420°C and 1460°C. Experiment C433 contains olv + cpx, exhibiting the complete dissolution of the added crystalline material and full equilibration of the experiment. Experiments C434 and C435 were run for similarly long run times and resulted in olv + cpx + opx + grt assemblages. The opx and grt compositions of these two runs are distinctly different than the compositions of the added crystals, further illustrating the validity of the observed assemblage in these two experiments.

Composition A15-09-2 is a mixture of A15-57 and 10% liquidus olv (Fo_{81}). Experiments were performed at 2.6 GPa and temperatures between 1440°C and 1480°C. The phase relations illustrate a coexistence of olv + cpx + opx at 1480°C, which is joined by garnet at 1460°C in experiment C436. At temperatures below 1460°C, opx is no longer a saturating phase.

As mentioned before, this study employed two different quenching methods for the high pressure phase equilibrium experiments. Method one produced devitrified glass and method two produced well quenched glasses representing the experimental melt compositions. Method two was used to preserve glass in critical experiments, however the decompression led to the destabilization of garnet upon quench

in many of the runs. The high temperature and sudden pressure drop caused the garnets to decompose to Cr-spinels and a non-stoichiometric Al-rich melt phase. The garnet decomposition was only observed for experiments employing quench method two, and experiments employing quench method one, which reproduced the conditions of runs that showed the garnet decomposition products all contained garnet as an equilibrium phase. This garnet decomposition has also been verified in the experiments on high-Ti lunar glass compositions of Krawczynski and Grove (2008).

High-Pressure Melting Relations

Experiments C434 and C435 both yielded liquids in equilibrium with a garnet lherzolite mineral assemblage. Both of these experiments were performed at 2.35 GPa, but the temperature was different by 20°C, resulting in a higher degree of melting in the higher temperature experiment, C435. The differences in the melt compositions from the two experiments, along with the compositions of the coexisting mineral phases, can be used to determine the relative change in the proportions of each mineral phase and the proportion and composition of the melt. The coefficients of the melting reaction and the instantaneous melt composition produced by melting a garnet lherzolite can be obtained by linearly regressing the melt compositions from the lower temperature experiment to the melt and silicate phase compositions of the higher temperature experiment. The results of this method can then be normalized to a single unit of melt produced, which yields the proportion of each mineral phase that contributed to the melting reaction (Eq. 1).

1.3 Olv + 3.6 Cpx + 0.6 Grt → 1.0 Liquid + 4.4 Opx Eq. 1

The calculated melting reaction for garnet lherzolite at 2.35 GPa indicates that melt + cpx + grt + olv react to produce melt + opx. These melting relations were also identified in the study of Longhi (1995) for melting garnet lherzolite. This melting reaction can be understood by comparing liquid and mineral compositions of the garnet lherzolite saturated experiments as projected in a pseudoternary phase

diagram (Figure 2). When opx + olv + cpx are in equilibrium with a liquid composition that lies outside of the composition-space bounded by those phases there is a reaction between the liquid and solid phases. For the bulk compositions in this study, the reaction consumes olv + cpx and produces melt + opx. This reaction topology can be observed in the experiments for compositions A15-75/25 and A15-09-2 (Figure 1). For these bulk compositions, which crystallize opx as a liquidus phase at high pressure, experiments of progressively lower temperature at given high pressure result in the eventual disappearance of opx from the phase assemblage. In the case of composition A15-75/25, the opx was not stable at sufficiently low temperatures so as to stabilize grt, whereas in A15-09-2 the composition was created to stabilize opx to a low enough temperature to allow for coexistence with grt.

Pyroxene Compositions

The pyroxene compositions observed in the experiments performed for this study are similar to those produced in previous investigations of the Apollo 15 green glasses (Elkins-Tanton et al., 2003 and Draper et al., 2006). Clinopyroxenes observed in our high pressure experiments have variable Wo (Ca/(Mg+Ca+Fe) moles) contents that correlate positively with the D^{px}_{melt} Al_2O_3 (Figure 3). The cpxs contain between 2.84 wt% and 7.29 wt% Al_2O_3, with Wo contents from 0.11 to 0.33. The opx exhibit a similar range in Al_2O_3 contents, 2.29 wt% to 5.91 wt%, and a range in Wo contents from 0.03 to 0.05. For experiments with coexisting opx and cpx the QUILF algorithm (Anderson et al., 1993) can be used to estimate a temperature of equilibration. The temperatures obtained by using this algorithm agree well with the known experimental temperatures, except for C362, (Table 4), confirming that the duration of the experiments were sufficient to approach equilibrium for these experiments.

Phase Fe-Mg K_D Values

The equilibrium distribution coefficient for Fe and Mg between olv and melt ($K_D^{Fe\text{-}Mg}{}_{Olv\text{-}M}$ = (Mg_{Melt} x Fe_{Olv}) / (Mg_{Olv} x Fe_{Melt}) molar) can be calculated for many of the experiments of this study.

Previous experimental investigations on lunar ultramafic glasses have found that the K_D values for the low-Ti ultramafic glasses are higher than the canonical value of 0.30 ± 0.03 determined for olv in terrestrial basalts by Roeder and Emslie (1970). The average K_D for olv in this study is 0.356 ± 0.030 (1σ), which agrees with past experimental work on lunar green glasses and low-Ti mare basalts (e.g. Elkins et al., 2000 and Longhi et al, 1978). The K_D values for opx and cpx are 0.324 ± 0.024 (1σ) and 0.349 ± 0.035 (1σ) respectively.

Discussion

Origin of the Apollo 15 Green Glass Compositional Trends

The studies by Elkins et al. (2000) and Elkins-Tanton et al. (2003) have investigated the major element variations in the green glasses of Apollo 14 and Apollo 15. Their work built on the investigations of Delano (1986), and confirmed the range in ultramafic glass compositions observed by earlier work. These two studies also performed phase equilibrium experiments on green glass compositions to determine the depth and temperature of generation. The results of these two studies concluded that the low-Ti glasses formed by assimilation of magma ocean cumulates over a range of depths, giving rise to liquidus MSP at pressures from 1.4 GPa to 2.2 GPa. In order to assimilate cumulates over this range of depths, melts must be produced at greater pressures and then migrate through the LMO cumulate pile. Based on the limited chemical variation observed in the major element compositions of the group A glasses of Apollo 15 (15A), Elkins-Tanton et al. (2003) suggested that these glasses may have formed from a simple melting process, thus providing a source of initial melts for cumulate assimilation to form the group B and C glasses.

The two 15A green glass compositions investigated in this study, A15-57 and A15-07, span the compositional range observed for this group of ultramafic glasses from Apollo 15 (Table 1). Both compositions display olv+opx MSPs at identical conditions, 2.1 GPa and 1520 °C, which is very similar

to the result obtained by Elkins-Tanton et al. (2003) for the preliminary group A composition they investigated. This confirms the suggestion by Elkins-Tanton et al. (2003) that the 15A glasses may have formed from a process that occurred at 2.1 GPa, with subsequent assimilation of magma ocean cumulates to give rise to the group B and group C glasses.

In the following discussion we will use our new phase equilibrium results to further develop a petrogenetic model for the origin of the Apollo 15 Group A, B and C glasses. The major addition from our work is to provide a quantitative estimate of the major element composition of melts of a deep primordial lunar interior that may have interacted with and assimilated magma ocean cumulates to form the Apollo 15 green glasses. Our study also considers an alternative model to form the Apollo 15 green glasses by deep melting of hybridized lunar mantle mineral assemblage. Further work is still needed in order to discriminate between the two models for the formation of the Apollo 15 green glass.

Generating the 15A and 15C Glasses

The study of Elkins-Tanton et al. (2003) has suggested that the 15A and 15C MSPs could represent the final depth of equilibration of a deep primordial melt with magma ocean cumulates. If a primordial melt has undergone significant fractionation or assimilation, the significance of liquidus MSPs is diminished due to the dependence of the MSP on the liquid Mg# and alkali content (Kinzler and Grove, 1992; Asimow and Longhi, 2004). At a constant pressure, liquids with higher Mg#s will have a larger olv primary phase volume than those of lower Mg#s, at constant NaK#, which is calculated as the $Na_2O + K_2O$ / ($Na_2O + K_2O + CaO$) all in wt units (Kinzler and Grove, 1992). The expansion of the olv primary phase volume is also observed as the pressure of melt generation is decreased (e.g. Kinzler and Grove, 1992). The 15C glass compositions have higher Mg#s than those of the 15A green glasses, both with similar range of NaK#s, and the observed liquidus MSP for the 15C composition (Elkins-Tanton et al., 2003) is at a shallower depth than that of the 15A compositions (Figure 1). The relationship of the liquidus MSP pressures and the green glass Mg#s could be the result of assimilation of magma ocean cumulates at different pressures; however the relationship could also be consistent with assimilation of a

single batch of magma ocean cumulates at a constant pressure, whereby the cumulate assemblage becomes more refractory, increasing the Mg#, as assimilation progresses. Because a residual cumulate mineral assemblage involving olv and pyroxenes evolves to higher Mg#s as it partially melts, the production of both 15A and 15C compositions at a similar depth is possible. Additionally, if the two compositions were formed from cumulate assimilation by melts coming from a common depth and source, the additional decompression of the deep melts would lead to an decrease in the temperature of the melts. The decreased temperature should be reflected in the temperature of the MSP if the 15C primordial melts assimilated cumulates at a shallower depth than the 15A primordial melts. Additionally, due to the higher Mg# of the 15C glasses, the lower temperature of the influxing primordial melt would decrease the ability to assimilate refractory magma ocean cumulates; however, assimilation of more evolved cumulates could still be achievable. Because the liquidus MSP pressure and temperature, and possibly the mineralogy too, can be perturbed by the assimilation process, the MSPs can only be used as a loose guide to the range of conditions involved in the production of the Apollo 15 green glasses.

Testing the Origin of the 15A and 15C Green Glasses

To test the hypothesis that the 15A and 15C glass compositions could be the result of assimilation of magma ocean cumulates, this study has chemically modeled mixtures of deep melts of a primordial lunar mantle with a magma ocean cumulate assemblage that includes olv+opx+cpx. The lunar thermal models of Solomon and Longhi (1977) indicate the presence of partial melts of primordial lunar mantle at depths below the lower extent of the magma ocean. The primordial material is inferred to be a garnet lherzolite similar to that found in the Earth's mantle, and the melting model of Ebert and Grove (2005) can be supplemented with the experimental data of this study and used to calculate melts of this lithology.

A. Modeling Melts of Primordial Lunar Mantle

The results of this study include three experiments that have melt in equilibrium with a garnet lherzolite mineral assemblage: C434, C435, and C436. These experiments were performed using starting

materials that were similar to lunar green glass compositions, thus providing a better analog to modeling lunar garnet lherzolite melting than experiments on terrestrial compositions. The model of Ebert and Grove (2005) used the available literature data for terrestrial garnet lherzolite melt compositions to calibrate a lherzolite melting model similar in formulation to that of Kinzler and Grove (1992). Incorporation of the experimental data of this study extends the calibration data set to include lunar relevant compositions, and it also improves the overall fit of the modeling parameters.

This garnet lherzolite melting model requires inputs that are based on the composition of the melts of interest (Ebert and Grove, 2005). The inputs include the NaK#, the Mg#, and the pressure of the melt compositions to be calculated by the model. The model calculates the temperature and major element composition of the garnet lherzolite saturated melt that has the prescribed Mg# and NaK#. This study uses the Taylor Whole Moon (TWM) composition of Taylor (1982) to represent the NaK# and the Mg# of the primordial mantle melts.

The temperature of the MSPs for the 15A and 15C green glass compositions, 1520 °C, provides a lower bound for the estimated temperatures of the primordial melts. Melt temperature estimates, using the TWM composition, are only above 1520 °C for pressures at or above 3.0 GPa. The mixing calculations discussed below will only consider these melts that are predicted to have temperatures above 1520 °C. As pointed out by Elkins-Tanton et al. (2003), if the 15A glasses and the 15C glasses are formed via a similar process the heat and mass transfer must be decoupled to allow both to have liquidus MSPs at the same temperature despite the 0.7 GPa pressure difference between the two. Thus we do not attempt to constrain the energy balance of the assimilation process.

B. Modeling the Cumulate Assimilant

The cumulate mineral phase compositions used in our mass balance models were all assumed to be in Fe-Mg equilibrium with a common liquid, simulating the crystallization of the phases from the same parental magma ocean melt. The Mg# of this common liquid is used as a variable in the mass balance calculations, and bulk assimilation of the cumulate phases is assumed. The average Fe-Mg $K_D^{melt}{}_{liq}$ values

for the mineral phases determined by the experiments of this study are used to calculate the Fe-Mg contents of the mineral phases in the assimilated cumulate. The CaO and Al_2O_3 contents of the cpx varied with temperature in the experiments of this study, so mixtures were performed using values consistent with the lower temperature experiments in order to more closely represent a cumulate cpx. The initial CaO and Al_2O_3 content for the cpx was set at 9.6 wt% CaO and 4.5 wt% Al_2O_3, however the final CaO and Al_2O_3 wt% for the pyroxenes used in the mixing calculations varied slightly in order to maintain cation stoichiometry according to the Mg# of the pyroxene.

C. Successful Mixing Calculations

Table 5 and Table 6 summarize the mixtures that have been calculated for garnet lherzolite melts of 3.2 GPa and 3.7 GPa and the cumulate assemblage required to mass balance with the Apollo 15 green glass compositions of A15-57 (Table 1) and A15-10C of Elkins-Tanton et al. (2003). These mixtures reproduce SiO_2, Al_2O_3, CaO, FeO, and MgO within 0-1.5% in most cases. Minor elements (Cr_2O_3, TiO_2, MnO, and K_2O) are not included in the calculation of the garnet lherzolite liquid composition and are expected to strongly vary in the pyroxenes according to the composition of the liquid from which they crystallize, so these were not considered during the mass balance calculations.

Garnet lherzolite melts that retain the Mg# and NaK# of the TWM composition are calculated to occur at 1539 °C at 3.2 GPa and 1581 °C at 3.7 GPa. The high pressure melts have lower Al_2O_3 and CaO contents and higher SiO_2 contents than those from lower pressures. This results in a lower proportion of the primordial melt needed to reproduce the green glass composition when the melt is derived from shallower levels. Both the 15A and 15C compositions require 37-38% primordial melt from 3.2 GPa, but they require 46% primordial melt from 3.7 GPa. Because of the high prescribed Mg# of the primordial melt, the cumulate assemblages needed to mass balance the primordial melt and the green glasses represent mineral composition that crystallized from an evolved magma ocean liquid. Such a cumulate would have originally resided at shallower depths than the MSPs of either the 15A or 15C glasses.

For the 15C composition, the Mg# of the liquid parental to the cumulate ranges from 0.33 at 3.2 GPa to 0.29 at 3.7 GPa, and the 15A composition the Mg#s range from 0.26 at 3.2 GPa to 0.23 at 3.7 GPa. The total MgO + FeO for the primordial melt drops as pressure drops, which serves to raise the bulk Mg# of the cumulates needed to mass balance with the green glass compositions. The modal proportions of the cumulus phases needed in the mass balance show little variation between the two pressures; however, the difference in phase proportions needed to reproduce the two green glass compositions is apparent. The 15C glass composition has a higher SiO_2 content and Mg# than the 15A composition, which requires a greater proportion of pyroxene and lower proportion of olivine in the cumulate assemblage. The 15C composition only requires 1-4% olv whereas the 15A composition requires 10-11% olv to complete the mass balance. The near lack of olv in the assimilated 15C cumulate, compared to the 15A assemblage, accounts for the higher SiO_2 of the 15C group and can be used to explain the lower total Ni and Co in the 15C group compared to the 15A compositions (Figures 4 and 5). It is also worth noting that the differences hereby attributed to olivine in the assimilant component of the 15A and 15C compositions could also represent an effect of variable amounts of olivine remaining in the source of the original melts or subsequent olivine fractionation as well.

Evolved Cumulates Deep in the Moon

The thermal models of Solomon and Longhi (1977) predict that as the LMO solidified, the zone of partial melt in the interior of the moon, where the primordial material underlies the LMO, would migrate to greater and greater depths. The heat provided by magma ocean solidification would be transferred to the primordial material, thus providing an isobaric batch melting scenario, which is directly mimicked by the phase equilibrium experiments of this study. As assumed in the mass balance calculations discussed above, the deep primordial melt would have a high Mg# due to the primordial nature of the mantle not involved with the magma ocean. In order to derive the green glass compositions of Apollo 15, or any of the ultramafic glasses, from mixing with the melts of the primordial mantle, the other mixing component would need to have an evolved composition. The lunar magma ocean would

crystallize from the interior outward, which would place the most primitive cumulates at the greatest depths, however many researchers have called upon cumulate overturn to deliver evolved cumulate mineral assemblages to great depths within the moon (e.g. Hess and Parmentier, 1995). This scenario would be required in order to produce the green glass compositions at Apollo 15, because the compositions of these cumulate would have crystallized at shallow depths in the magma ocean.

Eu Anomalies

A comprehensive study of the rare earth element compositions of the lunar ultramafic glasses and mare basalts by Shearer and Papike (1993) found a pervasive negative Eu anomaly for all of the investigated samples (Shearer and Papike, 1993). The negative Eu anomaly in lunar samples has long been described as a consequence of the remelting of Fe-Mg cumulates that sank in the magma ocean while co-crystallizing plagioclase floated to form a plagioclase-rich crust at the top of the magma ocean (e.g. Wood et al. 1970 and Smith et al., 1970). Plagioclase is thought to appear very late in the magma ocean crystallization sequence (> 90 % fractional crystallization), and the negative Eu anomaly would not have occurred in cumulates earlier in the magma ocean sequence. The ultramafic glasses may have acquired the negative Eu anomaly through assimilation of the late-stage magma ocean cumulates; however the mineralogy of the late-stage magma ocean cumulate is unlikely to contain olv, opx and cpx and should contain a high-Ti mineral phase. An additional mechanism for producing the small negative Eu anomaly is for the ultramafic melts to interact with a rare earth element enriched reservoir that preserves a negative Eu anomaly. The lunar KREEP geochemical reservoir has these characteristics and is expected to occur at shallow depths below the lunar surface, where the rising ultramafic magmas would have their greatest excess heat from adiabatic decompression.

A sample of the KREEP reservoir has not been identified; however, the lunar basalt 15386 represents a KREEP-rich basalt and can serve as a diluted representation of the KREEP geochemical reservoir (e.g. Neal and Kramer, 2003). The green glasses of Apollo 15 have low concentrations of many trace and rare earth elements, and interaction with an enriched reservoir could mask the original

abundances of these elements. Neal (2001) uses Sc/Sm vs. $[Sm/Yb]_N$ ($[\ ]_N$ = normalized to C1-Chondrite of Sun and McDonough (1989)) to indicate the influence of KREEP addition on lunar mare basalts and ultramafic glasses. The data of Shearer and Papike (1993) indicate a possible influence of the KREEP reservoir on the trace element composition of the Apollo 15 green glasses (Figure 6). Additionally, the 15A glasses have the smallest Eu anomalies and the 15E glasses have the largest Eu anomalies (Shearer and Papike, 1993), indicating that the Eu anomalies are positively correlated with the apparent level of KREEP influence shown by the trend in Figure 6. The presence of a KREEP component in the ultramafic glass compositions could indicate temporary storage at a shallow depth where the glasses would have interacted with the KREEP material.

Hybrid Mantle Source for Apollo 15 Green Glasses

The interaction with KREEP allows for the possibility of small amounts of shallow crystal fractionation of olivine. Starting composition A15-09-2 represents a 15A green glass composition plus liquidus olv. This simulates a reverse fractionation of the green glass composition at low pressure, where olv would have been the only stable phase near the liquidus. The fractionation of olivine could have occurred by melt-rock reaction on the rise to the surface or by stalling at shallow depths prior to eruption. Both of these scenarios allow for limited interaction with a KREEP reservoir and sufficient amounts of olivine fractionation. With the additional olv added to the starting composition, the bulk composition is in equilibrium with a garnet lherzolite assemblage below its liquidus at high pressure (Figure 1). This suggests that the green glass composition could represent melts of garnet lherzolite that melted to a sufficiently high extent so as to consume the grt + cpx, leaving an olv + opx residue. Figure 1 illustrates that cpx is found in the sub-liquidus region near the MSP for the green glass compositions, suggesting that the liquid is not far from being saturated with cpx. This is consistent with the residue having experienced only a small degree of melting beyond the exhaustion of the cpx.

Additionally, the disappearance of opx from the stable phase assemblage in the lowest temperature experiments on compositions A15-09-2 (Figure 1) also indicates that the original mineral

assemblage may have been olv + cpx + grt or even just cpx + grt, since olivine is no longer observed in the lowest temperature experiments on the green glasses at high pressure (Figure 1). The mineral phases observed in experiment C436 are too Fe-rich to represent primordial lunar mantle phases, thus indicating that the required grt-lherzolite must have been formed through another process. Elardo and Draper (2009) demonstrate that grt is not a crystallizing phase in a lunar magma ocean, so the derivation of the Apollo 15 green glasses from a lithology involving grt would not represent a primary LMO cumulate mineral assemblage. A hybrid mantle formed from mixtures of Mg-Fe silicates, supplemented with plagioclase feldspar or an Al + Ca enriched trapped liquid, can produce the require phase assemblages indicated above if equilibrated at subsolidus conditions at elevated pressures. This hybrid mantle lithology could have melted over a range of pressures with the liquids undergoing small amounts of olivine fractionation on their way to being erupted to produce the Apollo 15 green glasses. The interaction of a primordial mantle melt with the cumulate lithologies is not required; however, emplacement of batches of deep primordial melts may help to provide heat for the melting of the overturned cumulate lithologies even if they do not contribute chemically to their composition (Figure 7).

Mixed Magma Origin for 15B Glasses

Steele et al. (1992) attempted to model the Apollo 15 group B (15B) glass trend, both major and trace elements, as a batch equilibrium melting model. These models assumed a pyroxene-rich and oxygen-poor source, whereby the fO_2 of the source was sufficiently low as to allow Ni and Co to act as incompatible elements in the pyroxene. These models successfully reproduced the major and trace element characteristics of the 15B compositions, however they heavily rely upon the bulk $D_{Ni}<1$ and $D_{Co}<1$. The phase equilibrium results of Elkins et al. (2000), Elkins-Tanton et al. (2003) and the current study display high-pressure MSPs with olv+opx for all the investigated green glass compositions. Ni and Co are both strongly compatible in olv and olv is a large proportion of the phase assemblage at the MSPs, which invalidates the required assumption of the incompatible behavior of Ni and Co for the Steele et al. (1992) models. The increase in NiO with a decrease in MgO along the 15B trend, shown by the study of

Elkins-Tanton et al. (2003), rules out a simple melting or fractionation origin for the Apollo 15 green glasses.

Elkins-Tanton et al. (2003) argues that the relationships between the 15A, 15B, and 15C ultramafic glasses are most consistent with a process that involves assimilation of magma ocean cumulates over a range of depths. The decrease in NiO concentration as the MgO content increases in the Apollo 15 green glasses led Elkins-Tanton et al. (2003) to suggest that the 15A glasses may represent the parental melts that underwent assimilation to form the 15B and 15C glasses. However, the Elkins-Tanton et al. (2003) study, in their Figure 8, does not rule out the possibility that there is a deeper primordial melt that was involved in assimilation to produce each of the Apollo 15 green glass groups independently.

An alternative method by which the 15B glass compositions may be produced is by mixing an end-member composition of the 15A and 15C glasses (Figure 4). This simple process can reproduce the major element trends of the 15B glasses; however, evaluating this process using trace elements is difficult. The trace element data of Shearer and Papike (1993) are consistent with the 15B glasses being formed by mixing end members of the 15A and 15C glass groups; however, the data of Steele et al. (1992) appears to indicate higher Sm abundances for the 15B glasses than if they were mixtures between 15A and 15C compositions (Figure 8). When the Ni and Co data from Steele et al. (1992) are compared to the Ni and Co data from Shearer and Papike (1993) and Shearer et al. (1996), it becomes apparent that they do not agree for each of the Apollo 15 green glass compositional groups, suggesting that both data sets systematically differ for both high and low concentration trace elements (Figure 5). The discrepancy in the two datasets indicates that either the Steele et al. (1992) data is over estimating the concentrations of some of the trace elements, such as Sm, Ni and Co, or the Shearer and Papike (1993) and Shearer et al. (1996) studies, which agree well between themselves, are under estimating the values for these same trace elements. Until further studies can resolve this discrepancy, the production of 15B glass compositions from mixing of 15A and 15C melts is still a possible scenario. The subsequent portions of this study will focus on generating the 15A and 15C melt compositions; however, the same methods may be used to

produce the compositional range exhibited by the 15B glasses if they are shown at a later date to not have been formed by mixing of 15A and 15C melts.

Conclusions

Experiments on Apollo 15 green glass compositions produce liquidus MSPs with olv + opx at 2.1 GPa and 1510°C. Further experiments on compositions similar to the green glasses produced melts in equilibrium with a garnet lherzolite phase assemblage. Three experiments that produced melt + olv + opx + cpx + grt are used to calibrate a mantle melting model, which can then be used to estimate the major element compositions of melts of a primordial, unaffected by a magma ocean, lunar mantle. Mixtures of primordial melts, from 3.2 to 3.7 GPa, and evolved magma ocean cumulates, olv + cpx + opx, recreate the chemical compositions of the Apollo 15A and 15C green glasses. The availability of evolved magma ocean cumulates at pressures of 2.1 GPa indicate that cumulate overturn must have occurred following the crystallization of the LMO. Experiments on a 15A glass composition with a small amount of added olivine, indicates the possible derivation of the green glass magmas as high degree melts of garnet lherzolite at 2.6 GPa that later underwent ~10% olv fractionation at shallow depth. The more Fe-rich nature of the experimentally produced phases suggests that the grt-lherzolite was formed by subsolidus reequilibration of evolved LMO cumulates that were overturned to great depths within the LMO. Further work is required to distinguish between the two formation mechanisms, cumulate assimilation and reequilibrated cumulate melting, and to determine the possible role of primordial lunar mantle in the formation of mare ultramafic glasses.

Bibliography

Andersen, D.J., Lindsley, D.H., and Davidson, P.M., 1993, Quilf - a Pascal program to assess equilibria among Fe-Mg-Mn-Ti oxides, pyroxenes, olivine, and quartz: Computers & Geosciences, v. 19, p. 1333-1350.

Armstrong, J.T., 1995, Citzaf - a package of correction programs for the quantitative Electron Microbeam X-Ray-Analysis of thick polished materials, thin-films, and particles: Microbeam Analysis, v. 4, p. 177-200.

Asimow, P.D., and Longhi, J., 2004, The Significance of Multiple Saturation Points in the Context of Polybaric Near-fractional Melting: Journal of Petrology, v. 45, p. 2349-2367.

Barr, J.A., and Grove, T.L., 2010, AuPdFe Ternary Solution Model and Applications to Understanding the fO2 of Hydrous, High-Pressure Experiments: Contributions to Mineralogy and Petrology, v. In press.

Barr, J.A., Grove, T.L., and Wilson, A.H., 2009, Hydrous komatiites from Commondale, South Africa: An experimental study: Earth and Planetary Science Letters, v. 284, p. 199-207.

Boyd, F.R., and England, J.L., 1960, Apparatus for phase equilibrium studies at pressures up to 50 kilobars and temperatures up to 1750 °C Journal of Geophysical Research, v. 65, p. 741-748.

Delano, J.W., 1979, Apollo 15 green glass: Chemistry and possible origin: Proceedings of the 10th Lunar and Planetary Science Conference, p. 275-300.

Delano, J.W., 1986, Pristine lunar glasses: Criteria, data, and implications: Proceedings of the 17th Lunar and Planetary Science Conference, p. D201-D213.

Draper, D.S., duFrane, S.A., Shearer Jr., C.K., Dwarzski, R.E., and Agee, C.B., 2006, High-pressure phase equilibria and element partitioning experiments on Apollo 15 green C picritic glass: Implications for the role of garnet in the deep lunar interior: Geochemica et Cosmochimica Acta, v. 70, p. 2400-2416.

Ebert, E., and Grove, T.L., 2005, Systematics of garnet peridotite melting: New experimental constraints: Geophysical Research Abstracts, v. 7, p. EGU05-A-08306.

Elardo, S.M., and Draper, D.S., 2009, Crystallization of a Lunar Magma Ocean: Preliminary Experimental Results: Proceedings of the 40th Lunar and Planetary Science Conference, p. No. 1181.

Elkins, L.T., V.A., F., Delano, J.W., and Grove, T.L., 2000, Origin of lunar ultramafic green glasses: Constraints from phase equilibrium studies: Geochemica et Cosmochimica Acta, v. 64, p. 2339-2350.

Elkins Tanton, L.T., Chatterjee, N., and Grove, T.L., 2003, Experimental and petrological constraints on lunar differentiation from the Apollo 15 green picritic glasses: Meteoritics and Planetary Science, v. 38, p. 515-527.

Galbreath, K.C., Shearer, C.K., Papike, J.J., and Shimizu, N., 1990, Inter- and intra-group compositional variations in Apollo 15 pyroclastic green glass: Geochemica et Cosmochimica Acta, v. 54, p. 2565-2574.

Grove, T.L., and Juster, T.C., 1989, Experimental investigations of low-Ca pyroxene stability and olivine-pyroxene-liquid equilibria at 1-atm in natural basaltic and andesitic liquids: Contributions to Mineralogy and Petrology, v. 103, p. 287-305.

Hays, J.F., 1966, Lime-alumina-silica, Year Book - Carnegie Institution of Washington, p. 234-239.

Hess, P.C., and Parmentier, E.M., 1995, A model for the thermal and chemical evolution of the Moon's interior: Implications for the onset of mare volcanism: Earth and Planetary Science Letters, v. 134, p. 501-514.

Huebner, J.S., 1971, Buffering Techniques for Hydrostatic Systems at Elevated Pressures, *in* Ulmer, G.C., ed., Research Techniques for High Pressure and High Temperature: New York, Springer-Verlag, p. 123-177.

Johannes, W., Chipman, D.W., F., H.J., Bell, P.M., Mao, H.K., Newton, R.C., Boettcher, A.L., and Seifert, F., 1971, An interlaboratory comparison of piston-cylinder pressure calibration using the albite-breakdown reaction Contributions to Mineralogy and Petrology, v. 32, p. 24-38.

Khan, A., Mosegaard, K., and Rasmussen, K.L., 2000, A new seismic velocity model for the moon from Monte Carlo inversion of the Apollo Lunar Seismic Data: Geophysical Research Letters, v. 27, p. 1591-1594.

Kinzler, R.J., and Grove, T.L., 1992, Primary magmas of mid-ocean ridge basalts 2. Applications: Journal of Geophysical Research-Solid Earth, v. 97, p. 6907-6926.

Koga, K.T., Shimizu, N., and Grove, T.L., 1998, Disequilibrium trace element redistribution during garnet to spinel facies transformations, Proceedings of the 7th International Kimberlite Conference, MIT/WHOI, p. 444-451.

Krawczynski, M.J., and Grove, T.L., 2008, Experimental Investigation of the fO2 Effects on Apollo 17 Orange Glass Phase Equilibrium: Proceedings of the 39th Lunar and Planetary Science Conference, p. No. 1231.

Longhi, J., 1992, Experimental petrology and petrogenesis of mare volcanics: Geochemica et Cosmochimica Acta, v. 56, p. 2235-2251.

Longhi, J., 1995, Liquidus equilibria of some primary lunar and terrestrial melts in the garnet stability field: Geochemica et Cosmochimica Acta, v. 39, p. 2375-2386.

Longhi, J., Walker, D., and Hays, J.F., 1978, The distribution of Fe and Mg between olivine and lunar basaltic liquids: Geochemica et Cosmochimica Acta, v. 42, p. 1545-1558.

Médard, E., McCammon, C.A., Barr, J.A., and Grove, T.L., 2008, Oxygen fugacity, temperature reproducibility, and H2O contents of nominally anhydrous piston-cylinder experiments using graphite capsules: American Mineralogist, v. 93, p. 1838-1844.

Meyer, C., McKay, D.S., Anderson, D.H., and Butler, P.J., 1975, The source of sublimates on the Apollo 15 green and Apollo 17 orange glass samples: Proceedings of the 6th Lunar Science Conference, p. 1673-1699.

Nakamura, Y., 1983, Seismic velocity structure of the lunar mantle: Journal of Geophysical Research, v. 88, p. 677-686.

Neal, C.R., 2001, Interior of the Moon: The presence of garnet in the primitive deep lunar mantle: Journal of Geophysical Research, v. 106, p. 27865-27885.

Neal, C.R., and Kramer, G., 2003, The composition of KREEP: A detailed study of KREEP basalt 15386: Proceedings of the 34th Lunar and Planetary Science Conference, p. No. 2023.

Neal, C.R., and Shearer, C.K., 2004, Garnet in the Lunar Mantle: Further Evidence from Volcanic Glasses: Proceedings of the 35th Lunar and Planetary Science Conference, p. No. 2135.

Nunes, P.D., Tatsumoto, M., and Unruh, D.M., 1974, U-Th-Pb systematics of some Apollo 17 lunar samples and implications for a lunar basin excavation chronology: Proceedings of the Fifth Lunar Conference, v. 2, p. 1487-1514.

Shearer, C.K., and Papike, J.J., 1993, Basaltic magmatism on the Moon: A perspective from volcanic picritic glass beads: Geochemica et Cosmochimica Acta, v. 57, p. 4785-4812.

Shearer, C.K., Papike, J.J., and Layne, G.D., 1996, Deciphering basaltic magmatism on the moon from the compositional variations in the Apollo 15 very low-Ti picritic magmas: Geochemica et Cosmochimica Acta, v. 60, p. 509-528.

Smith, J.V., Anderson, A.T., Newton, R.C., Olsen, E.J., Wyllie, P.J., Crewe, M.S., Isaacson, M.S., and Johnson, D., 1970, Petrologic history of the Moon inferred from petrography, mineralogy, and petrogenesis of Apollo 11 rocks: Proceedings of the Apollo 11 Lunar Science Conference, p. 897-925.

Snyder, G.A., Taylor, L.A., and Neal, C.R., 1992, A chemical model for generating the sources of mare basalts: Combined equilibrium and fractional crystallization of the lunar magmasphere: Geochemica et Cosmochimica Acta, v. 56, p. 3809-3823.

Solomon, S.C., and Longhi, J., 1977, Magma oceanography: 1. Thermal evolution: Proceedings of the 8th Lunar Science Conference, p. 583-599.

Steele, A.M., Colson, R.O., Korotev, R.L., and Haskin, L.A., 1992, Apollo 15 green glass: Compositional distribution and petrogenesis: Geochemica et Cosmochimica Acta, v. 56, p. 4075-4090.

Sun, S.S., McDonough, W.F., 1989, Chemical and isotopic systematics of oceanic basalts; implications for mantle composition and processes. In: A.D. Saunders and M.J Norry, Editors, Magmatism in the Ocean Basins, vol. 42, Geological Society of London, p. 313-345.

Taylor, S.R., 1982, Planetary Science: A Lunar Perspective: Houston, TX, Lunar and Planetary Institute, 481 p.

Tormey, D.R., Grove, T.L., and Bryan, W.B., 1987, Experimental petrology of normal MORB near the Kane Fracture Zone: 22°-25°N, mid-Atlantic ridge: Contributions to Mineralogy and Petrology, v. 96, p. 121-139.

Wood, J.A., Dickey, J.S., Marvin, U.B., and Powell, B.N., 1970, Lunar anorthosites and geophysical model of the moon: Proceedings of the Apollo 11 Lunar Science Conference, p. 965-988.

Table 1. Compositions of starting materials used in this study. The composition of Kragero Opx is from Grove and Juster, 1989 and TMO Garnet is from Koga et al., 1998. See text for a detailed description of the starting mixtures.

	A15-57	A15-07	A15-07-26	A15-50/50	A15-75/25	A15-09-1	A15-09-2	Kragero Opx[a]	TMO Garnet[b]
SiO_2	45.74	45.4	44.3	45.02	45.13	46.19	45.1	57.3	42.4
TiO_2	0.39	0.35	0.35	0.37	0.35	0.3	0.35	0.06	0.16
Al_2O_3	7.22	7.75	12.01	9.62	8.82	8.55	6.5	0.1	23.7
Cr_2O_3	0.54	0.51	0.51	0.52	0.51	0.51	0.49	0	1.06
FeO	20	19.9	15.71	17.85	18.85	17.67	19.79	9.49	8.14
MnO	0.28	0.24	0.24	0.26	0.24	0.24	0.25	0.14	0.31
MgO	17.36	17.2	15.67	16.51	16.82	19.13	19.9	33.5	20.7
CaO	8.38	8.55	11.09	9.74	9.19	7.33	7.54	0.26	4.74
Na_2O	0.09	0.1	0.13	0.11	0.11	0.08	0.08	0	0
Total	100	100	100.01	100	100	100	100	100.85	101.21
Mg#	0.61	0.64	0.64	0.62	0.65	0.69	0.64	0.86	0.82

Table 2. Experimental conditions, phase assemblages, phase proportions, mineral-liquid K_Ds, and run durations for the experiments used in this study. Phase proportions were determined through a least squares linear regression of mineral compositions and starting composition. Negative proportions indicate that the phase compositions produce a nearly singular matrix which yields inaccurate estimates of the linear regression coefficients. [a] Grt decomposed upon quench. For these experiments, grt analyses from an experiment of the same bulk composition was used. No mineral KD was calculated for the grt in these experiments. [b] The liquid fraction of the experiment was too small to analyze.

Bulk	P	T			Phase Proportions					Fe-Mg KD				Duration
Composition	(GPa)	(°C)	Exp	Phases	Melt	Olv	Cpx	Grt	Opx	Olv	Cpx	Grt	Opx	(hrs)
A15-09-2	2.6	1480	C439	liq,olv,cpx,opx	0.63	0.17	0.19		0.01	0.33	0.33		0.29	24
A15-09-2	2.6	1460	C436	liq,olv,cpx,grt,opx	0.43	0.15	0.38	0.01	0.03	0.35	0.33	0.47	0.29	27.5
A15-09-2	2.6	1450	C444	liq,olv,cpx,grt[a]	0.5	0.14	0.34	0.01		0.37	0.37	~		50
A15-09-2	2.6	1440	C438	liq,olv,cpx,grt[a]	0.47	0.16	0.35	0.03		0.45	0.42	~		26
A15-09-1	2.4	1460	C433	liq,olv,cpx	0.69	0.15	0.18			0.34	0.35			23.5
A15-09-1	2.35	1440	C435	liq,olv,cpx,grt,opx	0.55	0.05	0.07	<0.01	0.33	0.41	0.42	0.54	0.37	25
A15-09-1	2.35	1420	C434	liq,olv,cpx,grt[a],opx	0.45	0.06	0.21	0.05	0.24	0.36	0.37	~	0.32	22
A15-75/25	2.3	1480	C427	liq,olv,opx	0.95	0.07			-0.01	0.36			0.33	24.5
A15-75/25	2.3	1460	C428	liq,olv,cpx	0.73	0.11	0.17			0.33	0.32			24.5
A15-75/25	2.3	1440	C432	liq,olv,cpx,grt[a]	0.5	0.06	0.4	0.03		0.33	0.33	~		23
A15-75/25	2.3	1420	C429	liq,olv,cpx,grt	0.41	0.09	0.42	0.08		0.38	0.37	0.53		26
A15-50/50	2.8	1500	C418	liq,olv,cpx,grt[a]	0.59	0.05	0.3	0.06		0.33	0.34	~		26
A15-50/50	2.6	1520	C419	liq,olv	0.94	0.07				0.34				19
A15-50/50	2.6	1510	C426	liq,olv,cpx	0.96	0.1	-0.05			0.38	0.38			29
A15-50/50	2.6	1500	C417	liq,olv,cpx,grt[a]	0.67	0.06	0.25	0.03		0.33	0.32	~		20
A15-50/50	2.6	1480	C422	liq,olv,cpx,grt[a]	0.7	0.07	0.2	0.03		0.34	0.35	~		24
A15-50/50	2.6	1460	C423	liq,olv,cpx,grt	0.5	0.07	0.31	0.13		0.42	0.39	0.61		30
A15-07-26	2.8	1460	C416	liq,olv,cpx,grt	0.31	0.04	0.38	0.27		0.32	0.28	0.44		46.5
A15-07-26	2.6	1560	C406	liq	1									21
A15-07-26	2.6	1450	C414	liq,olv,cpx	0.65	0.03	0.32			0.32	0.32			50
A15-07-26	2.6	1430	C412	liq,olv,cpx,grt	0.28	0.04	0.38	0.3		0.37	0.32	0.49		18

Table 2. cont.

Bulk Composition	P (GPa)	T (°C)	Exp	Phases	Phase Proportions					Fe-Mg KD				Duration (hrs)
					Melt	Olv	Cpx	Grt	Opx	Olv	Cpx	Grt	Opx	
A15-07	2.5	1550	C375	liq,opx	1				-0.01				0.35	5
A15-07	2.5	1520	C377	liq,olv,opx	0.96	0.08			-0.04	0.38			0.34	16
A15-07	2.5	1480	C379	liq,cpx,opx	0.84		-0.32		0.47		0.35		0.35	20
A15-07	2.35	1500	C383	liq,opx	0.89				0.11				0.36	11
A15-07	2.2	1540	C378	liq	0.99									17
A15-07	2.2	1520	C372	liq,opx	0.88				0.12				0.3	7
A15-07	2	1500	C384	liq,olv,opx	0.98	0.09			-0.08	0.35			0.33	13
A15-07	2	1480	C387	liq,olv,opx	0.9	0.06			0.04	0.34			0.32	10
A15-07	1.7	1500	C390	liq	1									23
A15-07	1.7	1480	C392	liq,olv	0.98	0.02				0.35				11.5
A15-57	2.5	1540	C358	liq,opx	0.86				0.14				0.3	8
A15-57	2.5	1520	C360	liq,olv,opx	0.78	0			0.21	0.33			0.29	20
A15-57	2.3	1520	C357	liq,opx	0.89				0.1				0.31	8
A15-57	2.3	1500	C362	liq,olv,cpx,opx	0.86	0.07	-0.07		0.14	0.39	0.37		0.33	22
A15-57	2.3	1420	C431	liq[b],olv,cpx										19.5
A15-57	2.1	1500	C359	liq,olv,opx	0.86	0.06			0.08	0.35			0.31	32
A15-57	2	1530	C385	liq	0.99									29
A15-57	1.8	1515	C393	liq,olv	0.96	0.04				0.34				9
A15-57	1.8	1500	C391	liq,olv	0.98	0.02				0.34				20

Table 3. Experimental phase compositions as analyzed by electron microprobe. All Fe analyzed as FeO, n = number of analyses, 1σ = one standard deviation of the mean for all analyses (given on the line below each elemental analysis and the Total). n/a = not analyzed.

Experiment	Phase	n	SiO2	TiO2	Al2O3	Cr2O3	FeO*	MnO	MgO	CaO	Na2O	Total
C357	melt	11	45.8	0.06	8.36	0.07	20.8	0.04	16.1	9.45	0.14	100.86
	1σ		2.1	0.03	1.76	0.02	3.5	0.02	0.9	1.09	0.05	0.54
	opx	8	55.1	0.03	2.36	0.72	11.5	0.21	28.4	1.93	0.11	100.33
			0.5	0.01	0.2	0.05	0.2	0.03	0.3	0.06	0.08	0.28
C358	melt	10	45.2	0.44	8.23	0.49	21.1	0.31	15.4	9.49	0.05	100.62
			0.8	0.06	1	0.04	1.9	0.04	0.7	0.72	0.12	0.84
	opx	9	54.7	0.04	2.64	0.73	11.8	0.19	28.3	2.03	0.03	100.43
			0.4	0.01	0.19	0.04	0.2	0.02	0.3	0.1	0.09	0.53
C359	melt	13	45.5	0.42	8.36	0.52	20.7	0.29	14.9	9.74	0.2	100.57
			0.9	0.06	0.47	0.05	1.5	0.03	0.8	0.34	0.13	0.41
	olv	7	38.5	0.02	0.1	0.3	20.1	0.24	40.8	0.33	n/a	100.36
			0.2	0.01	0.01	0.01	0.3	0.04	0.3	0.01	n/a	0.67
	opx	11	54.8	0.03	2.3	0.76	12.2	0.19	28.3	2.06	0.03	100.71
			0.3	0.01	0.23	0.06	0.1	0.01	0.2	0.04	0.05	0.36
C360	melt	6	43.3	0.47	8.18	0.48	22.1	0.35	14.4	9.63	0.31	99.2
			0.6	0.06	0.25	0.03	1.3	0.04	0.4	0.27	0.08	0.54
	olv	5	38.6	0.03	0.18	0.28	20.2	0.21	39.4	0.44	n/a	99.36
			0.1	0.02	0.13	0.02	0.3	0.03	0.3	0.19	n/a	0.51
	opx	5	53.8	0.03	2.97	0.76	12.2	0.21	27.3	2.4	0.01	99.66
			0.3	0.02	0.32	0.07	0.2	0.01	0.1	0.12	0.01	0.4
C362	melt	12	46	0.07	8.5	0.09	20.5	0.02	14.9	9.99	0.22	100.31
			2	0.03	0.72	0.02	4.2	0.01	1	0.68	0.08	0.6
	olv	11	38.1	0.01	0.11	0.29	21.2	0.22	39.6	0.38	n/a	99.98
			0.3	0.01	0.04	0.02	0.5	0.04	0.7	0.07	n/a	0.8
	opx	14	53.8	0.06	3.04	0.8	12.5	0.22	27.4	2.42	0.01	100.26
			0.5	0.01	0.25	0.06	0.3	0.03	0.3	0.21	0.02	0.56
	cpx	11	53.6	0.05	2.84	0.77	12.6	0.25	24.7	5.41	0.02	100.23
			0.4	0.01	0.13	0.03	0.2	0.02	0.2	0.26	0.03	0.58

Table 3. cont.

Experiment	Phase	n	SiO2	TiO2	Al2O3	Cr2O3	FeO*	MnO	MgO	CaO	Na2O	Total
C372	melt	5	44.1	0.37	8.59	0.43	20.9	0.23	15.6	9.64	0.16	100.01
			0.7	0.03	0.7	0.03	1.3	0.02	0.8	0.22	0.06	0.54
	opx	7	54.7	0.04	2.66	0.8	11.6	0.18	28.9	1.76	0.06	100.71
			0.3	0.01	0.23	0.06	0.2	0.02	0.5	0.06	0.07	0.58
C375	melt	9	47.2	0.01	8.21	0.03	19.1	0.02	17	9.22	0.14	100.93
			1.3	0.01	0.3	0.02	2	0.01	0.8	0.4	0.07	0.49
	opx	6	55.2	0.03	2.66	0.65	11	0.13	28.2	1.87	0	99.7
			0.2	0.01	0.29	0.05	0.2	0.01	0.2	0.04	0.01	0.27
C377	melt	10	46.4	0.02	8.87	0.04	18.6	0.02	16.3	10.4	0.34	101.01
			2.7	0.02	0.82	0.02	4	0.01	1.8	1.1	0.22	0.36
	olv	7	38.5	0	0.11	0.24	18.5	0.21	42.7	0.32	n/a	100.52
			0.4	0	0.01	0.02	0.2	0.03	0.8	0.02	n/a	0.67
	opx	4	54.3	0.04	3.17	0.78	11.1	0.13	28.2	2.11	0	99.9
			0.4	0.01	0.2	0.05	0	0.01	0.2	0.07	0.01	0.36
C378	melt	5	46.3	0.34	7.77	0.5	19.4	0.18	17.3	8.12	0.3	100.18
			1.1	0.02	0.35	0.03	1.7	0.01	0.4	0.25	0.09	0.17
C379	melt	11	44.6	0.02	8.94	0.03	20.5	0.02	14	11.2	0.58	99.85
			2.4	0.03	0.58	0.02	4.6	0.02	0.9	1.7	0.16	0.84
	opx	5	53.9	0.05	3.78	0.87	13.3	0.2	26.2	2.62	0.08	101.05
			0.2	0.01	0.23	0.07	0.2	0.04	0.3	0.24	0.11	0.22
	cpx	5	53.2	0.06	3.89	0.93	11.7	0.19	23	7.65	0.11	100.79
			0.2	0.01	0.08	0.02	0.1	0.02	0.2	0.15	0.04	0.23
C383	melt	14	44.9	0.37	8.82	0.45	19.4	0.23	15.1	9.69	0.08	99.01
			1.7	0.04	0.46	0.05	2.3	0.03	0.8	0.49	0.1	0.46
	opx	5	53.9	0.04	3.36	0.87	12.4	0.17	27.1	2.05	0	99.87
			0.7	0.02	0.24	0.05	0.2	0.03	0.1	0.06	0	0.5

Table 3. cont.

Experiment	Phase	n	SiO2	TiO2	Al2O3	Cr2O3	FeO*	MnO	MgO	CaO	Na2O	Total
C384	melt	14	46.7	0.04	8.14	0.07	19.1	0.02	15.9	9.32	0.3	99.61
			2.1	0.03	0.47	0.02	2.9	0.01	1.9	0.62	0.16	1.41
	olv	5	38.5	0.03	0.08	0.26	17.8	0.15	42.4	0.29	n/a	99.51
			0.3	0.02	0.02	0.02	0.3	0.01	0.4	0.02	n/a	0.29
	opx	5	55.1	0.05	2.29	0.8	11.6	0.13	29.1	1.64	0.01	100.63
			0.7	0.04	0.33	0.04	0.5	0.01	0.9	0.08	0.02	0.62
C385	melt	8	45.8	0.38	7.04	0.47	19.8	0.27	17.1	8.1	0.02	98.86
			0.6	0.08	0.34	0.03	0.6	0.03	0.9	0.51	0.04	0.36
C387	melt	13	45.6	0.07	8.72	0.08	20.1	0.02	15.5	9.78	0.28	100.16
			1.6	0.03	0.45	0.01	2.2	0.01	1.2	0.78	0.19	0.9
	olv	9	38.6	0.01	0.09	0.25	18.7	0.18	41.7	0.27	n/a	99.9
			0.5	0.01	0.03	0.01	0.3	0.02	0.6	0.01	n/a	0.32
	opx	5	54.4	0.03	2.79	0.89	11.9	0.2	28.3	1.8	0.01	100.32
			0.3	0.01	0.26	0.11	0.2	0.02	0.6	0.08	0.02	0.65
C390	melt	14	45.2	0.31	7.63	0.52	19.3	0.21	17.3	8.4	0.71	99.59
			0.2	0.06	0.06	0.04	0.5	0.03	0.2	0.14	0.15	0.51
C391	melt	14	46.2	0.4	7.37	0.55	20.5	0.26	17	8.53	0.16	100.98
			0.6	0.05	0.31	0.06	0.7	0.03	0.9	0.45	0.07	0.82
	olv	8	38.9	0.01	0.08	0.3	17.8	0.19	43.3	0.29	n/a	100.92
			0.8	0.01	0.01	0.01	0.2	0.02	0.6	0.01	n/a	0.29
C392	melt	13	45.5	0.32	7.76	0.52	19.2	0.23	16.5	8.72	0.68	99.49
			0.9	0.05	0.21	0.03	0.3	0.03	0.3	0.12	0.33	0.82
	olv	6	38.8	0.01	0.08	0.27	17.5	0.17	42.8	0.26	n/a	99.87
			0.5	0.01	0.03	0.01	0.5	0.02	0.3	0.01	n/a	0.77
C393	melt	16	46.8	0.4	7.52	0.51	19.9	0.28	16.6	8.68	0.36	101.03
			0.6	0.06	0.19	0.06	1	0.03	0.3	0.22	0.14	0.48
	olv	6	38.6	0.01	0.08	0.31	17.4	0.21	42.7	0.3	n/a	99.53
			0.3	0.01	0.03	0.02	0.5	0.03	0.3	0.02	n/a	0.5

Table 3. cont.

Experiment	Phase	n	SiO2	TiO2	Al2O3	Cr2O3	FeO*	MnO	MgO	CaO	Na2O	Total
C406	melt	13	43.7	0.37	11.89	0.51	14.9	0.2	15.7	11.6	1.01	99.88
			0.3	0.04	0.07	0.03	0.3	0.02	0.2	0.4	0.1	0.82
C412	melt	6	41	0.93	10.64	0.14	22.7	0.24	11.6	11.1	1.19	99.48
			1	0.28	1.12	0.04	2.1	0.03	1.6	1.4	0.64	0.53
	olv	5	37.5	0.03	0.14	0.08	25.7	0.2	35	0.49	n/a	99.16
			0.3	0.02	0.04	0.02	0.6	0.03	0.9	0.05	n/a	0.49
	cpx	7	51	0.15	6.23	0.4	10.4	0.1	16.8	15.1	0.41	100.66
			0.2	0.05	0.17	0.06	0.2	0.07	0.3	0.2	0.14	0.45
	grt	7	39.9	0.22	22.07	0.98	14.5	0.28	15.2	6.84	0.01	99.97
			0.4	0.07	0.33	0.15	0.3	0.04	0.4	0.42	0.02	0.33
C414	melt	14	44.2	0.47	10.37	0.44	17.9	0.24	15.2	10.7	0.45	99.93
			0.4	0.06	0.09	0.03	0.6	0.03	0.5	0.3	0.05	0.54
	olv	7	38.5	0.02	0.25	0.16	21	0.22	39.8	0.49	n/a	100.39
			0.3	0.01	0.08	0.02	0.5	0.02	0.3	0.2	n/a	0.61
	cpx	3	51.7	0.1	6.6	0.51	9.52	0.19	18.1	14	0.46	101.19
			0.1	0	0.13	0.07	0.11	0.01	0.6	0.2	0.08	0.39
C416	melt	11	40.4	0.72	10.44	0.15	23.3	0.28	11.3	10.5	1.77	98.93
			0.2	0.06	0.08	0.02	0.3	0.02	0.1	0.1	0.09	0.3
	olv	10	37.9	0.04	0.3	0.1	24.2	0.23	37	0.59	n/a	100.31
			0.1	0.01	0.26	0.01	0.7	0.03	0.4	0.17	n/a	0.72
	cpx	6	50.9	0.13	7.29	0.52	9.51	0.16	16.7	15.3	0.63	101.11
			0.2	0.01	0.33	0.04	0.41	0.01	0.3	0.4	0.18	0.45
	grt	5	40.2	0.22	22.22	0.96	14	0.33	15.5	6.91	0.02	100.3
			0.2	0.03	0.33	0.3	0.7	0.05	0.2	0.27	0.04	0.54

Table 3. cont.

Experiment	Phase	n	SiO2	TiO2	Al2O3	Cr2O3	FeO*	MnO	MgO	CaO	Na2O	Total
C417	melt	9	43.2	0.44	11.25	0.3	20.5	0.29	13.1	10.5	1.01	100.63
			0.2	0.05	0.07	0.05	0.2	0.03	0.2	0.1	0.13	0.43
	olv	5	38.2	0.02	0.19	0.21	20.5	0.17	40.3	0.46	n/a	100.02
			0.2	0.01	0.05	0.01	0.1	0.01	0.3	0.08	n/a	0.23
	cpx	6	51.7	0.08	6.29	0.92	10.2	0.2	20.1	11.1	0.31	100.92
			0.3	0.01	0.33	0.05	0.2	0.02	0.4	0.4	0.16	0.35
C418	melt	11	43	0.56	11.02	0.34	21.4	0.27	12.8	10.3	0.84	100.54
			0.2	0.06	0.09	0.03	0.2	0.03	0.2	0.1	0.11	0.45
	olv	10	38	0.01	0.21	0.27	21.5	0.22	39	0.47	n/a	99.67
			0.1	0.01	0.01	0.02	0.4	0.03	0.2	0.03	n/a	0.46
	cpx	7	51.7	0.11	6.09	0.58	11.3	0.22	20.2	10.4	0.26	100.79
			0.3	0.02	0.21	0.03	0.2	0.02	0.5	0.3	0.13	0.74
C419	melt	8	44.2	0.04	10.3	0.07	18.3	0.03	14.9	11.2	0.54	99.61
			0.3	0.01	0.08	0.02	0.3	0.02	0.1	0.1	0.07	0.46
	olv	11	38.8	0	0.23	0.24	17.5	0.19	42	0.39	n/a	99.3
			0.3	0	0.24	0.02	0.2	0.03	0.5	0.02	n/a	0.51
C422	melt	10	44	0.54	10.94	0.33	19.8	0.3	13.2	10.5	0.72	100.26
			0.1	0.06	0.05	0.04	0.4	0.04	0.1	0.2	0.08	0.55
	olv	6	38.6	0.02	0.15	0.19	20.6	0.21	40.1	0.39	n/a	100.29
			0.2	0.01	0.01	0.02	0.2	0.02	0.3	0.02	n/a	0.3
	cpx	11	51.9	0.07	5.85	0.77	10.8	0.19	20.7	10.3	0.23	100.81
			0.3	0.02	0.19	0.05	0.5	0.03	0.5	0.6	0.16	0.5

Table 3. cont.

Experiment	Phase	n	SiO2	TiO2	Al2O3	Cr2O3	FeO*	MnO	MgO	CaO	Na2O	Total
C423	melt	11	42.5	0.67	10.07	0.18	21	0.28	12.8	10.7	0.98	99.22
			1.9	0.1	0.42	0.05	2.4	0.03	1.1	0.5	0.39	0.43
	olv	10	37.8	0.02	0.17	0.14	25.1	0.23	36.2	0.44	n/a	100.1
			0.3	0.01	0.03	0.01	0.3	0.04	0.2	0.02	n/a	0.39
	cpx	10	51.3	0.09	5.86	0.58	11.9	0.22	18.5	12	0.21	100.61
			0.3	0.02	0.33	0.06	0.4	0.04	0.5	0.7	0.2	0.44
	grt	6	40.8	0.2	22.42	1.31	14.7	0.31	14.8	6.35	0.02	100.9
			0.2	0.04	0.22	0.14	0.4	0.03	0.4	0.3	0.01	0.48
C426	melt	6	45.6	0.33	10.68	0.44	17.1	0.25	14.2	10.8	1.11	100.44
			1.3	0.03	0.69	0.05	2.3	0.03	0.9	0.6	0.54	0.68
	olv	4	39	0.01	0.2	0.28	18.8	0.21	40.9	0.47	n/a	99.9
			0.3	0	0.02	0.01	0.2	0.01	0.5	0.04	n/a	0.41
	cpx	6	52	0.08	5.94	1.06	9.35	0.21	20.6	11.2	0.42	100.88
			0.5	0.02	0.15	0.05	0.56	0.02	1	1.3	0.1	0.55
C427	melt	14	44.6	0.4	9.79	0.5	17.7	0.22	15.1	10.5	0.84	99.6
			0.5	0.05	1.13	0.05	1.7	0.03	0.3	0.7	0.15	0.51
	olv	8	38.8	0	0.13	0.28	18	0.2	42.4	0.35	n/a	100.23
			0.1	0	0.01	0.01	0.1	0.02	0.5	0.01	n/a	0.35
	opx	6	54.7	0.03	3.35	0.88	11.1	0.17	28.7	2.29	0.03	101.25
			0.4	0.02	0.46	0.1	0.2	0.02	0.2	0.15	0.03	0.37
C428	melt	11	43.5	0.5	10.59	0.35	20.1	0.23	12.4	10.1	1.76	99.62
			0.2	0.05	0.09	0.04	0.2	0.03	0.1	0.2	0.13	0.48
	olv	6	38.1	0	0.15	0.2	21.3	0.22	39.8	0.37	n/a	100.24
			0.3	0	0.02	0.01	0.2	0.03	0.4	0.01	n/a	0.4
	cpx	6	52	0.06	5.48	1.19	10.3	0.17	20.2	10.5	0.51	100.39
			0.5	0.01	0.17	0.1	0.4	0.03	0.4	0.5	0.06	0.51

Table 3. cont.

Experiment	Phase	n	SiO2	TiO2	Al2O3	Cr2O3	FeO*	MnO	MgO	CaO	Na2O	Total
C429	melt	11	42.8	0.77	10.8	0.2	23.1	0.26	11.4	10.3	0.69	100.22
			2.3	0.15	0.49	0.05	3.2	0.03	1.2	0.5	0.46	0.59
	olv	6	37	0.02	0.18	0.15	27	0.21	35	0.41	n/a	99.97
			0.1	0.01	0.02	0.01	0.1	0.02	0.4	0.03	n/a	0.38
	cpx	6	51.1	0.13	6.11	0.65	14	0.23	18.5	10	0.22	100.95
			0.5	0.04	0.41	0.04	0.5	0.04	0.4	0.2	0.07	0.38
	grt	5	40.9	0.21	22.51	1.31	15.3	0.31	14.3	5.76	0.01	100.63
			0.4	0.03	0.09	0.06	0.3	0.01	0.1	0.07	0.01	0.48
C431	melt	n/a	-	-	-	-	-	-	-	-	-	-
	olv	7	37.1	0.03	0.12	0.17	25.6	0.23	36.5	0.41	n/a	100.17
			0.1	0.01	0.02	0.01	0.2	0.03	0.2	0.03	n/a	0.36
	cpx	10	51	0.08	5.11	0.83	14.2	0.23	20.2	8.23	0.14	100.01
			0.4	0.02	0.42	0.02	0.4	0.03	0.5	0.45	0.1	0.82
C432	melt	10	41.4	0.7	10.88	0.22	22.9	0.23	11.4	9.98	1.19	98.87
			0.3	0.06	0.1	0.03	0.3	0.03	0.1	0.19	0.11	0.32
	olv	10	37.6	0	0.22	0.15	24.4	0.24	36.8	0.43	n/a	99.84
			0.2	0	0.11	0.02	0.4	0.03	0.5	0.1	n/a	0.6
	cpx	8	51.4	0.09	6.14	0.73	13.2	0.19	20.1	8.61	0.21	100.74
			0.4	0.01	0.2	0.06	0.3	0.01	0.3	0.34	0.08	0.6
C433	melt	15	44.9	0.45	10.83	0.38	18.5	0.24	13.1	9.19	2	99.56
			0.2	0.06	0.06	0.04	0.3	0.02	0.3	0.1	0.09	0.5
	olv	6	38.6	0.03	0.16	0.25	19.6	0.18	40.7	0.34	n/a	99.89
			0.3	0.01	0.02	0.02	0.2	0.02	0.6	0.01	n/a	0.66
	cpx	6	52.9	0.05	4.71	0.86	11.2	0.23	22.9	7.54	0.27	100.67
			0.2	0.02	0.33	0.06	0.2	0.03	0.5	0.45	0.06	0.27

Table 3. cont.

Experiment	Phase	n	SiO2	TiO2	Al2O3	Cr2O3	FeO*	MnO	MgO	CaO	Na2O	Total
C434	melt	16	42.2	0.6	10.86	0.19	21.4	0.26	12.6	10.2	0.91	99.17
			0.4	0.06	0.13	0.02	0.4	0.02	0.3	0.2	0.09	0.65
	olv	6	38.1	0	0.12	0.12	23.4	0.21	37.9	0.34	n/a	100.23
			0.2	0.01	0.02	0.01	0.3	0.03	0.2	0.02	n/a	0.28
	opx	11	51.7	0.05	5.91	0.67	13.9	0.18	25.6	2.47	0.02	100.59
			0.4	0.02	0.34	0.06	0.3	0.02	0.4	0.1	0.01	0.55
	cpx	5	51.7	0.07	5.7	0.65	12.9	0.2	20.6	9.13	0.15	101.08
			0.2	0.01	0.11	0.07	0.5	0.02	0.3	0.28	0.09	0.36
C435	melt	8	42.8	0.66	11.16	0.19	20	0.25	13.5	10.59	0.29	99.47
			1.1	0.06	0.45	0.03	1.5	0.04	0.8	0.29	0.24	0.89
	olv	6	37.9	0	0.13	0.13	23	0.22	37.9	0.36	n/a	99.7
			0.2	0	0.01	0.02	0.6	0.02	0.2	0.02	n/a	0.63
	opx	6	52.1	0.07	5.88	0.72	14.1	0.16	25.7	2.52	0.03	101.23
			0.5	0.01	0.33	0.06	0.2	0.01	0.2	0.09	0.02	0.02
	cpx	9	51.1	0.09	6.37	0.74	12.5	0.2	20.3	9.25	0.12	100.61
			0.5	0.02	0.33	0.04	0.4	0.02	0.6	0.46	0.03	0.77
	grt	6	41.5	0.11	22.45	1.64	13	0.28	16.2	5.68	0.02	100.95
			0.2	0.04	0.47	0.1	0.5	0.03	0.3	0.28	0.03	0.52
C436	melt	17	41.6	0.72	10.28	0.26	24.2	0.29	12.6	9.66	0.31	99.84
			2.9	0.11	0.74	0.09	5.3	0.05	1.9	1.11	0.22	0.63
	olv	4	38	0.04	0.15	0.16	24.8	0.24	37	0.39	n/a	100.79
			0.1	0.01	0.06	0.02	0.1	0.03	0.2	0.04	n/a	0.24
	opx	5	52.8	0.09	3.93	0.63	14.6	0.19	26	2.54	0.1	100.84
			0.5	0.01	0.32	0.02	0.3	0.03	0.2	0.06	0.08	0.32
	cpx	7	51.8	0.08	4.59	0.7	13.2	0.24	21.1	8.44	0.17	100.36
			0.1	0.01	0.1	0.03	0.4	0.02	0.4	0.23	0.09	0.77
	grt	9	40.5	0.21	21.23	2.38	14.3	0.34	15.9	6.31	0.02	101.08
			0.5	0.04	0.58	0.24	0.3	0.02	0.3	0.38	0.02	0.34

Table 3. cont.

Experiment	Phase	n	SiO2	TiO2	Al2O3	Cr2O3	FeO*	MnO	MgO	CaO	Na2O	Total
C438	melt	10	41.8	0.6	9.02	0.27	23	0.29	14.7	8.3	1.38	99.33
			1.8	0.21	2.28	0.09	3	0.01	6.7	2.05	0.44	1.15
	olv	7	37.3	0	0.15	0.18	25.3	0.23	36.1	0.37	n/a	99.68
			0.2	0.01	0.05	0.02	0.4	0.03	0.4	0.03	n/a	0.81
	cpx	6	52.3	0.1	4.67	0.66	12.8	0.2	19.5	9.94	0.23	100.45
			0.2	0.02	0.13	0.03	0.5	0.03	0.3	0.46	0.13	0.58
C439	melt	8	43.6	0.54	8.78	0.38	21.7	0.29	13.4	9.32	0.68	98.74
			0.4	0.05	0.31	0.03	0.5	0.05	0.6	0.33	0.05	0.18
	olv	6	38.2	0.02	0.11	0.25	21.1	0.18	39	0.34	n/a	99.25
			0.1	0.01	0.01	0.01	0.1	0.02	0.3	0.01	n/a	0.24
	opx	17	53.9	0.05	3.52	0.73	12.7	0.15	26.6	2.51	0.1	100.26
			0.4	0.01	0.16	0.03	0.3	0.02	0.3	0.07	0.08	0.48
	cpx	14	53.1	0.06	3.65	0.78	12	0.21	22.6	7.84	0.16	100.36
			0.5	0.02	0.28	0.04	0.4	0.03	0.4	0.42	0.05	0.52
C444	melt	19	42.7	0.6	9.14	0.43	23.4	0.25	14	8.18	0.99	99.76
			1	0.07	1.02	0.04	1.9	0.03	1.9	1.03	0.14	0.61
	olv	7	37.7	0.01	0.16	0.18	23.5	0.19	37.6	0.37	n/a	99.7
			0.1	0.01	0.08	0.01	0.5	0.02	0.2	0.06	n/a	0.59
	cpx	5	52.1	0.08	4.69	0.75	12.9	0.24	20.9	8.75	0.04	100.46
			0.1	0.02	0.22	0.05	0.5	0.03	0.4	0.48	0.04	0.24

Table 4. Temperature estimates based on coexisting cpx and opx compositions using the QUILF95 computer program (Anderson et al., 1993).

Experiment	Actual Temp (°C)	QUILF Temp (°C)
C362	1500	1366 ± 675
C379	1480	1481 ± 29
C434	1420	1415 ± 92
C435	1440	1431 ± 91
C436	1460	1438 ± 78
C439	1480	1433 ± 40

Table 5. Mass balance calculations to reproduce the compositions of Group A and Group C green glasses of Apollo 15. Chemical compositions of the mineral phases and the grt-lherzolite melts are given in Table 6.

Primordial Melt + Assimilant Calculations

		Mix Percentages			
Pressure (Gpa)	Bulk Composition	Olv	Opx	Cpx	Grt-Lherzolite Melt
3.2	A15-57	11	17	34	38
3.2	A15-10C	4	26	33	37
3.7	A15-57	10	14	30	46
3.7	A15-10C	1	29	24	46

Table 6. Mineral and melt compositions used in the mass balance calculations summarized in Table 5. Mix fraction is the proportion of each composition that is required to produce the estimated composition (Est. Comp). The residual liquid Mg# represents the Mg# of the magma ocean melt with which all of the cumulate mineral phases (Olv, Opx, and Cpx) are in equilibrium. The Grt-Lherzolite Melt composition and temperature are results of the modified garnet lherzolite melting model of Ebert and Grove (2005). Bulk Composition represents the Apollo 15 green glass composition to be modeled in the mass balance (A15-57: Group A and A15-10C: Group C). See text for further discussion.

3.2 GPa	A15-57						
	Olv	Opx	Cpx	Grt-Lherzolite Melt	Bulk Composition	Est. Comp	% Diff
Mix Fraction	0.11	0.17	0.34	0.38			
SiO_2	34.01	50.05	49.68	45.17	45.74	46.3	-1
TiO_2	0.02	0.05	0.1	0.3	0.39	0.16	
Al_2O_3	0.11	3.51	4.44	13.53	7.22	7.26	-1
Cr_2O_3	0.16	0.8	0.63	0	0.54	0.37	
FeO	42.08	26.55	22.59	8.4	20	20.02	0
MnO	0.21	0.18	0.19	0	0.28	0.12	
MgO	23.04	16.35	12.72	20.1	17.36	17.28	0
CaO	0.38	2.43	9.44	12.21	8.38	8.3	1
Na_2O	0	0.08	0.22	0.27	0.09	0.19	
Total	100	100	100	99.99	100	100	
Cations	3.01	3.99	3.99				
Mg#	0.49	0.52	0.50	0.81	0.61	0.61	
	Residual Liquid Mg# 0.26			Temperature 1539 °C			

Table 6. cont.

3.2 GPa	A15-10C						
	Olv	Opx	Cpx	Grt-Lherzolite Melt	Bulk Composition	Est. Comp	% Diff
Mix Fraction	0.04	0.26	0.33	0.37			
SiO_2	35.08	51.08	50.52	45.17	47.64	48.07	-1
TiO_2	0.02	0.05	0.1	0.3	0.3	0.16	
Al_2O_3	0.11	3.58	4.51	13.53	7.51	7.43	1
Cr_2O_3	0.16	0.82	0.64	0	0.54	0.43	
FeO	36.22	22.39	19.12	8.4	16.63	16.69	0
MnO	0.22	0.19	0.19	0	0.24	0.12	
MgO	27.8	19.33	15.1	20.1	18.63	18.56	0
CaO	0.39	2.48	9.6	12.21	8.35	8.35	0
Na_2O	0	0.08	0.22	0.27	0.15	0.19	
Total	100	100	100	99.99	100	100	
Cations	3.01	3.99	3.99				
Mg#	0.58	0.61	0.58	0.81	0.67	0.66	
	Residual Liquid Mg# 0.33			Temperature 1539 °C			

3.7 GPa	A15-57						
	Olv	Opx	Cpx	Grt-Lherzolite Melt	Bulk Composition	Est. Comp	% Diff
Mix Fraction	0.1	0.14	0.3	0.46			
SiO_2	33.51	49.56	49.28	45.49	45.74	46	-1
TiO_2	0.02	0.05	0.1	0.3	0.39	0.18	
Al_2O_3	0.1	3.47	4.4	11.97	7.22	7.32	-1
Cr_2O_3	0.16	0.8	0.62	0	0.54	0.31	
FeO	44.78	28.52	24.23	8.96	20	19.86	1
MnO	0.21	0.18	0.19	0	0.28	0.1	
MgO	20.85	14.94	11.6	21.44	17.36	17.52	-1
CaO	0.37	2.41	9.36	11.57	8.38	8.51	-1
Na_2O	0	0.07	0.22	0.26	0.09	0.19	
Total	100	3.99	3.99	99.99	100	100	
Cations	3.01	3.01	3.01				
Mg#	0.45	0.48	0.46	0.81	0.61	0.61	
	Residual Liquid Mg# 0.23			Temperature 1581 °C			

Table 6. cont.

3.7 GPa	A15-10C						
	Olv	Opx	Cpx	Grt-Lherzolite Melt	Bulk Composition	Est. Comp	% Diff
Mix Fraction	0.01	0.29	0.24	0.46			
SiO_2	34.48	50.51	50.05	45.49	47.64	47.93	-1
TiO_2	0.02	0.05	0.1	0.3	0.3	0.18	
Al_2O_3	0.11	3.54	4.47	11.97	7.51	7.61	-1
Cr_2O_3	0.16	0.81	0.63	0	0.54	0.39	
FeO	39.49	24.69	21.05	8.96	16.63	16.73	-1
MnO	0.21	0.19	0.19	0	0.24	0.1	
MgO	25.14	17.68	13.78	21.44	18.63	18.55	0
CaO	0.38	2.45	9.51	11.57	8.35	8.32	0
Na_2O	0	0.08	0.22	0.26	0.15	0.19	
Total	100	100	100	99.99	100	100	
Cations	3.01	3.99	3.99				
Mg#	0.53	0.56	0.54	0.81	0.67	0.66	
	Residual Liquid Mg# 0.29			Temperature 1581 °C			

Figure Captions

Figure 1. Experimental phase equilibrium diagrams for Apollo 15 group A green glass compositions A15-57 and A15-07 and two analog compositions A15-75/25 and A15-09-2 (see text for further description of the compositions). MSP = liquidus multiple-phase saturation point.

Figure 2. Pseudoternary phase diagram showing compositions of coexisting mineral phases and melt for experiment C435. The compositions are shown in oxygen normalized units projected through the Plag component of Tormey et al. (1987). The melting reaction is for high-pressure phase equilibrium results and is described in more detail in the text.

Figure 3. Mineral-melt equilibrium partition coefficient for Al_2O_3 (wt. units) vs. the Wo content (Ca / [Ca+Mg+Fe]) in experimentally produced clinopyroxenes. The continuous variation in Wo content indicates that the clinopyroxenes are sub-calcic augites and are above the clinopyroxene solvus.

Figure 4. Apollo 15 green glass compositions from Elkins-Tanton et al. (2003) for groups A, B and C. The compositions of group B glasses can be produced by mixes of group A and group C glasses for all major elements in addition to the SiO_2 and MgO shown here.

Figure 5. Ni and Co concentrations for Apollo 15 green glasses from Steele et al. (1992) and Shearer and Papike (1993), shaded and white regions respectively. The INAA trace element study of Steele et al. (1992) produced distinctly higher concentrations for many trace elements as compared to the ion microprobe study of Shearer and Papike (1993). This discrepancy is apparent in high concentration trace elements shown here as well as in low concentration trace elements shown in Figure 5, suggesting a systematic disagreement between the elements.

Figure 6. The influence of a KREEP geochemical reservoir can be observed in the trace element composition of Apollo 15 green glasses. Data of Shearer and Papike (1993) for Apollo 15 green glasses (groups A, B, C, D and E), and KREEP composition of Neal and Kramer (2003). Sm/Yb normalized to the C1-chondrite values of Sun and McDonough (1989).

Figure 7. Schematic drawing illustrating the production of the Apollo 15 green glasses. **A**. Primordial melts mixing with evolved LMO cumulates, whereby the liquidus MSP provides an estimate of the temperature and pressure of bulk assimilation/reequilibration. **B**. Grt-bearing cumulates melt to a high degree, leaving only olv and opx in the residue. The aggregate melts stall in shallow chambers where olv fractionation and minor amounts of assimilation could occur. Both scenarios derive the 15B compositions by mixing melts of 15A and 15C.

Figure 8. Sm and Co concentrations for Apollo 15 green glasses from Steele et al. (1992), shaded regions, and Shearer and Papike (1993), white regions. The two studies produce different ranges of concentrations for both Sm and Co for each of the green glass groups, which are defined based upon major element characteristics (Delano, 1986). The 15B glass compositions are consistent with derivation from a mixture of 15A and 15C, except for the outlying point with a high Sm content.

Figure 1.

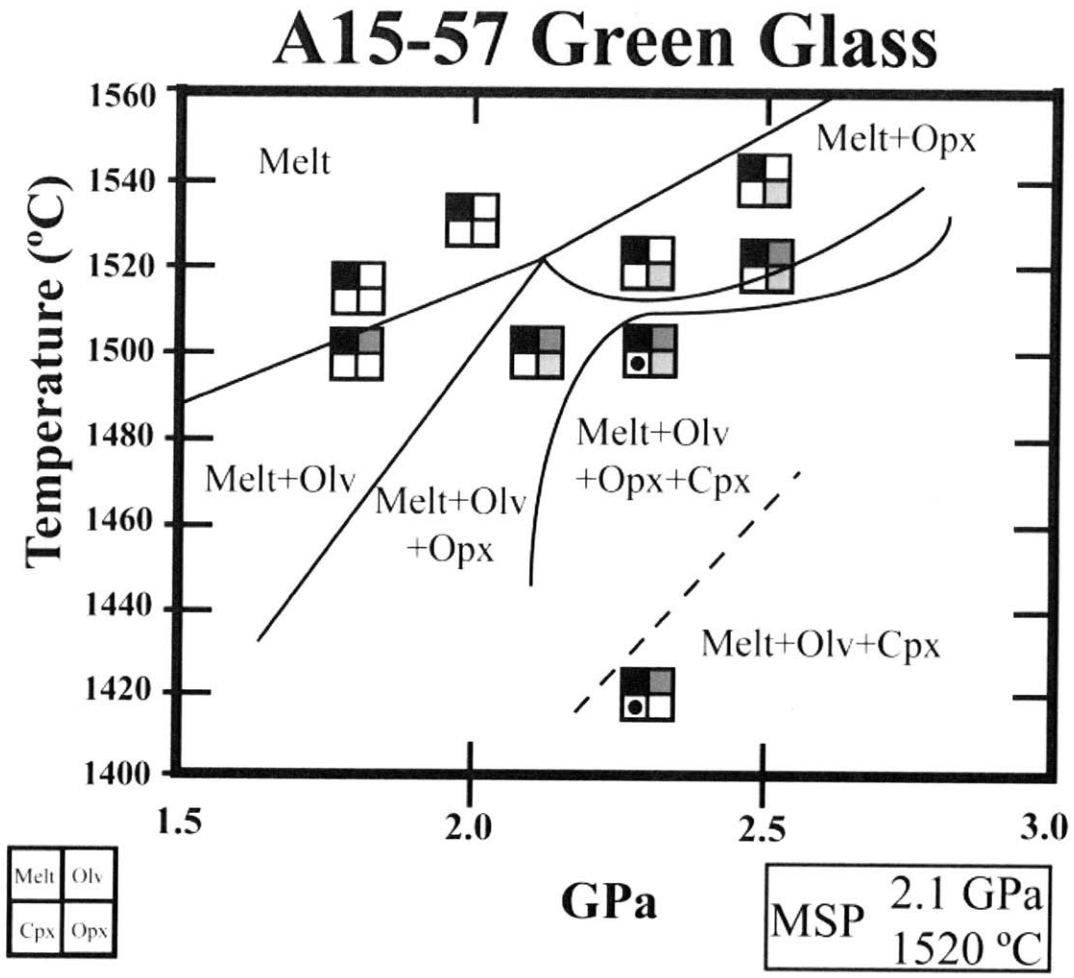
A15-57 Green Glass
Temperature (°C)
1560
1540
1520
1500
1480
1460
1440
1420
1400
1.5
2.0
2.5
3.0
GPa
Melt
Melt+Opx
Melt+Olv
Melt+Olv
+Opx
Melt+Olv
+Opx+Cpx
Melt+Olv+Cpx
Melt
Olv
Cpx
Opx
MSP 2.1 GPa
1520 °C

Figure 1. cont.

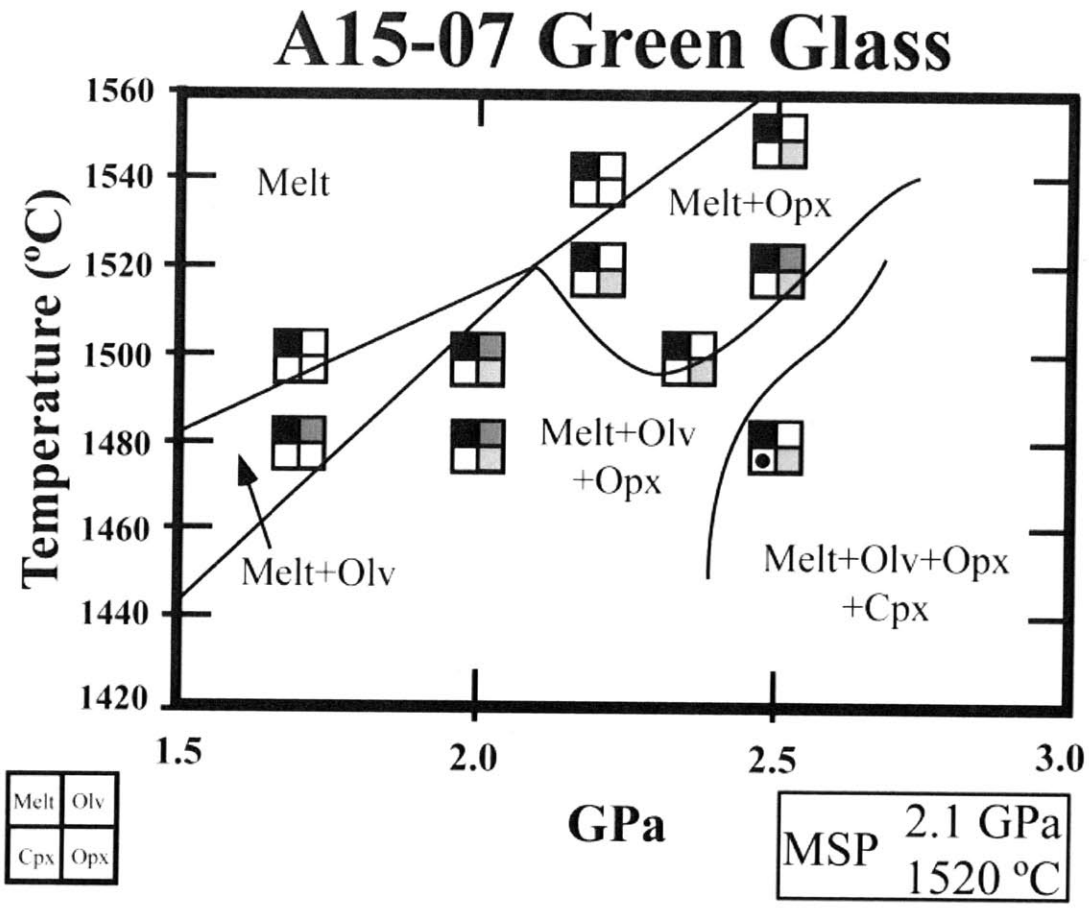

Figure 1. cont.

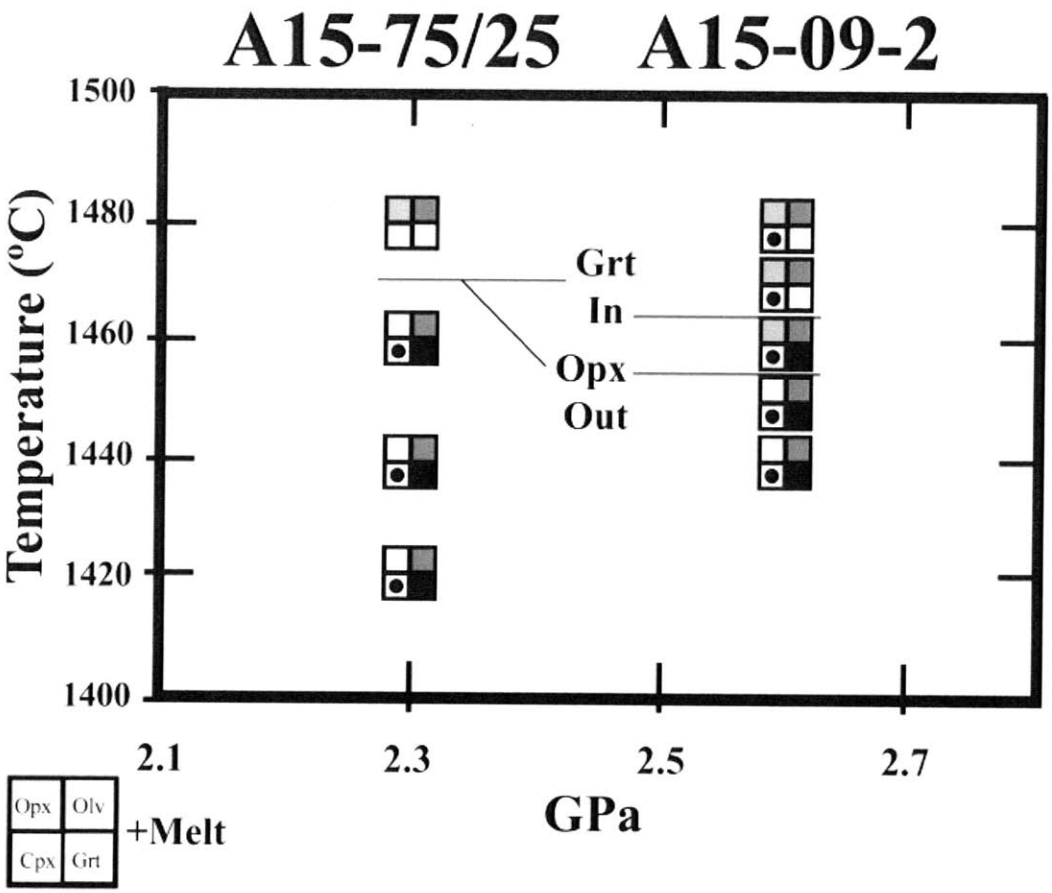

Figure 2.

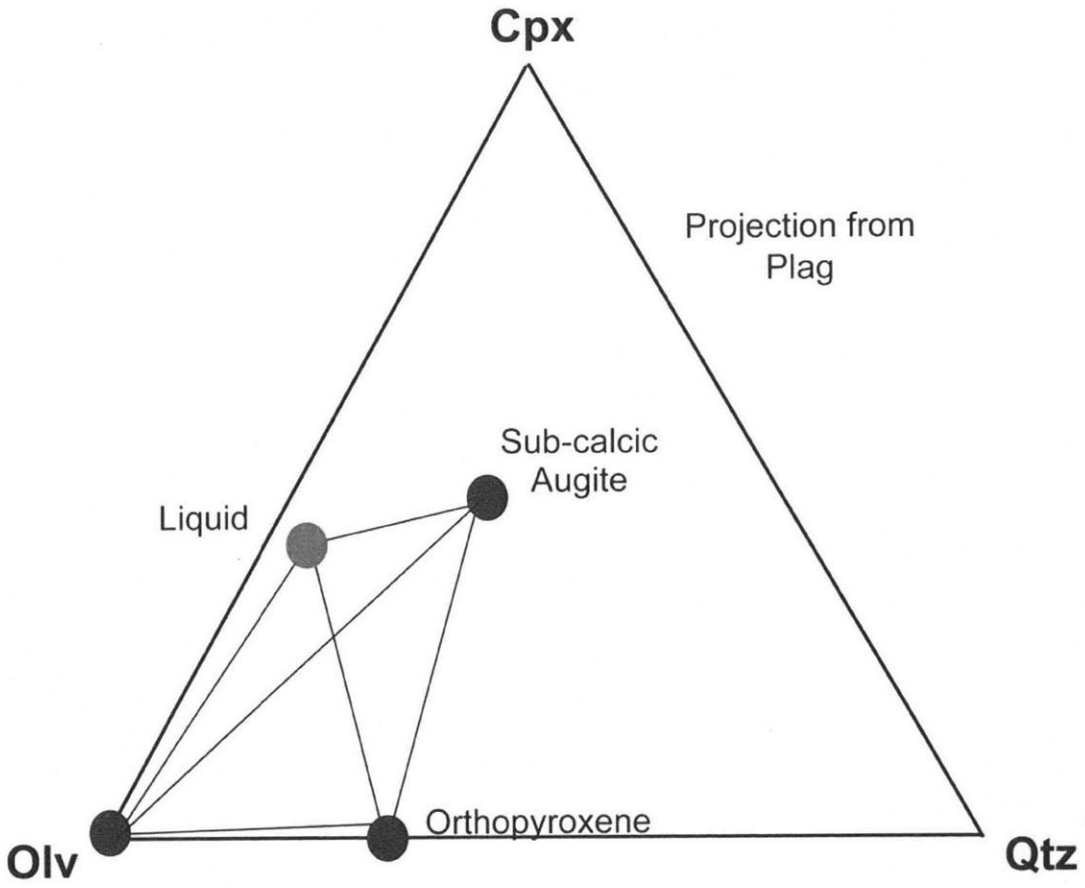

Oliv + Cpx (±Grt) ↔ Opx + Liquid

Figure 3.

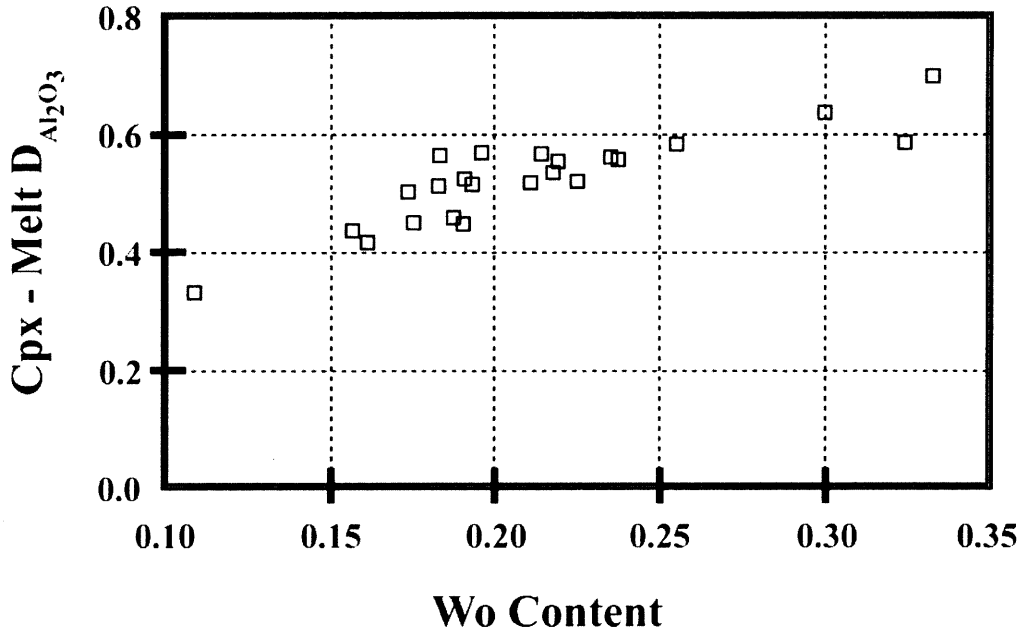
0.8
0.6
0.4
0.2
0.0
Cpx - Melt $D_{Al_2O_3}$
0.10
0.15
0.20
0.25
0.30
0.35
Wo Content

Figure 4.

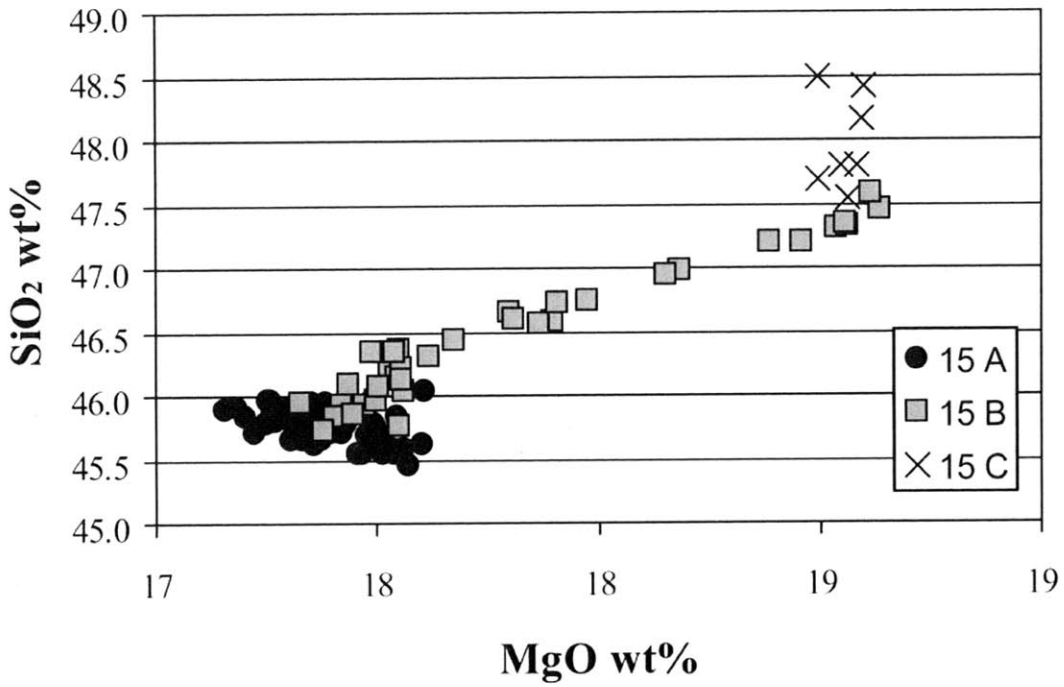
49.0
48.5
48.0
47.5
47.0
46.5
46.0
45.5
45.0
SiO2 wt%
17
18
18
19
19
MgO wt%
15 A
15 B
15 C

Figure 5.

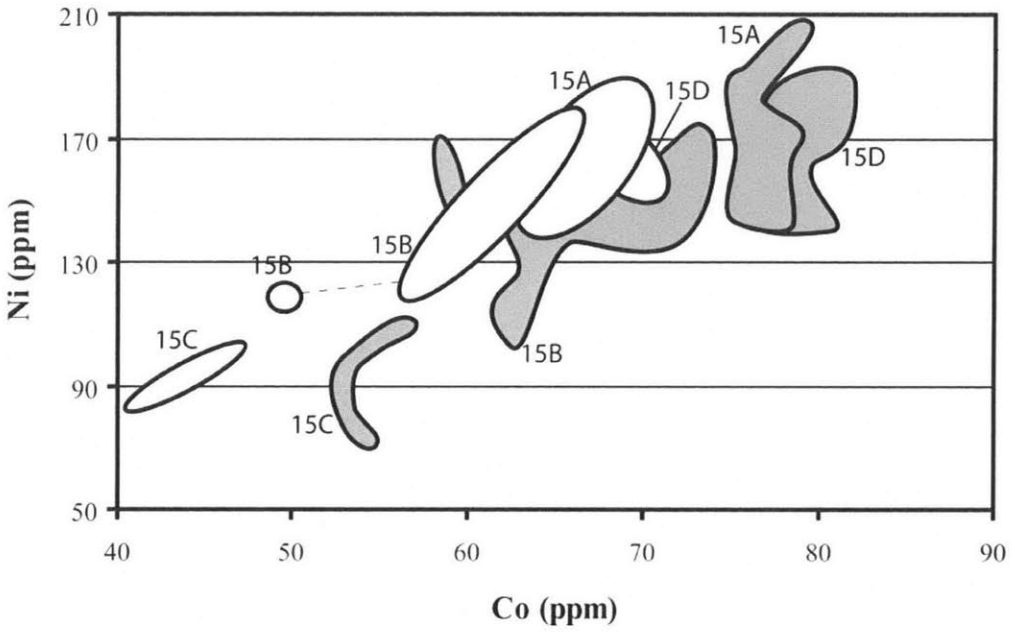
210
170
130
90
50
Ni (ppm)
40
50
60
70
80
90
Co (ppm)
15A
15A
15D
15D
15B
15B
15B
15C
15C

Figure 6.

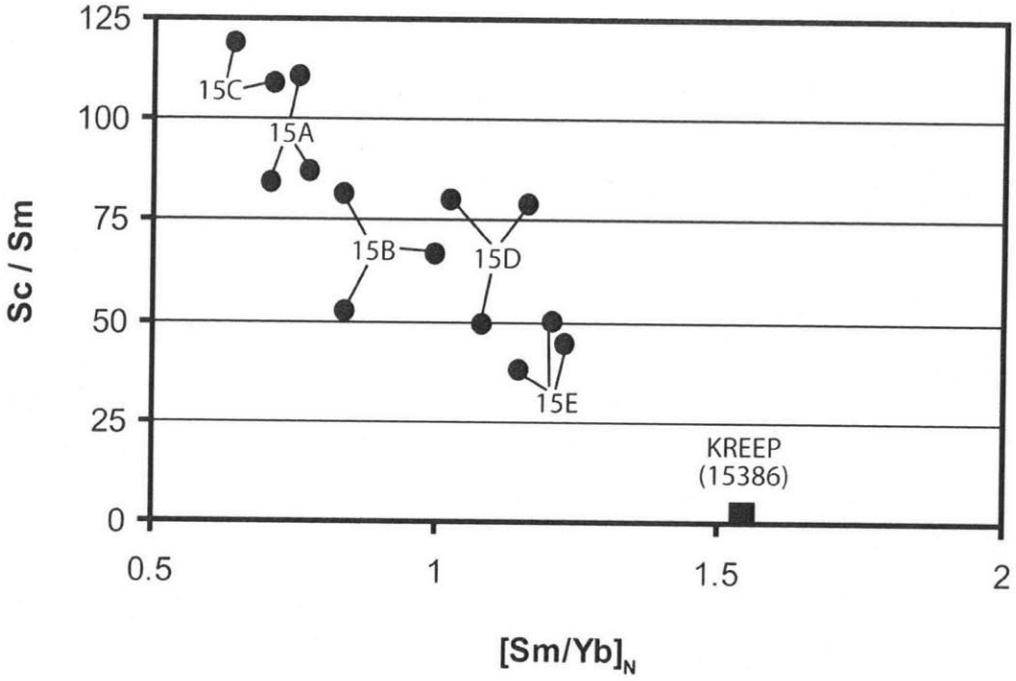
125
100
75
50
25
0
Sc / Sm
0.5
1
1.5
2
[Sm/Yb]N
15C
15A
15B
15D
15E
KREEP
(15386)

Figure 7.

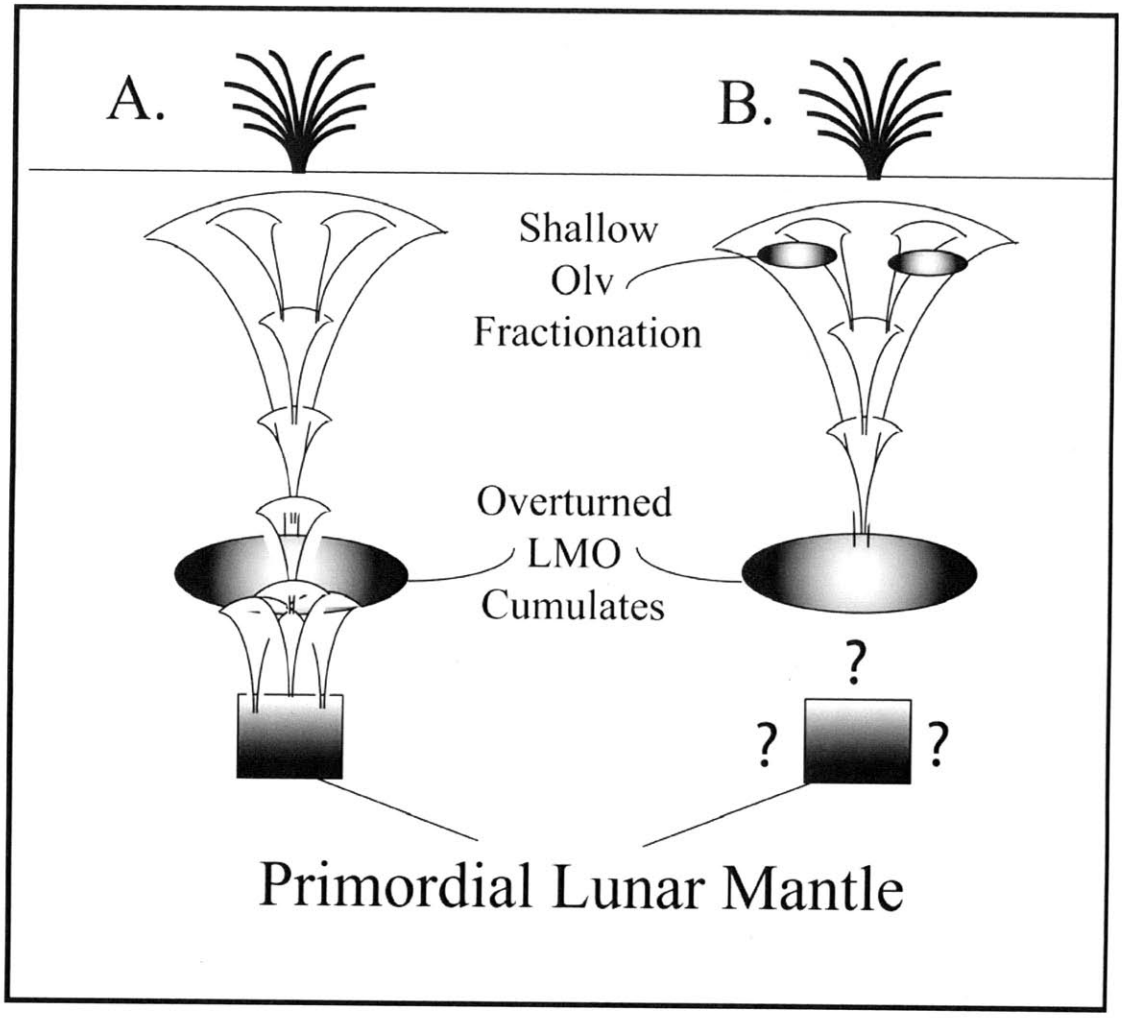
A.
B.
Shallow
Olv
Fractionation
Overturned
LMO
Cumulates
?
?
?
Primordial Lunar Mantle

Figure 8.

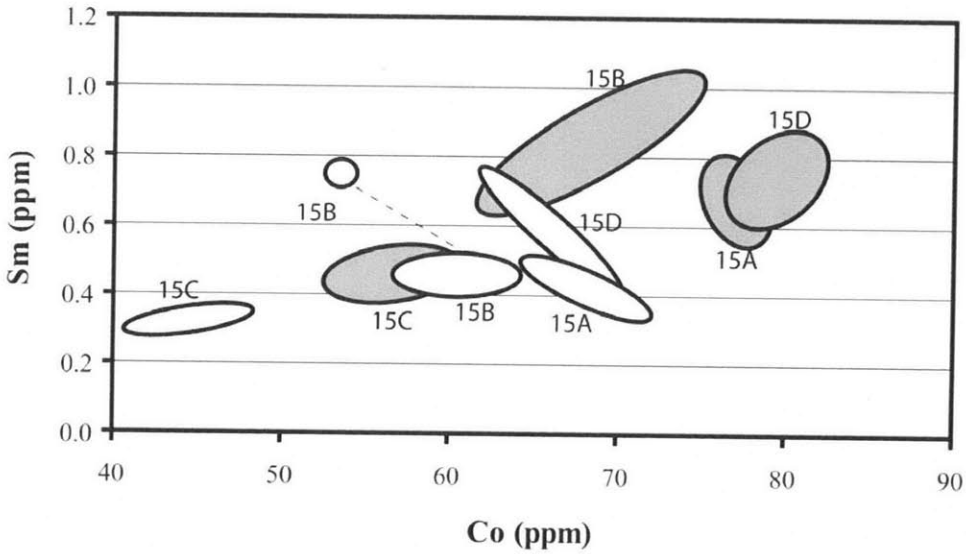
1.2
1.0
0.8
0.6
0.4
0.2
0.0
Sm (ppm)
40
50
60
70
80
90
Co (ppm)
15B
15D
15B
15D
15A
15C
15C
15B
15A

Chapter 3: Primitive Magnesian Andesites from the Mt. Shasta region, California: Products of mantle melting, fractional crystallization and magma mixing

Abstract

Primitive high-SiO_2, (57.4 to 58.9 wt. %), high-MgO (10.1 to 7.66 wt. %) andesite lavas preserve evidence of magma mixing of at least four magmatic components. Compositional variations in the mixed lavas and in the phenocrysts preserve evidence for the identity of these components. Two primitive liquids are present. The primitive magnesian andesite is the dominant component of the erupted magmas. Also present is a primitive basaltic andesite with lower SiO_2 (~ 53 wt. %) and high MgO (~ 10 wt. %). These two primitive magmas mixed with at least two compositionally evolved magmas. One is a product of fractional crystallization of the basaltic andesite and the second is an even more evolved dacite – rhyodacite component. Trace element and isotopic characteristics are consistent with these multi-component magmas as mixtures of melts and there is no evidence for the incorporation of peridotite as one of the mixed components. The primitive end member magnesian andesite (57.4 % SiO_2, 10.1 % MgO) is in equilibrium with the abundant Fo_{94} olivine that is present in the lavas when the effect of variation in oxygen fugacity is taken into account. This primitive magnesian andesite represents a mantle-derived primary magma composition derived from a harzburgite residue by hydrous mantle melting.

Introduction

Andesites are common volcanic rocks in arc settings, however primitive magnesian andesites (PMA) are only found in a small subset of arcs worldwide (e.g. the Aleutians, Kay, 1978, Yogodzinski et al., 1995, the Cascades, Clynne and Borg, 1997, Baker et al., 1994, Anderson, 1974 and Japan, Tatsumi and Ishizaka, 1982, Ishizaka and Carlson, 1983). These primitive arc magmas are important for understanding the processes that lead to the generation of arc lavas, because they preserve much of their primary geochemical characteristics (e.g. Grove et al., 2002, 2003). In the Cascades arc Anderson (1974b) first described this unique type of andesite as one component of a mixed magma taken sampled from a cinder pit in the saddle between Whaleback and Deer Mtns. near Mt. Shasta in northern California (S17 of Anderson, 1973). Until the current study, this was the only sample locality of this PMA eruption that had been investigated. This PMA locality has received attention from numerous researchers investigating the origin of high-MgO, high-SiO_2 magmas (e.g. Grove et al., 2002, 2003, 2005; Anderson, 1974a, 1974b, 1976, 1979; Wood and Turner, 2009). This study reports a comprehensive investigation of the lavas and vents of the Whaleback – Deer Mtn. eruption.

Several investigators have used experimental petrology and geochemical modeling to infer that this PMA magma was produced by hydous melting in the arc mantle wedge (e.g. Grove et al., 2003, Wood and Turner, 2009). However a study by Streck et al. (2007) proposed that PMA magmas are not mantle melts, but are mixtures of disaggregated peridotite and dacite (+/- basalt) and thus do not represent iproduct of mantle melting processes in arc environments. In this paper we discuss the geology, petrology and geochemistry of the Mt. Shasta PMA occurrences in order to understand the nature of compositional variability and identify the composition of the most primitive PMA that is preserved there.

Grove et al. (2005) demonstrated that the andesite and dacite lavas that comprise the bulk of the eruptive products in the Mt. Shasta region are formed through large scale fractional crystallization and magma mixing processes that involved hydrous mantle-derived basaltic andesites and hydrous PMA parental magmas. Evidence for these processes is preserved in the mineral assemblages in the Shasta

stratocone lavas and the proposed mixing processes successfully reproduce the major and trace element characteristics of the Mt. Shasta andesite and dacite lava suite (Grove et al., 2003, 2005). However, if the PMA magma does not actually exist as a mantle derived liquid, then this explanation for the Mt. Shasta lavas is no longer valid. Additionally, if the model of Streck et al. (2007) is correct, then the production of the primitive dacites used in the mixing models must be investigated. Therefore it is important to understand whether or not PMA magmas are mantle melts. Since these sorts of lavas are found in arcs around the world it is important to find the process(es) that lead to their generation.

This study investigates the PMA magmas at Mt. Shasta, including newly identified localities, in order to better understand their formation. Phenocrysts from these samples have long been shown to record localized mixing (e.g. Anderson, 1976), and this study examines the compositional variations in the minerals in order to determine the nature of their original host magmas and evidence for the nature of the magma mixing occurring in the PMA plumbing system. Isotopic compositions of Mt. Shasta lavas are investigated to determine the viability of mixing models that include dacites and crustal ultramafic debris. Isotopic evidence and evidence for the magmatic origin for the primitive olivine and orthopyroxene phenocrysts eliminates the possibility that the PMAs are derived by interacting magmas with a subvolcanic crustal level peridotite is eliminated.

Geologic Setting and Sampling

Mt. Shasta and environs lie near the southern end of the Cascade arc in northern California. Pre-Tertiary rocks of the Klamath Mountains province outcrop to the south and west. Tertiary and Quaternary volcanics of the High Cascades occur to the northeast and east. Tertiary sandstones, shales, and andesitic volcanics, Mesozoic granitic rocks, ultramafic rocks of the Trinity ophiolite, and Mesozoic and Paleozoic metasedimentary rocks are present in the Shasta region and have been inferred to be present beneath the volcano (Griscom, 1980; Blakely et al., 1985; Fuis et al., 1987). The location of the crust-mantle boundary (33-37 km) and the

position of the subducted slab (~125 km) beneath Mt. Shasta have been documented in several seismic investigations (Zucca et al., 1986; Harris et al., 1991; Benz et al., 1992). The Juan de Fuca plate is being subducted at a half spreading rate of 40 mm per year (Wilson, 1988) and the age of the plate beneath Mt. Shasta is inferred to be 12 to 14 million years old (Green and Harry, 1999). As discussed by Grove et al. (2002) the trace of the Blanco Fracture Zone projects beneath the vicinity of Mt. Shasta and serpentine present in the fracture zone may be the source of the high-H_2O contents in Shasta primitive lavas.

The PMA cinder cone, ~8 km north of Mt. Shasta in the saddle between Whaleback and Deer Mtns., first described by Anderson (1973) and termed location S17 (e.g. Anderson, 1973, 1974b, 1976). As described by Anderson (1974b), the location exposes layers composed of cinders and volcanic bombs, with at least two episodes of eruption delineated by the angular unconformity of the two sets of layers. Baker et al. (1994) studied samples from this locality (85-41a, b, c, d) that illustrated the compositional variability present in the cinder cone and obtained major and trace element compositions. Trace element and isotopic composition of one of these samples (85-41b) is reported in Grove et al. (2002) and the highest MgO sample (i.e. most primitive, 85-41c, 9.14 wt. % MgO) was used as an experimental starting composition for experimental studies (e.g. Grove et al., 2003).

Based on unpublished mapping (R.L. Christiansen, personal communication) we sampled lavas that were erupted from one or both vents in the Whaleback – Deer Mountain saddle (Figure 1). A second vent (Vent 2) is 200 m north of the cinder quarry and has erupted lava flows to both the east and west. Sample 88-23, Table 1 is a near-vent sample of this lava. Lavas from Vent 2 and the S17 vent are covered by two younger eruptions. The older of the two is a high alumina olivine tholeiite (HAOT) informally referred to as the Basalt of Pluto Cave (R.L. Christiansen, personal communication). This HAOT lava (see Baker et al., 1994, samples 85-38 and 85-39) erupted from a series of vents ~ 100m north of Vent 2 and defines the surface of the Whaleback – Deer Mtn. saddle flowing up to the edge of the S17 vent locality, thereby obscuring lavas that erupted from Vent 2 and that may have erupted from the S17 vent.

A second younger lava flow covers both the HAOT and the lavas from the PMA eruption(s) near the distal end of the western lava flow. This lava is an andesite informally referred to as the Whaleback andesite (R.L. Christiansen, personal communication). PMA lava flows were erupted from either or both the S17 vent and Vent 2. Lava flows extend to the east and west of these vents. To the east the lava flow extends approximately 2 km. and is partly covered by HAOT. To the west lava flows extend ~6 km to the area of Grass Lake and these could have come from either the S17 vent or vent 2. Samples were collected along the length of these flows from the portions left uncovered by the younger HAOT and andesite flows. Also, the S17 vent, lava from Vent 2 and the western terminus of the lava flow were sampled for paleomagnetic orientation. All three locations share the same magnetic direction and it is therefore possible that the vents and flows were erupted during a single event (D. Champion, personal communication).

Analytical Methods

Field sampling was performed at outcrops of the PMA lavas and at the PMA cinder cone (S17). Samples were chosen to be free of oxidation and weathering, and samples for geochemistry were chipped onsite. The sample chips were boiled for 30 minutes and then put into an ultrasonic bath for 10 minutes. This process that was repeated two times in distilled H_2O. The samples were then dried and hand-picked to eliminate chips with noticeable vesicle filling or hammer marks.

Major element and trace element analyses given in Table 1 were performed on the ThermoARL Advant'XP+ sequential XRF instrument at Washington State University. See Johnson et al. (1999) for discussion of analytical procedure, precision and accuracy. Select trace elements and REEs reported in Table 2 were analyzed by ICP-MS on an HP 4500+ instrument at Washington State University following the procedures of Knack et al. (1994).

Isotopic measurements were performed in the Department of Terrestrial Magnetism (DTM) at the Carnegie Institution of Washington and are reported in Table 3. Sr and Nd isotopic compositions were

measured on the DTM Thermo-Fisher Triton thermal ionization mass spectrometer in static mode. Sr was loaded in HNO_3 onto single outgassed Re filaments and then coated in a mixture of Ta_2O_5, HF and H_3PO_4. The 4 isotopes of Sr and ^{85}Rb were monitored simultaneously in faraday cups with corrections made for ^{87}Rb on ^{87}Sr. Most samples were run at ^{88}Sr signal sizes between 3-5 x 10^{-11} amps, using 8-second integrations to obtain 200 ratios using amplifier rotation between blocks of 20 ratios. The exception was the Trinity peridotite sample TG89-12 where ^{88}Sr was 5 x 10^{-12} amps. Most samples had measured $^{85}Rb/^{86}Sr$ ratios below 0.000007 with only TG89-12 having $^{85}Rb/^{86}Sr$ of 0.000041, resulting in a correction to $^{87}Sr/^{86}Sr$ of 0.000019. Sr data are fractionation corrected to $^{86}Sr/^{88}Sr = 0.1194$. The average value for the NBS 987 Sr standards measured in the same analytical sessions as these samples was $^{87}Sr/^{86}Sr = 0.7102446 \pm 0.0000024$ (2 standard errors (se) on 9 analyses). Uncertainties on sample $^{87}Sr/^{86}Sr$ were typically below 0.000007, except for TG89-12 where the uncertainty was 0.000040.

Nd was loaded in HCl onto one Re filament of a double-filament arrangement and run as the Nd+ ion. All 7 Nd isotopes, ^{140}Ce, and ^{147}Sm were monitored. Most samples were run at ^{144}Nd signal sizes of 2 x 10^{-11} amps for 270 ratios calculated from 8 second integrations using amplifier rotation. The one exception was the Trinity peridotite sample TG89-12 where ^{144}Nd was 2 x 10^{-12} amps. Sm interferences were occasionally significant with one sample (TG07-27) having $^{147}Sm/^{146}Nd = 0.0057$ and one (TG82-94a) with $^{147}Sm/^{144}Nd = 0.0022$. Most samples had $^{147}Sm/^{146}Nd < 0.00003$. For TG07-27 and TG82-94a, the ratio most sensitive to Sm interference, $^{148}Nd/^{144}Nd$, was 0.241589 ± 0.000003 and 0.241582 ± 0.000003, respectively, after Sm correction compared to the average for the standard of 0.2415821 ± 0.0000017 (2se of 9 analyses of the JNdi Nd standard) indicating that the Sm correction is accurate at these levels of Sm interference. Nd is fractionation corrected to $^{146}Nd/^{144}Nd = 0.7219$ and reported relative to an average value of 0.512115 for the JNdi standard, which corresponds to 0.511860 for the La Jolla Nd standard. Nine measurements of the JNdi standard provided an average $^{143}Nd/^{144}Nd = 0.512112 \pm 0.000003$ (2se). Most samples had 2se uncertainties on $^{143}Nd/^{144}Nd < 0.000005$ except for TG89-12 where the uncertainty is 0.000017.

Os isotopic compositions were measured on the DTM Thermo-Fisher Triton by negative thermal ionization with the OsO_3- ion. Samples were loaded in HBr onto single platinum filaments and then covered with $Ba(OH)_2$. An oxygen leak valve was used to obtain pressures of ~2 x 10^{-7} torr in the ion source region during analysis. Most samples were run by peak-hopping in the single electron multiplier. The Trinity peridotite (TG89-12) was run statically on faraday cups. For TG89-12, ^{188}Os was 1.3 x 10^{-12} amps. Other samples were run at ^{192}Os ranging from 16000 cps (TG83-58) to generally above 60,000 cps. Data are fractionation corrected to $^{192}OsO_3/^{188}OsO_3 = 3.091878$, then corrected for oxygen isotope composition using the oxygen isotope composition reported by Nier (1950), and finally re-fractionation corrected to $^{192}Os/^{188}Os = 3.082609$. The average $^{187}Os/^{188}Os$ measured for the DTM Os standard using static faraday multicollection is 0.1740098 ± 0.0000020 (2se of 7 analyses). The average measured for this standard on the multiplier is 0.17367 ± 0.00007 (2se of 7 analyses). Samples are corrected for ^{187}Re interference by measuring ^{185}Re. $^{185}Re/^{188}Os$ ranged from 0.0015 to 0.031 for the samples measured on the multiplier to 0.000006 for TG89-12. Concentration uncertainties including only the precision of the isotopic measurements was always better than 0.3%. A 2 pg Os blank with $^{187}Os/^{188}Os = 0.174$ was subtracted from all samples. Given the low concentration of several of the samples, this blank constituted as much as 13%, 9%, 7%, and 5% of the Os measured in TG83-58, TG83-46, TG85-41c, and TG82-94a, respectively.

Compositions of minerals were obtained with the MIT five-spectrometer JEOL 733 Superprobe using on-line data reduction. Automation software using the matrix correction procedures of Bence and Albee (1968) with modifications of Albee and Ray (1970) were used, as well as newer automation software that utilized the CITZAF correction package of Armstrong (1995). The later software used the atomic number correction of Duncumb and Reed, Heinrich's tabulation of absorption coefficients, and the fluorescence correction of Reed to obtain a quantitative analysis (Armstrong, 1995). A comparison of the results from the two techniques on a basalt standard glass showed no appreciable difference between the two methods. Analyses of minerals from the PMA samples are shown in Table 4. All analyses were performed using a 15 kV accelerating voltage and a 10 nA beam current using a focused beam spot of ~2

μm. Na was counted at the beginning of the analysis for 5 s and other elements were measured for up to 40 s, depending on abundance level. Analytical precision can be inferred from replicate analyses of an andesite glass working standard (38b-129) from a 0.1 MPa experiment (Grove and Juster, 1989). One standard deviation of replicate glass analyses expressed as relative percent of oxides are SiO_2:0.4%, Al_2O_3:0.9%, CaO:1.5%, MgO:1.5%, FeO:1.4%, MnO:8.1%, P_2O_5:5%, Na_2O:1.9%, K_2O:1.1%, based on 289 individual measurements over 28 analytical sessions.

Compositional Variations in the PMA Minerals

The lavas at the S17 cinder cone contain ~ 4 – 8 volume% phenocrysts that consist of olivine (Fo_{87} to $Fo_{94.1}$) from 0.5 to 10 mm in size. Olivine is compositionally uniform in the interior of the phenocrysts and surrounded by a thin normally zoned rim (Figure 2a). Pyroxene phenocrysts in the S17 samples are both normally and complexly, reverse-zoned (Figure 2b and Figure 3). There are distinct populations of normally to sector-zoned high-magnesian high-Ca pyroxene (cpx, Wo_{41}, Mg# = 90, 0.2 to 2 mm; Mg# = 100*[Mg / (Mg + Fe)]; Wo = 100*[Ca / (Ca + Mg + Fe)]; molar), iron-rich orthopyroxene (opx) and cpx (Wo_3 and Wo_{41}, Mg# = 69, 0.2 to 2 mm) and rare sieve plagioclase (0.2 to 1 mm). The orthopyroxene phenocrysts containing iron-rich portions show textural evidence of reaction with the host magma (Figure 2b). The opx in Figure 2b preserves an unreacted core (Mg# = 69) and wormy reaction zone that contains trapped melt inclusions, wisps of unreacted opx and reacted opx with Mg# = 85. In turn these reacted interiors are surrounded by a more magnesian overgrowth rim (Mg# = 94).

In the Vent 2 lava (88-23) the phenocryst assemblage is dominated by olivine (Fo_{87} to Fo_{91}) with rare Fo_{92-94} olivines, magnesian high-Ca pyroxene (cpx, Wo_{41}, Mg# = 90) and only rarely are iron-rich opx and cpx and plagioclase present. In the lava flows the phenocryst assemblage is dominated by olivine (Fo_{90} to $Fo_{93.8}$), magnesian high-Ca pyroxene (cpx, Wo_{41}, Mg# = 90). The eastern trending lava flow is compositionally zoned, with the most magnesian composition represented in the eruption occurring at its

distal end (see 07-28, Table 1). This sample dominantly contains of olivine (Fo_{90-91}) and magnesian cpx (Mg# = 90) with rare olivines with compositions of Fo_{92-94} (Table 4).

Spinel is also present and is included in the high-Fo olivines, Fo_{87-94}, as 0.1 to 0.2 mm euhedral octahedral.. Baker et al. (1994) presents an analysis of these spinels with a Cr# (100*[Cr/(Cr+Al)], molar) of 83 with and Mg# of 66. Euhedral Cr-rich spinels are commonly found in the primitive olivines of the PMA samples from Mt. Shasta, both from the second cinder cone and the lava flows. The compositions of spinels from the Mt. Shasta PMAs are plotted in Figure 4 as Cr# vs. Mg# to compare them with the compositions of spinel in PMAs from Mt. Lassen (Clynne and Borg, 1997) and the spinels found in the Trinity peridotite (Quick, 1981).

Major Element Compositional Variations in PMA Lavas

As a consequence of remapping and sampling the compositional range of the PMA lavas have been extended considerably, allowing the mixing and the primitive PMA parental magma to be identified. The key compositional variations in major elements are shown in Figure 5 where the compositions of bombs from the S17 cinder cone and the samples from lava flows and Vent 2 are compared with Shasta stratocone andesites (Grove et al., 2005), Shasta-region primitive basaltic andesites (BAs; Baker et al., 1994, Grove et al., 2002, 2003) and glass inclusions in minerals from the S17 PMA sample 85-41b. Also shown in Figure 5 are the experimentally determined crystallization paths at 200 MPa, H_2O-saturated at the Ni-NiO buffer from Grove et al. (2003) on PMA 85-41c and basaltic andesite (BA) 85-44.

The lava flows extend the composition of the PMA magma system to higher MgO contents than those found in the S17 cinder cone (Baker et al. 1994). Samples 07-28, 09-4 and 09-5 span an MgO range from 9.91 to 10.08 wt. %. In contrast the most MgO-rich composition analyzed by Baker et al. (1994) contains 9.14 wt.% MgO (85-41c). The compositions of samples from the flow also extend to lower MgO (7.61 wt.% MgO, 88-23) than the cinder cone (8.05 % MgO, 85-41d). Chemical composition and position in the flow are also correlated. The most distal samples are the highest in MgO and the ones

closest to the vents are lowest in MgO. Samples at intermediate distances are intermediate in composition. Thus, the PMA flow is a compositionally zoned eruption, similar to the Giant Crater flow field at Medicine Lake volcano (Donnelly-Nolan et al., 1991, Baker et al., 1991). Furthermore, the compositional trends of the erupted material in the cinder cone and in the lava flows extend in different direction on major element variation diagrams (Figure 5). The lava flow trend extends toward the compositional array defined by the more evolved BA lavas from the Shasta region. This is defined by the grey arrow in Figure 5 a-d and is characterized by an increase in CaO, Al_2O_3 and FeO with decreasing MgO and a decrease in SiO_2 with decreasing MgO. In contrast, the samples from the S17 cinder cone show decreasing CaO and FeO with decreasing MgO, a less pronounced increase in Al_2O_3 and increasing SiO_2 with decreasing MgO. This trend extends toward the field defined by the Shasta andesites and dacites in Figure 5. These two distinct trends make sense in terms of the contrasting phenocryst populations of the flows and Vent 2 vs. the S17 cinder cone. The flows contain phenocrysts that are common in the BA lavas (Baker et al., 1994); magnesian olivine and high-Mg# cpx. In contrast, the S17 vent samples contain the iron rich opx and cpx and plagioclase, indicative of mixing with andesite and dacite magmas.

Compositional Variations in Melt Inclusions in PMA Minerals

Melt inclusions are present in PMA minerals and were originally the major tool that Anderson used to characterize the compositional characteristics of the PMA (Anderson, 1974, 1976a,b, 1979). We have analyzed melt inclusions in the S17 samples and find 5 distinct populations (Table 5). One is characterized by high CaO, high CaO/Al_2O_3 and has the highest Mg#s. This was recognized by Anderson and these were not in our sample (85-41b) and are not plotted on Figure 5. The second melt inclusion population is trapped in Fo90-Fo91 olivine and high-Mg# clinopyroxene that grew after magma mixing and prior to eruption. These melt inclusions are most similar to the primitive basaltic andesite lavas that are present at other locations in the vicinity of Mt. Shasta. A fourth population of melt inclusions is

trapped in iron-rich opx and cpx. The melt is andesitic to dacitic (63 - 70% SiO_2) and it represents an evolved magma that was mixed with the primitive andesites. A fifth melt inclusion population is andesitic (61 % SiO_2, 5 to 6 % Na_2O, 0.1 K_2O). This melt inclusion population is associated with reacted and resorbed Fe-rich opx and plagioclase (Figure 2b). The composition of these melt inclusions with high Al_2O_3 and Na_2O, very low K_2O and high FeO are most consistent with an origin by remelting of cumulate clots of minerals. These melt inclusions are trapped at the reacted core of the opx crystal pictured in Figure 2b.

Anderson (1976) described the mixing of "basaltic" and dacitic liquids with crystals of olivine, plagioclase and pyroxene to form the magmas that erupted at the S17 cinder cone. The basaltic liquid was inferred based on the presence of primitive olivine and orthopyroxene crystals found in the PMA cinders and bombs, along with glass inclusions described as basaltic. Anderson (1976) included a major element analysis of an example of the "basaltic" inclusions, and the analyses reported an average (normalized to anhydrous, 100 wt%) SiO_2 content of 56.8 wt%, with unnormalized values ranging from 53.7 wt% to 55.8 wt%. These primitive mafic components are what Baker et al. (1994) and Grove et al. (2002, 2003) refer to as basaltic andesite (51 – 53 wt. % SiO_2) and primitive magnesian andesite (57 – 59 wt. % SiO_2). The dacitic component was inferred based on dacitic glass inclusions in Fe-rich orthopyroxenes and from the presence of sieve textured plagioclase feldspar grains. Anderson (1976) also noted the presence of andesite glass inclusions, 58.5 wt% SiO_2 (averaged and normalized to 100 wt%), in olivines (Fo_{89-90}) that lacked the orthopyroxene reaction rims of the most primitive (Fo_{93-94}) olivines in the samples. These andesite glass inclusions were attributed to the trapping of a fully hybridized mixture of the basaltic and dacitic melt, with the addition of small amounts of plagioclase and the crystallization of olivine and orthopyroxene. Anderson (1976) went on to point out that the glass inclusions of the hybrid andesite had H_2O contents of ~2 wt%, which was lower than the ~4-6 wt% estimated for the "basaltic" component. The study concluded that all the observed evidence conclusively illustrated that the andesites found at the S17 locality were hybrids of crystal poor dacitic and "basaltic" magmas.

Discussion

Multi-Component Magma Mixing in the Mt. Shasta PMAs

Samples from the S17 locality contain complexly zoned clinopyroxene grains that preserve evidence for multiple episodes of mixing. Figure 3 shows a clinopyroxene in sample 09-7 that preserves chemical zonation of major and minor elements. The inner most portion of the clinopyroxene (Stage 1), nearest to the core of the grain, has low Cr_2O_3 (~0.18 wt%), high TiO_2 (~0.4 wt%), and low Mg# (~81). The composition abruptly changes as the analyses progress outward, indicating that the evolved clinopyroxene entered a more primitive, depleted magma due to the increase in Cr_2O_3 (~0.9 wt%) and Mg# (~91), and the decrease in TiO_2 (~0.08) (Stage 2). This is followed by a zone of gradually decreasing Cr_2O_3 content at a nearly constant Mg# and TiO_2 content for (Stage 3). Following the gradual decrease in Cr_2O_3 there is a more steady decrease in the Cr_2O_3 content that is coupled with a decrease in the Mg# and an increase in the TiO_2 content of the pyroxene (Stage 4). The composition of the pyroxene becomes like that of the pyroxene seen near the core of the grain (Stage 1), with Mg# ~79, Cr_2O_3 ~0.17 wt%, and TiO_2 ~0.39 wt%. The zoning then indicates another abrupt change in composition (Stage 5), indicative of mixing the clinopyroxene grain into another primitive, depleted magma that produces pyroxene growth like that seen in the first mixing event recorded in the grain: Mg# ~90, Cr_2O_3 ~ 1.0 wt%, and TiO_2 ~0.4 wt%.

This clinopyroxene grain preserves a record of having been mixed into a primitive depleted magma during two different episodes. The early history of the grain indicates that it was in a more evolved magma with and Mg# ~50 ($_{Fe\text{-}Mg}{}^{Cpx\text{-}Liq}K_D = 0.25$) during the Stage 1 growth. Stage 2 growth of the clinopyroxene indicates it was mixed into a primitive, depleted liquid that had an Mg# ~72 and a low TiO_2 content. During Stage 3 the clinopyroxene records a progressive decrease in Cr_2O_3 content with very little change in Mg# or TiO_2 content, indicating the crystallization of Cr-spinel from the primitive, depleted magma. Stage 4 records continued evolution of the magma to lower Mg#s and higher TiO_2

contents, which is indicative of fractional crystallization of the host magma. The most evolved clinopyroxene indicates that the host magma once again reached Mg#s ~48-50 before the second mixing event occurred. The second mixing, Stage 5, produces clinopyroxene with the same composition as the clinopyroxene grown in Stage 2, which would be in equilibrium with a liquid having an Mg# ~71. The overgrowth zones of Stage 2 and Stage 5 exhibit some minor embayments of the earlier growth zones, indicating that during the mixing events the clinopyroxene may have entered a magma that was not initially saturated with clinopyroxene. However, upon further evolution of the magma clinopyroxene became stable and the primitive clinopyroxene overgrowths began to form. This means the Mg#s of the liquids in equilibrium with the most primitive clinopyroxenes represent a lower bound for the Mg# of the primitive magma. Additionally, the compositions of reversely zoned orthopyroxenes are similar in Mg# to the evolved and primitive clinopyroxene compositions of the grain described above and likely grew from the same mixing magmas. The outer most zone of both of the populations of pyroxene can be directly correlated to the mafic magma in which they are now hosted, a PMA. The similarities in the chemistry of Stage 2 and Stage 5 clinopyroxene growth indicate that the crystal preserves evidence of recharging a magma chamber or conduit by PMA magmas, which subsequently evolve to dacites via fractional crystallization. Since this would suggest that the clinopyroxene originally crystallized in a fractionating PMA magma that was just rejuvenated by later injections of the same magma type, the crystal would be termed an antecryst instead of a xenocrysts (Hildreth, 1981).

The reaction textures preserved in the iron-rich, reversely-zone opx in Figure 2b preserve evidence of extended residence times in a magma chamber sufficient for a silicate melt to react and reequilibrate an orthopyroxene of Mg# 69 to one with Mg# 85, and then the sharp magnesian overgrowth rim in Figure 2b shows evidence for recharge by primitive PMA magma. In the experimental study of Grove et al.(2003), PMA 85-41c was used to determine a liquid line of descent at 200 MPa, H_2O-saturated. The most evolved liquid reported is a dacite (85-41c#9, 65.6 wt. % SiO_2, F = 0.40) and contains opx with an Mg# of 76. To produce an opx with Mg# of 69 would require even further crystallization. The mid-80's Mg# in the opx reaction zone and in the cpx crystal in Figure 3 would have

crystallized from an andesitic PMA derivative liquid (e.g. 85-41c#8, 62.7 % SiO_2, F = 0.46) that contains opx with Mg# of 83.5. Therefore, fractional crystallization of a PMA parent lava followed by recharge of a new batch of PMA magma that crystallized before another recharge event entered and triggered an eruption of mixed PMA melts can explain the mineral compositions and textures that are observed in the PMA cinder cone. The andesitic and dacitic melt inclusion population trapped in the Fe-rich minerals (Table 5 and Figure 2) is roughly coincident at 65 to 69 wt. % SiO_2 with the liquid compositions in 85-41c that crystallize pyroxenes with the same Mg# range as those containing the trapped melt inclusions. The PMA lavas identified in this study do not contain the complexly zoned pyroxene populations observed in the cinder cone samples, suggesting that perhaps they had a more direct passage through the magmatic conduit system.

Primitive Parental PMA Melts

Anderson (1974b) originally described the occurrence of Fo94 olivines from the S17 locality PMA samples. This has been noted by many subsequent researchers (e.g. Baker et al., 1994, Grove et al., 2005) and is one of the pieces of evidence cited by Streck et al. (2007) to indicate interaction with the Trinity ultramafic body. Streck et al. (2007) noted that phenocrysts of Fo_{87} represent the equilibrium composition phenocrysts that crystallized just prior to eruption; however, the less common high-Fo olivines (Fo_{90-94}) must represent xenocrystic material from the underlying ultramafic body. In the studies of Anderson (1973, 1974a,b, 1976, 1979) and the more recent work of Ruscitto and Wallace (2008), it is shown that the high-Fo olivines contain volatile-rich, primary, magmatic melt inclusions that are thought to have been trapped during the early skeletal growth history of the crystals. This is in stark contrast to the proposal that the olivines are derived from a crustal level peridotite massif proposed by Streck et al. (2007).

High-Fo olivines are also found in all of the PMA lava flow samples examined in this study as well as all samples in this study from the S17 locality. The olivine compositions vary continuously from Fo_{94} to Fo_{84}, with possible gaps in sampling or occurrence of compositions between $Fo_{92.5}$-Fo_{91} and Fo_{87}-

Fo_{85} (Figure 6). The high-Fo olivines are sometimes rimmed by orthopyroxene that has an Mg# similar to the Fo content of the outermost olivine, suggesting that the olivines have seen a low-pressure peritectic reaction whereby olivine reacts with the surrounding melt to produce orthopyroxene. This probably occurred during the ascent or eruption of the PMA magma carrying the high-Fo olivine phenocrysts, and does not necessarily indicate that the olivines are xenocrystic. The lack of reverse zoning in the olivines also indicates that the most primitive olivines do no record an extensive history of mixing and fractional crystallization.

Analyses of the PMA olivines display increasing Ca and Mn and decreasing Ni as the Fo content decreases. The high Ni contents of the most primitive olivines are similar to contents found in fertile peridotite olivines, however the low Ca and Mn contents of the most primitive olivines and the increasing Ca and Mn contents of the olivines as they become less magnesian is clearly indicative of a magmatic origin for all of the olivines of the PMAs. The most primitive PMA reported for Mt. Shasta is sample 07-28 of the current study. Assuming all of the Fe analyzed is Fe^{2+}, the sample is Mg# 75.5. For an $^{Olv\text{-}Liq}{}_{Fe\text{-}Mg}K_D = 0.3 \pm 0.03$, the sample would be in equilibrium with $Fo_{90\text{-}92}$ olivine. The sample contains olivine crystals with core compositions from $Fo_{90\text{-}94}$, indicating that the most magnesian olivines can not easily be explained as phenocrysts that crystallized directly from the 07-28 PMA.

Arc magmas display a large variation in fO_2 conditions, suggesting that the Fo_{94} olivines found in the Mt. Shasta PMAs could be the result of crystallization at oxidizing conditions. Grove et al. (2005) estimated the fO_2 conditions of NNO+1 log unit to NNO-1 log unit for lavas at Mt. Shasta, based on coexisting oxide mineral phases (ulvöspinel-magnetite and ilmenite-hematite), which provides an estimate for the range of fO_2 conditions for the crystallization of the PMA. If the PMA 07-28 has not undergone any crystal fractionation, 28% of the FeO* in the sample would need to exist as Fe^{3+} for the 07-28 bulk composition to be in equilibrium with Fo_{94} olivine. The work of Kress and Carmichael (1991) can be used calculate the percentage of Fe^{3+} in a magma as a function of the temperature and the fO_2. Grove et al. (2003) determined the 0.1 MPa liquidus temperature of 1250°C for the PMA 85-41c, which is slightly less primitive than the 07-28 PMA. This liquidus temperature can be extrapolated to high

pressures (200 MPa) indicated by the study of Grove et al. (2005), yielding an estimated anhydrous liquidus of ~1300°C. Using the model of Medard and Grove (2008), this anhydrous liquidus can be adjusted for the liquidus lowering effects of H_2O dissolved in the magma. Estimates for the H_2O content of the PMAs at Mt. Shasta range from ~2.5 wt% (Anderson, 1973) to 6 wt% (Baker et al., 1994), which translates to a liquidus temperature decrease of between 85°C and 160°C. This yields a possible temperature range of ~1215°C to ~1140°C for the hydrous liquidus temperature. The equation of Huebner (1971) for the Ni-NiO (NNO) buffer, including the pressure correction, is used to calculate the fO_2 at the pressure and temperature of interest. With Eq. 7 of Kress and Carmichael (1991), for temperatures of 1215°C to 1140°C and an fO_2 value of NNO+1 log unit, the calculated Fe^{3+}/Fe_{Total} in the 07-28 bulk composition is 28-29%. With this estimate for the Fe^{3+} content of the PMA magma, the FeO content of the melt would be 4.19 wt% (normalized anhydrous). This liquid composition is in equilibrium with Fo_{93}-Fo_{94} olivine ($^{Olv\text{-}Liq}{}_{Fe\text{-}Mg}K_D = 0.30 \pm 0.03$), indicating that the PMA lava composition of 07-28 is in equilibrium with the enigmatic Fo_{94} olivine core compositions known from the PMA lavas and cinders.

Sample 07-28, from the end of the western lava flow, is an excellent candidate for a primitive, high-degree, hydrous mantle melt of PMA composition. The olivine phenocrysts that do not preserve $Fo_{93\text{-}94}$ cores can be interpreted based on the magma mixing components identified above and the compositional zoning observed for the PMA lava flow. The mixing trend indicated by the gray arrow in Figure 5 trends toward an evolved liquid with a composition similar to that of Shasta-region BAs that have undergone small amounts of fractional crystallization. An example from the Grove et al. (2003) experiments on primitive BA 85-44 (85-44#7, 54.6 wt. % SiO_2, F = 0.95, olivine $Fo_{84.5}$) is a possible end member of mixing that would contain cpx and olivine crystals ($Fo_{87\text{-}85}$) similar to those found in both the PMA cinder cone samples and in the lavas. The olivines with cores of $Fo_{92\text{-}90}$ olivine likely record events of increased crystal nucleation formed during or just after the mixing event that produced the S17 cinder cone magmas and the compositionally zoned lava flow (Baker et al., 1994).

Testing the Streck et al. (2007) Trinity Peridotite Component in PMA Magmas

Anderson (1979) discussed the possibility that the Trinity Ultramafic complex may be the source of the most primitive olivine and orthopyroxene phenocrysts in the PMA magma. Anderson (1979) suggested that the decomposition of the serpentinized peridotites of the Trinity ultramafic body may not only explain the primitive nature of the high-Fo olivines but also the presence of elevated Cl concentrations in some of the analyzed melt inclusions studied by Anderson (1974a).

This concept was revived by the work of Streck et al. (2007), which asserted that PMA magmas are not mantle derived melts but instead are formed by mixing dacites and basalts. Streck et al. (2007) called upon the same phenocryst evidence originally proposed by Anderson (1976) as evidence that there were dacites and basalts mixing to form the hybrid andesite, however they found that to mass balance the dacites and basalts they needed another component to add additional high-Mg# character to the mixture. Streck et al. (2007) then adopted the suggestion from Anderson (1979) that material from the Trinity ultramafic sequence was involved and that the hybrid andesite mixture inherited the primitive olivine and orthopyroxene grains directly from a hypothetical, not observed in nature (Quick, 1981), harzburgite.

They developed two different mixing models that mixed a Mt. Shasta dacite (83-58; Grove et al., 2003) with a basalt (Model 1: HAOT 85-38 and Model 2: calc-alkaline basalt 85-1a; both from Baker et al., 1994) and a harzburgite contaminant (75% $Fo_{93.7}$ olivine and 25% Mg# 89.6 orthopyroxene) to produce the major element contents of two samples from the S17 PMA locality (MS1604; Streck et al., 2007 and 85-41; Baker et al., 1994). The two models work well to reproduce the majority of the major elements for the two PMA samples in their study, however it is noticeably poor in the reproduction of Al_2O_3, models are too high by ~0.7 to 1.0 wt% Al_2O_3, and CaO, models are too low by ~0.7 to 1.0 wt% CaO. Only removal of a portion of the dacite component can produce a better fit for both the Al_2O_3 and the CaO, however lowering the proportion of the dacite in the mixtures would lower the SiO_2 content of the mixtures. The high SiO_2 contents of the Mt. Shasta PMA is one of the defining characteristics of the samples so retaining the correct SiO_2 content is important in constructing an argument that the PMA composition is just a mixture of dacite and basalt with ultramafic contamination. By defining the mixing

end members, Streck et al. (2007) have provided a testable solution to the mixing scenario that was originally proposed in the work of Anderson (1976).

A. Phenocryst Evidence Against Mixing with the Trinity

The studies of Anderson (1976, 1979), Baker et al. (1994), Grove et al. (2002, 2005), and Streck et al. (2007) identify high-Fo (Fo_{93-94}) olivine grains in the samples from the S17 locality. High-Fo olivines (Fo_{93-94}) have also been found in the PMA lavas identified in this study indicating a possible link between the lavas and the cinder cone or a more universal process that affects all instances of PMA generation at Mt. Shasta. Anderson (1976) and Anderson (1979) interpreted these olivines as being xenocrysts from either the "basaltic" component of the hybrid andesite or as evidence for the incorporation of material from the Trinity ultramafic body. Similarly, Streck et al. (2007) also used these high-Fo olivines as evidence for the incorporation of a harzburgite component thought to be from the Trinity ultramafic body. Baker et al. (1994) presents an analysis of the high-Fo olivine along with the composition of a spinel included in the olivine. The olivine is Fo_{94} and the spinel has a Cr# of 83 with an Mg# of 66. Euhedral Cr-rich spinels are commonly found in the primitive olivines, Fo_{87-94}, of the PMA and BA samples from the Mt. Shasta region.

The Trinity ultramafic body has been examined in detail by Quick (1981), which studied the lithologic and petrologic diversity of the ultramafic body. Quick (1981) provides mineral compositions for the major mineral phases in the different lithologies of the peridotites and associated ultramafic rocks in the Trinity. The study found that the majority of the olivines in the peridotite were Fo_{90-91} in the lherzolite, harzburgite, and dunite lithologies, with Fo_{92-93} olivines occurring rarely in the plagioclase lherzolites. Quick (1981) also analyzed the compositions of the Cr-spinels found in the Trinity peridotite lithologies and found the range in compositions to be similar between the different peridotite lithologies. The spinel compositions range from Mg# 52-65 and Cr# 43-63 with the harzburgite spinels being Mg# 52-60 and Cr# 54-60 (Figure 4). The study by Quick (1981) clearly shows that the Fo94 olivines with included, euhedral, spinels of Cr#s >70 are not represented in the Trinity ultramafic complex despite

being ubiquitous in the PMA lavas found at Mt. Shasta. Texturally, the spinel grains in the Trinity perdiotites are quite distinctive and occur as anhedral, equigranular crystals form 5 to 10 mm in size, as multiple grain intergrowths not included in olivine. This contrasts with the euhedral, fine-grained (10 – 100 microns) character of the Cr-rich spinel included in the PMA and BA olivine phenocrysts.

The study of Kamenetsky et al. (1997) noted an occurrence of lavas that include similarly high-Fo olivines and Cr-rich spinels. In the study they identified forsteritic olivines, up to Fo_{94}, with Cr-spinels, Cr# 78-87, along with primitive orthopyroxene and clinopyroxenes in lavas from the Lau Basin. The lavas were produced by decompression melting, due to a southward propagating spreading backarc spreading center, of refractory hydrated sub-arc lithosphere from the Tofua arc. (Kamenetsky et al.,1997). Despite the more complicated tectonic history of the samples, the lavas that crystallized these unusual phases were produced through hydrous melting of a refractory mantle lithosphere created in a sub-arc mantle wedge, as would be expected for the PMA magmas at Mt. Shasta.

Studies by Clynne and Borg (1997) and Borg and Clynne (1997) identify PMA lavas further south in the Cascades, at Mt. Lassen. The Trinity ultramafic body is not inferred to occur underneath Mt. Lassen, however similar PMA lavas are found at this location. The Mt. Lassen PMA lavas have not been found to include Fo94 olivines, however the most primitive olivines identified in the PMA samples, Fo_{91}, do include high-Cr# spinels similar to those of the PMA lavas from Mt. Shasta (Figure 4). Clynne and Borg (1997) interpret the primitive olivines and high-Cr# spinels to be primary crystallization products of the Mt. Lassen PMA magmas, which resulted from fluid-rich melting of a refractory mantle lithosphere in the Cascade subduction zone beneath Mt. Lassen.

B. Isotopic Evidence Against Dacite Mixing to Produce PMAs

In response to the study published by Streck et al. (2007), Barr et al. (2007) compiled published Nd and Sr isotopic data for the proposed mixing end members to show that the mixing proportions used by Streck et al. (2007) could not reproduce the isotopic composition of the PMA magma from the S17 locality. Sr and Nd isotopic analyses presented in the current study, for the newly identified PMA lavas as

well as sample 85-41c of the S17 locality, match the composition reported by Grove et al. (2002) for PMA sample 85-41b (Table 3 and Figure 7). Barr et al. (2007) also compiled Sr and Nd data from the literature for the variety of ultramafic lithologies for the Trinity ultramafic body in order to estimate the influence this material would have on the mixing models. The isotopic compositions of the Trinity peridotite samples vary greatly (Gruau et al., 1995 and Jacobsen et al., 1984), however the low Sr and Nd contents of the Trinity peridotites have little effect on the overall composition of the mixtures, which are dominated by the composition of the dacite mixing member. The mixtures of dacite and HAOT or primitive basaltic andesite (PBA) (referred to as CAB in Streck et al., 2007), following the proportions proposed by Streck et al. (2007) are shown in Figure 7. These mixtures do not include an estimate for the composition of the hypothetical ultramafic component, thus can be combined with the values presented by Barr et al. (2007) to illustrate the total variability expected for these mixing models. These mixtures can not reproduce the Sr and Nd isotopic compositions of the Mt. Shasta PMA lavas. Dacites from Mt. Shasta exhibit a wide range in isotopic composition and trace element abundances (e.g. Grove et al., 2002), thus making the compositions of dacite mixtures heavily dependant upon the composition of the chosen dacite, however no dacite currently known from Mt. Shasta can be used in a mixing scenario to simultaneously reproduce the major element and Sr and Nd isotopic composition of Mt. Shasta PMAs.

It is conceivable that the true dacite mixing end member required by the models of Streck et al. (2007) is not represented at the surface at Mt. Shasta, however any mixture that is largely composed of dacite, which is needed to reproduce the high SiO_2 contents of PMAs, will require an ultramafic component in order to offset the low Mg# of the dacite. In the case of Mt. Shasta, the source of the ultramafic material has been proposed to be the Trinity ultramafic body. It was shown above that the crystals found in the PMAs of Mt. Shasta that were thought by Anderson (1976) and Streck et al. (2007) to be pieces of the Trinity ultramafic body, in fact do not match the compositional or textural characteristics of any known material from the Trinity ultramafic body. However, there are many ultramafic bodies west of the Cascade arc in northern California, and some may include lithologies that are similar to the proposed ultramafic material found in the PMA lavas (Medaris, 1975).

In order to test the hypothesis that PMAs are formed by dacite mixtures that have interacted with a crustal level ultramafic body, we analyzed the Os isotopic compositions of Mt. Shasta lavas and a sample of Trinity peridotite (Figure 8). Residues of mantle melting have been observed to have low $^{187}Os/^{188}Os$ and high concentrations of Os (e.g. Parkinson et al., 1998). The sample of Trinity peridotite analyzed in this study displays the same characteristics (Figure 8). The peridotite has both the highest concentration of Os and the most unradiogenic Os of all the samples in this study, whereas the dacites 83-58 and 83-46 (of Grove et al., 2002) were found to contain the least amount of Os and the highest $^{187}Os/^{188}Os$ of all the samples. The samples of PMA, HAOT, and one of the PBAs have Os compositions similar to the dacites, and the other PBA analyzed in this study has $^{187}Os/^{188}Os$ similar to the other primitive lavas except with almost an order of magnitude higher Os concentration. Figure 8 includes a mixing model calculated by using a 2:1 ratio of dacite (83-58) and HAOT (85-38), like that of Model 1 of Streck et al. (2007), and mixing in 0.1% to 7% of the Trinity peridotite. The mixing model illustrates the result of interaction of a dacite mixture with a crustal ultramafic body. Due to the high concentration of Os and low $^{187}Os/^{188}Os$ composition, the amount of influence the ultramafic body can produce on the dacite mixture must be less than 0.2% of the total Os in order to produce a composition similar to the PMA. Os is highly incompatible in silicate minerals compared to silicate melts (e.g. Burton et al., 2002), so the interaction of magma with a crustal ultramafic body would not gain appreciable amounts of Os via physical entrainment of crystalline debris; however, the interaction of the magma with the ultramafic body would be expected to strongly contaminate the dacite. The Os scavenged by a dacitic magma would overwhelm the low Os abundance of the dacite, thus making it unlikely that the PMAs could inherit a primitive Mg# component from a crustal level ultramafic body.

Mt. Lassen PMAs

The occurrence of PMA lavas at Mt. Lassen is well documented (e.g. Clynne and Borg, 1997, and Borg et al., 1997, Table 1 of this study). The Mt. Lassen PMAs do not contain the disequilibrium pyroxenes and high-Fo olivines that are common in the S17 PMA samples at Mt. Shasta, however the

lavas share many chemical characteristics with the lavas from Mt. Shasta. The lavas have similar major and trace element composition, including the elevated SiO_2, Mg#, and Ni contents, as well as large ion lithophile element enrichments and high field strength element depletions (Baker et al., 1994, Clynne and Borg, 1997, Borg et al., 1997). The olivine compositions of the Mt. Lassen PMAs do not include Fo_{93-94} olivines like the Mt. Shasta PMAs, however the most primitive olivines (Fo_{91-92}) exhibit higher Ni contents compared to those from the Mt. Shasta PMAs (Figure 6). Clynne and Borg (1997) found that the primitive olivines have euhedral spinel inclusions that have Cr#s and Mg#s similar to those found in the primitive olivines of the Mt. Shasta PMAs (Figure 4). The Mt. Lassen PMAs have high $^{187}Os/^{188}Os$ and low Os contents (Figure 8; Borg et al., 2000), which is inconsistent with the assimilation of an ultramafic crust (Hart et al., 2002 and Borg et al., 2000). The Sr, Nd, and Pb isotopes of the PMAs display primitive values indicative of a mantle origin (Borg et al., 1997), despite having elevated $\delta^{18}O$ relative to typical mantle (Borg et al., 2000). The elevated $\delta^{18}O$ is a characteristic also shared by the PMAs at Mt. Shasta, although the nature of this enrichment is not well understood (Bindeman et al., 2005).

Primitive magnesian andesite lavas have been identified in other arcs around the globe. Wood and Turner (2009), Grove et al. (2003) and Gaetani and Grove (2003) summarize these occurrences in New Zealand, Papua, New Guinea, Japan and the Aleutians. Any explanation used to explain the production of PMA magmas must be widely applicable to a variety of arc settings, circumstantially suggesting that PMAs are direct melts of the mantle during arc volcanism.

Wood and Turner (2009) Estimates of Pressure and Volatile Content

Grove et al. (2003) explain the mantle origin of PMAs at Mt. Shasta based on their experimental investigations and those of Baker et al. (1994). Their conclusions are that the PMA magmas were likely generated by high extents of hydrous melting of the sub-arc mantle that left a harzburgite residue. The recent work of Wood and Turner (2009) has proposed an algorithm by which the H_2O content and pressure of melt generation can be determined for mantle melts in equilibrium with a harzburgite, based on their SiO_2, MgO and alkali ($Na_2O + K_2O$) contents. The study works by estimating the effect of the

H_2O on the MgO and SiO_2 content of melts of harzburgites as compared to an estimate of the anhydrous melts of the same composition. They propose that there is an increase in the MgO and SiO_2 contents of harzburgite melts under hydrous melting conditions versus anhydrous conditions. Wood and Turner (2009) go on to estimate the pressure of melt generation based on the composition of the melt of interest and an estimate of its effective H_2O content, adjusted from the original H_2O content according to the CO_2 content. Figure 9 illustrates the results of this calculation performed on the PMAs of Mt. Shasta (07-28 and 85-41c) and Mt. Lassen (LC86-1009). The results are shifted to a lower pressure at 4.5 wt% H_2O compared to the experimental results of Baker et al. (1994), but this is expected due to the experimental residual assemblage under those conditions produced a liquidus saturation with olv + opx + cpx (Grove et al., 2003) rather than a harzburgite (olv + opx). In order to produce the PMA compositions at mantle pressures (>~1.0 GPa), the melt H_2O contents must be 6 wt% or greater. This agrees well with the estimates of Grove et al. (2003) for the PMA composition 85-41c from Mt. Shasta. The more primitive PMA 07-28 requires slightly less H_2O for a given pressure of equilibration compared to 85-41c, however the difference is less than the expected sensitivity of the model. Also, the PMA from Mt. Lassen appears to have formed at either lower pressure conditions or with a higher H_2O content than the PMAs at Mt. Shasta, although the melting of a less depleted mantle source and lower extents of melting can not be ruled out as causes of the compositional differences.

Mixing Models Using Mt. Shasta Dacites

There has been extensive petrologic investigation into the dacites at Mt. Shasta (e.g. Baker et al., 1994 and Grove et al., 2005). A universal conclusion found to be true in all of these studies is that there is no evidence for the production of dacite magma through mantle or crustal melting processes. The dacites on and around Mt. Shasta were formed primarily by extensive fractionation and mixing of more primitive magmas such as the primitive basaltic andesites and PMAs discussed by Grove et al. (2005). A logical extension of this observation is that since the more primitive magmas are involved in the production of the dacites, then there should be instances where a batch of the more primitive magmas are

partially mixed with a fraction of a derivative dacite on its way to the surface. Thus seems to be the case for the PMA magmas from the S-17 locality, although the most primitive compositions show very little dacitic involvement.

For all of the Mt. Shasta andesites and dacites examined by Grove et al. (2005), each sample that has orthopyroxene phenocrysts also have plagioclase feldspar phenocrysts and another mafic phenocryst phase(clinopyroxene or olivine) present. In order to use such a dacite as a mixing component, all of the phenocryst populations should be identifiable in the mixed lava; however these phenocrysts, including the evolved orthopyroxenes, are not observed in the most primitive PMA at Mt. Shasta, 07-28. Thus it can easily be concluded that the high-SiO_2 composition of Mt. Shasta PMAs is not a result of mixing with dacitic magmas.

Conclusions

1. Primitive magnesian andesite magmas occur as lava flows, in addition to cinders and bombs of the S17 locality, at Mt. Shasta volcano in northern California. These lavas are geochemically similar to previous analyses of PMA samples from the S17 locality, and preserve compositions that represent the most primitive PMAs known from Mt. Shasta. The lavas contain high-Fo olivine phenocrysts (Fo_{90-94}) with high Ni contents, and the olivine phenocrysts contain euhedral, high-Cr# spinels. Within the range of measured H_2O contents of the PMA magmas and oxygen fugacities estimated for Mt. Shasta lavas, the Fo_{94} olivine cores are in equilibrium with the most primitive PMA sample identified in this study (07-28). The S17 locality PMAs contain complexly zoned pyroxene antecrysts that preserve evidence of mixing and subsequent evolution of multiple batches of PMA, BA and dacite magmas in the magmatic plumbing system.
2. The PMAs at Mt. Shasta display primitive mantle-like Sr and Nd isotopic characteristics, which is irreproducible by mixing models of Streck et al. (2007). The elevated $^{187}Os/^{188}Os$

and low Os contents of the PMAs provide evidence that they have not seen significant interaction with a crustal ultramafic body, in particular the Trinity ultramafic body.

3. PMA lavas of Mt. Lassen and Mt. Shasta share many petrologic and geochemical characteristics. Similarities in major element, minor element and isotopic compositions as well as phenocryst compositions, along with the lack of evidence for ultramafic contamination at both sites, suggests that PMA magma generation is the result of mantle melting that occurs throughout the southern Cascades.

Bibliography

Albee, A.L., and Ray, L., 1970, Correction factors for electron probe microanalysis of silicates, oxides, carbonates, phosphates and sulfates: Analytical Chemistry, v. 42, p. 1408-1414.

Anderson, A.T., 1973, The before-eruption water content of some high alumina magmas: Bulletin of Volcanology, v. 37, p. 243-267.

Anderson, A.T., 1974a, Chlorine, Sulfur, and Water in Magmas and Oceans: Geological Society of America Bulletin, v. 85, p. 1485-1492.

Anderson, A.T., 1974b, Evidence for a picritic, volatile-rich magma beneath Mt. Shasta, California: Journal of Petrology, v. 15, p. 243-267.

Anderson, A.T., 1976, Magma-mixing: Petrological process and volcanological tool: Journal of Volcanological and Geophysical Research, v. 1, p. 3-33.

Anderson, A.T., 1979, Water in some hypersthenic magmas: Journal of Geology, v. 87, p. 509-531.

Armstrong, J.T., 1995, Citzaf - a package of correction programs for the quantitative Electron Microbeam X-Ray-Analysis of thick polished materials, thin-films, and particles: Microbeam Analysis, v. 4, p. 177-200.

Baker, M.B., Grove, T.L., and Price, R.C., 1994, Primitive basalts and andesites from the Mt. Shasta region, N. California: products of varying melt fraction and water content: Contributions to Mineralogy and Petrology, v. 118, p. 111-129.

Barr, J.A., Grove, T., and Elkins-Tanton, L.T., 2007, High-Magnesian andesite from Mount Shasta: A product of magma mixing and contamination not a primitive melt: COMMENT: Geology v. Online Forum, p. e147-e148.

Bence, A.E., and Albee, A.L., 1968, Empirical correction factors for the electron microanalysis of silicates and oxides: Journal of Geology, v. 76, p. 382-403.

Benz, H.M., Zandt, G., and Oppenheimer, D.H., 1992, Lithospheric structure of northern California from teleseismic images of the upper mantle: Journal of Geophysical Research, v. 97, p. 4791-4807.

Bindeman, I.N., Eiler, J.M., Yogodzinski, G.M., Tatsumi, Y., Stern, C.R., Grove, T.L., Portnyagin, M., Hoernle, K., and Danyushevsky, L.V., 2005, Oxygen isotope evidence for slab melting in modern and ancient subduction zones: Earth and Planetary Science Letters, v. 235, p. 480-496.

Blakely, R.J., Jachens, R.C., Simpson, R.W., and Couch, R.W., 1985, Tectonic setting of the sourhern Cascade Range as interpreted from its magnetic and gravity fields: Geological Society of America Bulletin, v. 96, p. 43-48.

Borg, L.E., Brandon, A.D., Clynne, M.A., and Walker, R.J., 2000, Re-Os isotopic systematics of primitive lavas from the Lassen region of the Cascade arc, California: Earth and Planetary Science Letters, v. 177, p. 301-317.

Borg, L.E., Clynne, M.A., and Bullen, T.D., 1997, The Variable Role of Slab-derived Fluids in the Generation of a Suite of Primitive Calc-Alkaline Lavas from the Sourthernmost Cascades, California: The Canadian Mineralogist, v. 35, p. 425-452.

Burton, K.W., Abdelmouhcine, G., Jean-Louis, B., Allegre, C.J., Schiano, P., Clocchiatti, R., and Olivier, A., 2002, The compatibility of rhenium and osmium in natural olivine and their behavious during mantle melting and basalt genesis: Earth and Planetary Science Letters, v. 198, p. 63-76.

Clynne, M.A., and Borg, L.E., 1997, Olivine and Chromian Spinel in Primitive Calc-alkaline and Tholeiitic Lavas from the Southernmost Cascade Range, California: A Reflection of Relative Fertility of the Source: The Canadian Mineralogist, v. 35, p. 453-472.

Fuis, G.S., Zucca, J.J., Mooney, W.D., and Milkereit, B., 1987, A geologic interpretation of seismic-reflection results in northern California: Geological Society of America Bulletin, v. 98, p. 53-65.

Green, N.L., and Harry, D.L., 1999, On the relationship between subducted slab age and arc basalt petrogenesis, Cascadia subduction system, North America: Earth and Planetary Science Letters, v. 171, p. 367-381.

Griscom, A., 1980, Klamath Mountains province. In Oliver, H. (ed) Interpretation of the gravity map of California and its continental margin: California Division of Mines Bulletin, v. 205, p. 34-36.

Grove, T.L., Baker, M.B., Price, R.C., Parman, S.W., Elkins-Tanton, L.T., Chatterjee, N., and Müntener, O., 2005, Magnesian andesite and dacite lavas from Mt. Shasta, northern California: products of fractional crystallization of H_2O-rich mantle melts: Contributions to Mineralogy and Petrology, v. 148, p. 542-565.

Grove, T.L., Elkins-Tanton, L.T., Parman, S.W., Chatterjee, N., Müntener, O., and Gaetani, G.A., 2003, Fractionatal crystallization and mantle-melting controls on calc-alkaline differentiation trends: Contributions to Mineralogy and Petrology, v. 145, p. 515-533.

Grove, T.L., and Juster, T.C., 1989, Experimental investigations of low-Ca pyroxene stability and olivine-pyroxene-liquid equilibria at 1-atm in natural basaltic and andesitic liquids: Contributions to Mineralogy and Petrology, v. 103, p. 287-305.

Grove, T.L., Parman, S.W., Bowring, S.A., Price, R.C., and Baker, M.B., 2002, The role of an H_2O-rich fluid component in the generation of primitive basaltic andesites and andesites from the Mt. Shasta region, N California: Contributions to Mineralogy and Petrology, v. 142, p. 375-396.

Gruau, G., Bernard-Griffiths, J., Lécuyer, C., Henin, O., Macé, J., and Cannat, M., 1995, Extreme Nd isotopic variation in the Trinity Ophiolite Complex and the role of melt/rock reactions in the oceanic lithosphere: Contributions to Mineralogy and Petrology, v. 121, p. 337-350.

Harris, R.A., Iyer, H.M., and Dawson, P.B., 1991, Imaging the Juan de Fuca Plate beneath southern Oregon using teleseismic P wave residuals: Journal of Geophysical Research, v. 96, p. 19879-19889.

Hart, W.K., Carlson, R.W., and Shirey, S.B., 1997, Radiogenic Os in primitive basalts from the northwestern U.S.A.: Implications for petrogenesis: Earth and Planetary Science Letters, v. 150, p. 103-116.

Huebner, J.S., 1971, Buffering Techniques for Hydrostatic Systems at Elevated Pressures, *in* Ulmer, G.C., ed., Research Techniques for High Pressure and High Temperature: New York, Springer-Verlag, p. 123-177.

Ishizaka, K., and Carlson, R.W., 1983, Nd-Sr systematics of the Setouchi volcanic rocks, southwest Japan: Earth and Planetary Science Letters, v. 64, p. 327-340.

Jacobsen, S.B., Quick, J.E., and Wasserburg, G.J., 1984, A Nd and Sr isotopic study of the Trinity peridotite; implications for mantle evolution: Earth and Planetary Science Letters, v. 68, p. 361-378.

Johnson, D.M., Hooper, P.R., and Conrey, R.M., 1999, GeoAnalytical Lab, Washington State University: Advances in X-ray Analysis, v. 41, p. 843-867.

Kamenetsky, V.S., Crawford, A.J., Eggins, S.M., and Muehe, R., 1997, Phenocryst and melt inclusion chemistry of near-axis seamounts, Valu Fa Ridge, Lau Basin; insight into mantle wedge melting and the addition of subduction components: Earth and Planetary Science Letters, v. 151, p. 205-223.

Kay, R.W., 1978, Aleutian magnesian andesites: melts from subducted Pacific ocean crust: Journal of Volcanology and Geothermal Research, v. 4, p. 117-132.

Knaack, C., Cornelius, S., and Hooper, P.R., 1994, Trace element Analysis of rocks and minerals by ICP-MS: Open File Report, Department of Geology, Washington State University.

Kress, V.C., and Carmichael, I.S.E., 1991, The compressibility of silicate liquids containing Fe2O3 and the effect of composition, temperature, oxygen fugacity and pressure on their redox states: Contributions to Mineralogy and Petrology, v. 108, p. 82-92.

Medard, E., and Grove, T.L., 2008, The effect of H_2O on the olivine liquidus of basaltic melts: experiments and thermodynamic models: Contributions to Mineralogy and Petrology, v. 155, p. 417-432.

Medaris, L. G., 1975, Coexisting spinel and silicates in alpine peridotites of the granulite facies: Geochemica et Cosmochemica Acta, v. 39, p. 947-958.

Nier, A.O., 1950, A Redetermination of the Relative Abundances of the Isotopes of Carbon, Nitrogen, Oxygen, Argon, and Potassium: Physical Review, v. 77, p. 789-793.

Parkinson, I.J., Hawkesworth, C.J., and Cohen, A.S., 1998, Ancient mantle in a modern arc: Osmium isotopes in Izu-Bonin-Mariana forearc peridotites: Science, v. 281, p. 2011-2013.

Quick, J.E., 1981, Petrology and Petrogenesis of the Trinity Peridotite, an Upper Mantle Diapir in the Eastern Klamath Mountains, Northern California: Journal of Geophysical Research, v. 86, p. 11837-11863.

Ruscitto, D., and Wallace, P., 2008, Revisiting the compositions and volatile contents of olivine-hosted melt inclusions from the Mount Shasta region: EOS Trans., AGU, v. 89 (53), Fall Meet. Suppl., Abstract V13F-06.

Streck, M.J., Leeman, W.P., and Chesley, J., 2007, High-magnesian andesite from Mount Shasta: A product of magma mixing and contamination, not a primitive mantle melt: Geology, v. 35, p. 351-354.

Tatsumi, Y., and Ishizaka, K., 1982, Origin of high-magnesian andesites in the Setouchi volcanic belt, southwest Japan, I. Petrological and chemical characteristics: Earth and Planetary Science Letters, v. 60, p. 293-304.

Wilson, D., 1988, Tectonic history of the Juan de Fuca ridge over the last 40 million years: Journal of Geophysical Research, v. 93, p. 11863-11876.

Wood, B.J., and Turner, S.P., 2009, Origin of primitive high-Mg andesite: Constraints from natural examples and experiments: Earth and Planetary Science Letters, v. 283, p. 59-66.

Yogodzinski, G.M., Kay, R.W., Volynets, O.N., Koloskov, A.V., and Kay, S.M., 1995, Magnesian andesite in the western Aleutian Komandorsky region: implications for slab melting and processes in the mantel wedge: Geological Society of America Bulletin, v. 107, p. 505-519.

Zucca, J.J., Fuis, G.S., Milkereit, B., Mooney, W.D., and Catchings, R.D., 1986, Crustal structure of northeastern California: Journal of Geophysical Research, v. 91, p. 7359-7382.

Table 1. XRF Major and Trace Elements for PMAs of Mt. Shasta and Mt. Lassen

Location	SVR	SVR	SVR	SVR	SVR	SVR	SVR	SVR	SVR
Sample	85-41c	88-23	91-5a	07-27	07-28	09-4	09-5	09-7	09-8
Lat.	41° 34.03	n/a	41° 34.03	41° 34.73	41° 35.03	41° 35.21	41° 35.34	41° 34.03	41° 34.41
Long.	122° 07.91	n/a	122° 07.91	122° 10.41	122° 11.63	122° 11.75	122° 11.87	122° 07.91	122° 07.14
SiO2	57.17	56.28	58.09	56.60	57.14	57.38	56.46	57.37	56.28
TiO2	0.57	0.75	0.58	0.65	0.60	0.60	0.60	0.58	0.75
Al2O3	14.23	15.40	14.63	14.39	13.77	13.98	14.09	14.21	15.36
FeO*	5.49	6.12	5.66	5.87	5.79	5.91	5.81	5.62	6.25
MnO	0.10	0.12	n/a	0.11	0.11	0.11	0.11	0.11	0.12
MgO	8.95	7.64	8.73	8.60	10.03	9.91	9.77	9.34	7.84
CaO	8.11	9.05	8.14	8.66	8.31	8.23	8.22	8.09	9.06
Na2O	3.02	3.06	3.16	2.89	2.83	2.89	2.77	2.96	3.01
K2O	0.73	0.65	0.76	0.84	0.75	0.73	0.72	0.78	0.71
P2O5	0.13	0.18	0.15	0.16	0.15	0.15	0.14	0.13	0.18
Sum	98.50	99.24	99.90	98.78	99.47	99.89	98.70	99.19	99.55
Ni	125	44	125	81	141	140	139	132	51
Cr	581	348	581	493	698	694	698	655	355
Sc	23	25	n/a	26	25	24	25	24	27
V	160	190	n/a	176	165	163	162	158	185
Ba	173	224	173	225	206	212	202	191	223
Rb	14	10	14	16	14	15	12	15	13
Sr	759	906	759	842	794	780	778	741	885
Zr	84	110	84	104	93	93	93	89	110
Y	10	14	10	12	12	13	11	11	13
Nb	1.9	2.2	1.9	2.2	1.7	2.4	2.3	3.0	3.5
Ga	14	16	14	16	15	15	15	15	15
Cu	58	48	n/a	55	60	64	64	48	48
Zn	56	60	n/a	56	57	58	59	56	63
Pb	2	3	n/a	3	3	2	3	2	3
La	10	12	10	11	15	13	11	13	10
Ce	20	31	20	27	26	24	23	20	30
Th	2	2	n/a	1	2	1	2	1	2
Nd	13	16	n/a	16	13	12	13	12	15

Table 1. cont.

Location	LVC	LVC	LVC	LVC
Sample	06-1A	06-1C	06-2	06-3
Lat.	40° 43.75	40° 43.75	40° 43.80	40° 43.80
Long.	121° 50.25	121° 50.25	121° 50.45	121° 50.45
SiO_2	58.43	60.10	57.74	58.13
TiO2	0.51	0.49	0.56	0.56
Al2O3	15.79	14.91	15.72	15.78
FeO*	5.36	5.04	5.66	5.70
MnO	0.10	0.09	0.10	0.10
MgO	7.58	7.03	7.59	7.72
CaO	7.32	6.91	7.25	7.24
Na2O	3.23	3.09	3.37	3.33
K2O	0.77	0.80	0.92	0.89
P2O5	0.11	0.13	0.12	0.13
Sum	99.20	98.58	99.03	99.56
Ni	179	165	241	246
Cr	274	248	271	281
Sc	22	21	20	20
V	142	149	147	145
Ba	190	197	196	201
Rb	10	10	13	13
Sr	766	742	755	753
Zr	73	69	80	81
Y	10	10	12	11
Nb	1.8	1.6	3.1	3.5
Ga	17	17	16	17
Cu	44	45	62	50
Zn	67	63	70	70
Pb	5	4	4	3
La	5	6	9	10
Ce	12	16	17	16
Th	3	2	5	3
Nd	7	10	7	11

SVR: Shasta Volcanic Region, LVC: Lassen Volcanic Center. Latitude and Longitude are reported in degrees and minutes N and W respectively. All Fe reported as FeO*. Sample 95-1a was analyzed at the USGS facility in Menlo Park (see Grove et al., 2005).

Table 2. Select trace elements and REE analyzed by ICP-MS (ppm)

Sample	85-41C	88-23	07-27	07-28
La	10.19	13.56	12.78	11.44
Ce	22.76	30.57	28.77	25.87
Pr	3.04	4.05	3.83	3.43
Nd	12.24	16.71	15.74	13.89
Sm	2.60	3.44	3.13	2.87
Eu	0.83	1.09	0.99	0.92
Gd	2.35	3.05	2.77	2.53
Tb	0.35	0.47	0.42	0.38
Dy	2.02	2.72	2.42	2.19
Ho	0.39	0.54	0.48	0.43
Er	1.05	1.43	1.28	1.14
Tm	0.16	0.21	0.19	0.17
Yb	0.99	1.33	1.21	1.04
Lu	0.16	0.21	0.19	0.17
Ba	174	225	225	209
Th	1.94	2.21	2.37	2.20
Nb	2.32	3.10	2.83	2.58
Y	10.54	13.93	12.48	11.29
Hf	2.37	2.94	2.76	2.53
Ta	0.16	0.20	0.18	0.18
U	0.68	0.74	0.80	0.77
Pb	3.60	3.75	4.07	3.63
Rb	13.0	10.0	15.9	14.0
Cs	0.76	0.44	0.75	0.68
Sr	761	905	838	793
Sc	23.4	25.7	24.7	23.2
Zr	80	105	99	88

Table 3. Isotopic Compositions of Selected Lavas

Sample	82-94a	85-41c	85-44	07-27	07-28	83-46	83-58	89-12
Rock Type	PBA	PMA	PBA	PMA	PMA	Dacite	Dacite	Trinity Peridotite
$^{87}Sr / ^{86}Sr$	0.703653	0.702999	0.703799	0.703013	0.703003	0.703694	0.70286[a]	0.704503
$^{143}Nd / ^{144}Nd$	0.512901	0.512971	0.512875	0.5129759	0.5129749	0.512829	0.512952[a]	0.513708
εNd[b]	5.1	6.5	4.6	6.6	6.6	3.7	6.1	20.9
Os (ppt)	19.1	14.1	110.2	n/a	n/a	9.4	6.6	3897
$^{187}Os / ^{188}Os$	0.17531	0.16739	0.16102	n/a	n/a	0.18291	0.20983	0.12434

[a] Data from Grove et al. (2002)

[b] Using CHUR = 0.512638 of DePaolo (1988)

Table 4. Example Mineral Compositions from Mt. Shasta and Mt. Lassen PMAs of This Study

07-28

	SiO_2	TiO_2	Al_2O_3	Cr_2O_3	FeO	MnO	MgO	CaO	NiO	Total
1	41.53	0.00	0.01	0.08	6.09	0.12	51.77	0.09	0.30	99.99

Core composition of normally zoned, ~1 mm euhedral olivine phenocryst ($Fo_{93.8}$)

	SiO_2	TiO_2	Al_2O_3	Cr_2O_3	FeO	MnO	MgO	CaO	NiO	ZnO	Total
2	0.03	0.42	8.17	53.16	27.41	0.40	8.95	0.10	0.06	0.22	98.92

Euhedral spinel included in the olivine shown above (Cr# 80)

	SiO_2	TiO_2	Al_2O_3	Cr_2O_3	FeO	MnO	MgO	CaO	Na_2O	Total
3	53.50	0.22	1.64	1.00	3.52	0.13	18.55	21.40	0.17	100.12

Core composition of medium euhedral clinopyroxene phenocryst (Mg# 90)

07-27

	SiO_2	TiO_2	Al_2O_3	Cr_2O_3	FeO	MnO	MgO	CaO	NiO	Total
1	40.59	0.01	0.00	0.06	9.71	0.14	49.03	0.11	0.15	99.81

Core composition of normally zoned, ~1 mm euhedral olivine phenocryst ($Fo_{90.0}$)

	SiO_2	TiO_2	Al_2O_3	Cr_2O_3	FeO	MnO	MgO	CaO	NiO	Total
2	38.69	0.06	0.08	0.05	22.45	0.36	37.30	0.39	0.05	99.43

Rim composition of euhedral olivine phenocryst shown above ($Fo_{74.8}$)

85-41c

	SiO_2	TiO_2	Al_2O_3	Cr_2O_3	FeO	MnO	MgO	CaO	NiO	Total
1	41.62	0.00	0.02	0.08	5.80	0.05	51.72	0.11	0.23	99.64

Core composition of normally zoned, ~2 mm euhedral olivine phenocryst ($Fo_{94.1}$)

	SiO_2	TiO_2	Al_2O_3	Cr_2O_3	FeO	MnO	MgO	CaO	NiO	Total
2	56.93	0.04	1.53	1.30	3.90	0.06	34.72	1.41	0.05	99.95

Core composition of normally zoned, medium orthopyroxene phenocryst ($Mg\#_{94}$)

Table 4. cont.

85-41c cont.

	SiO_2	TiO_2	Al_2O_3	Cr_2O_3	FeO	MnO	MgO	CaO	Na_2O	Total
3	51.01	0.71	2.83	0.09	10.25	0.26	13.57	19.81	0.50	99.04

Core composition of reversely zoned, medium clinopyroxene phenocryst (Mg# 70)

	SiO_2	TiO_2	Al_2O_3	Cr_2O_3	FeO	MnO	MgO	CaO	Na_2O	Total
4	52.96	0.34	2.32	0.70	4.75	0.15	18.83	19.32	0.21	99.58

Rim composition of reversely zoned, medium clinopyroxene phenocryst shown above (Mg# 88)

85-41b

	SiO_2	TiO_2	Al_2O_3	Cr_2O_3	FeO	MnO	MgO	CaO	NiO	Total
1	40.75	0.04	0.00	0.08	6.08	0.08	51.50	0.11	0.37	99.01

Core composition of normally zoned, ~1 mm euhedral olivine phenocryst ($Fo_{93.8}$)

	SiO_2	TiO_2	Al_2O_3	Cr_2O_3	FeO	MnO	MgO	CaO	Na_2O	Total
2	54.72	0.15	1.38	0.91	3.36	0.10	19.04	21.01	0.34	101.01

Core composition of unzoned, medium euhedral clinopyroxene phenocryst (Mg# 91)

	SiO_2	TiO_2	Al_2O_3	Cr_2O_3	FeO	MnO	MgO	CaO	Na_2O	Total
3	53.62	0.31	1.13	0.04	19.76	0.36	24.45	1.63	0.04	101.34

Core composition of reversely zoned, large orthopyroxene phenocryst (Mg# 69)

	SiO_2	TiO_2	Al_2O_3	Cr_2O_3	FeO	MnO	MgO	CaO	Na_2O	
4	56.66	0.12	0.86	0.07	9.61	0.15	31.76	1.92	0.05	101.20

Middle zone composition of reversely zoned, large orthopyroxene phenocryst of #4 above (Mg# 85)

	SiO_2	TiO_2	Al_2O_3	Cr_2O_3	FeO	MnO	MgO	CaO	Na_2O	
5	57.71	0.07	0.95	0.67	4.73	0.07	35.71	1.19	0.00	101.10

Rim composition of reversely zoned, large orthopyroxene phenocryst of #4 and #5 above (Mg# 93)

Table 4. cont.

06-2

	SiO_2	TiO_2	Al_2O_3	Cr_2O_3	FeO	MnO	MgO	CaO	NiO	Total
1	40.19	0.00	0.00	0.00	9.20	0.10	50.28	0.07	0.74	100.57

Core composition of normally zoned, ~1 mm euhedral olivine phenocryst ($Fo_{90.7}$)

	SiO_2	TiO_2	Al_2O_3	Cr_2O_3	FeO	MnO	MgO	CaO	Na_2O	Total
2	53.50	0.09	2.11	0.28	4.37	0.15	17.18	22.50	0.23	100.41

Core composition of unzoned, medium euhedral clinopyroxene phenocryst (Mg# 88)

	SiO_2	TiO_2	Al_2O_3	Cr_2O_3	FeO	MnO	MgO	CaO	Na_2O	Total
3	48.75	0.47	4.70	0.05	11.10	0.30	13.11	20.10	0.43	99.01

Core composition of reversely zoned, medium clinopyroxene phenocryst (Mg# 68)

	SiO_2	TiO_2	Al_2O_3	Cr_2O_3	FeO	MnO	MgO	CaO	Na_2O	
4	52.54	0.24	2.01	0.93	4.26	0.13	17.14	21.61	0.30	99.17

Rim composition of reversely zoned, medium clinopyroxene phenocryst shown above (Mg# 88)

06-1

	SiO_2	TiO_2	Al_2O_3	Cr_2O_3	FeO	MnO	MgO	CaO	Na_2O	Total
1	52.76	0.12	0.93	0.06	8.47	0.65	14.56	22.08	0.33	99.96

Composition of coarse groundmass clinopyroxene (Mg# 75)

Table 5. Electron microprobe analyses of melt inclusions in 85-41b.

	SiO_2	TiO_2	Al_2O_3	Cr_2O_3	FeO	MnO	MgO	CaO	Na_2O	K_2O	P_2O_5	Sum	Mg#
1	63.53	0.69	15.62	0.24	3.06	0.09	4.35	6.24	4.29	1.63	0.25	97.39	0.72
2	61.35	0.95	14.77	0.03	6.17	0.08	3.47	7.85	4.85	0.19	0.27	99.57	0.50
3	70.27	1.20	10.14	0.01	5.12	0.07	2.96	6.08	3.66	0.19	0.29	99.39	0.51
4	66.22	0.74	17.24	0.03	3.27	0.04	0.80	5.97	5.17	0.22	0.29	99.09	0.30
5	65.80	0.39	16.68	0.00	4.18	0.06	1.79	4.94	5.85	0.22	0.09	100.61	0.43
6	69.18	0.36	14.68	0.05	4.61	0.05	0.38	3.68	4.45	2.37	0.20	96.78	0.13
7	68.97	0.79	13.87	0.04	6.52	0.06	0.28	1.96	4.38	2.83	0.28	100.52	0.07
8	69.02	0.75	13.65	0.08	6.80	0.07	0.67	1.96	4.04	2.80	0.17	98.75	0.15
9	63.88	0.73	19.73	0.02	2.60	0.04	1.05	4.44	5.10	1.86	0.55	99.03	0.42
10	60.74	0.64	17.10	0.06	5.74	0.04	2.36	7.52	5.04	0.47	0.29	95.36	0.42
11	66.94	0.55	16.00	0.03	6.49	0.04	0.41	3.44	4.16	1.74	0.20	100.4	0.10
12	63.62	0.32	20.69	0.05	3.50	0.08	0.51	4.77	4.61	1.79	0.06	99.02	0.21
13	59.22	0.57	17.44	0.04	3.95	0.06	4.79	9.04	3.97	0.72	0.21	99.46	0.68
14	61.27	0.50	17.47	0.05	4.20	0.06	4.32	6.60	4.55	0.78	0.19	98.48	0.65
15	63.88	0.73	19.73	0.02	2.60	0.04	1.05	4.44	5.10	1.86	0.55	96.96	0.42
16	60.74	0.64	17.10	0.06	5.74	0.04	2.36	7.52	5.04	0.47	0.29	101.45	0.42
17	60.24	0.47	16.81	0.04	4.20	0.11	4.80	8.22	4.15	0.81	0.15	99.77	0.67
18	59.36	0.30	17.64	0.00	4.06	0.09	7.54	6.02	4.50	0.38	0.10	97.39	0.77
19	63.53	0.69	15.62	0.24	3.06	0.09	4.35	6.24	4.29	1.63	0.25	97.99	0.72

All analyses are normalized to 100 %, but the original microprobe total is presented as the sum.
1-5, Melt inclusion in reacted opx in Fig. 1b, Mg# = 69.
6-13, Melt inclusions in pyroxenes,
6-9 Wo41, Mg# 69-71,
10-11 opx, Mg# = 88,
12-13, opx, Mg# = 67.5.
14-18, Melt inclusions in olivine.

Figure Captions

Figure 1. Map of the occurrences of PMA lavas at Mt. Shasta. Light grey region indicates extent of HAOT lavas, dark grey indicate regions of PMA lavas. Sample locations refer to samples in Table 1. Mapping based on unit designations and mapping of R. L. Christiansen (personal communication).

Figure 2. Characteristic mineral grains found in S17 PMA samples. A. Normally zoned high-Fo olivine from sample 85-41b of Baker et al. (1994). B. Complexly zoned opx with evolved core, reacted interior and primitive rim. Mineral analyses shown in Table 4.

Figure 3. Zoned clinopyroxene grain from sample 09-7 from the S17 cinder cone. The stages of zoning indicating mixing into primitive magmas and subsequent evolution followed by mixing into another primitive magma of a similar composition. See the text for further description of the zoning stages.

Figure 4. Compositions of spinels reported for the Trinity ultramafic body (Quick, 1981) and the PMAs of Mt. Shasta and Mt. Lassen. Data for Mt. Lassen PMAs is from Clynne and Borg (1997) and data for Mt. Shasta PMAs is from this study and Baker et al. (1994). Both Cr# and Mg# are in molar units. In the PMAs the spinels are mainly found as inclusions in olivine.

Figure 5. Major element variation diagrams for Mt. Shasta lavas from Table 1, Baker et al. (1994), and Grove et al. (2002, 2003, 2005) and melt inclusions compositions of Table 5. Also shown are liquid lines of descent for PMA 85-41c and PBA 85-44 of Grove et al. (2003). Light grey arrow indicates mixing trajectory of PMA samples from the lava flow identified in this study.

Figure 6. Olivine compositions from the PMA lavas of Mt. Shasta and Mt. Lassen. The analyses include multiple points from several grains to illustrate the continual normally zoned growth of the high-Fo olivines.

Figure 7. Sr and Nd isotopic compositions of Mt. Shasta lavas. Figure after Grove et al. (2003). Model 1 and Model 2 represent mixtures of dacite and basalts in the proportions of Model 1 and Model 2 of Streck et al. (2007).

Figure 8. Os concentrations and isotopic compositions for select Mt. Shasta lavas and sample of Trinity peridotite. Samples of Mt. Lassen lavas from Borg et al. (2000) are shown for comparison. See text for description of the melting model.

Figure 9. Pressure (GPa) of generation and melt H_2O (wt %) contents calculated for PMAs of the southern Cascades using the algorithm of Wood and Turner (2009). 07-28, this study, and 85-41c, taken from Baker et al. (1994) are from Mt. Shasta and LC86-1009, taken from Borg et al. (1997) is from Mt. Lassen.

Figure 1.

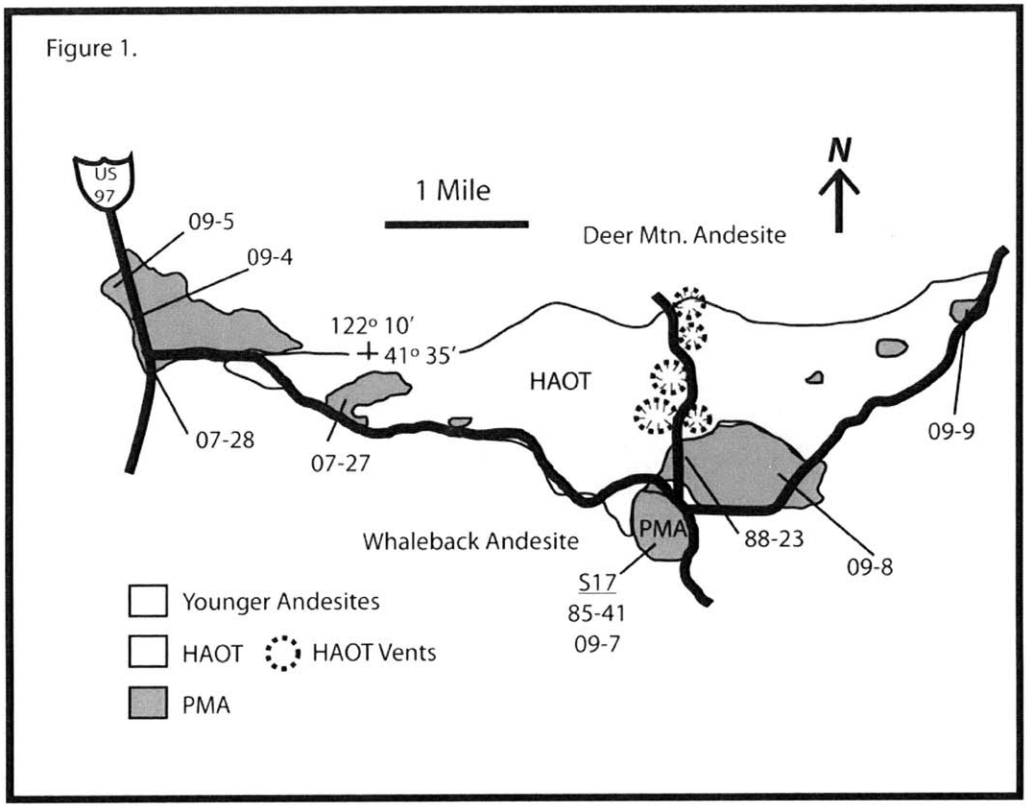
Figure 1.
US 97
1 Mile
N
09-5
09-4
Deer Mtn. Andesite
122° 10′
41° 35′
HAOT
07-28
07-27
09-9
Whaleback Andesite
PMA
88-23
09-8
S17
85-41
09-7
Younger Andesites
HAOT
HAOT Vents
PMA

Figure 2.

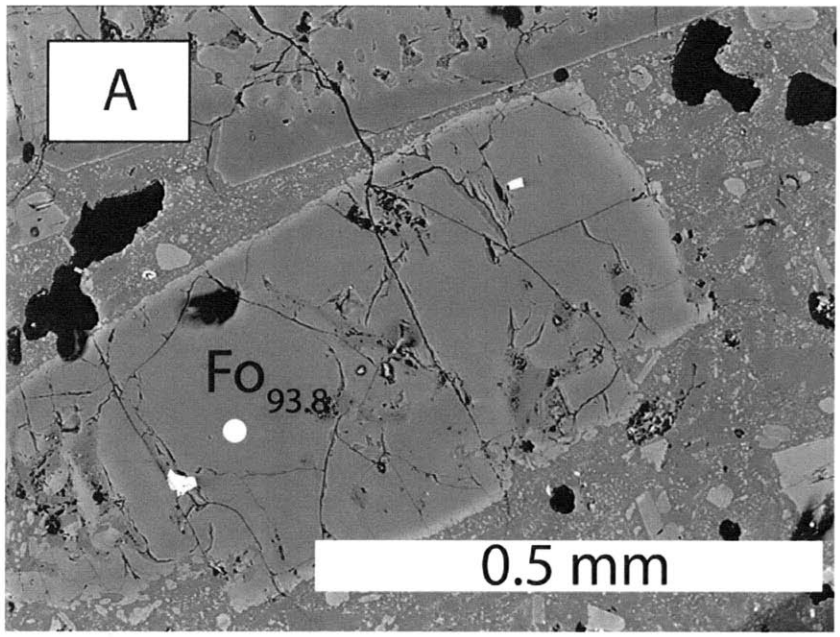

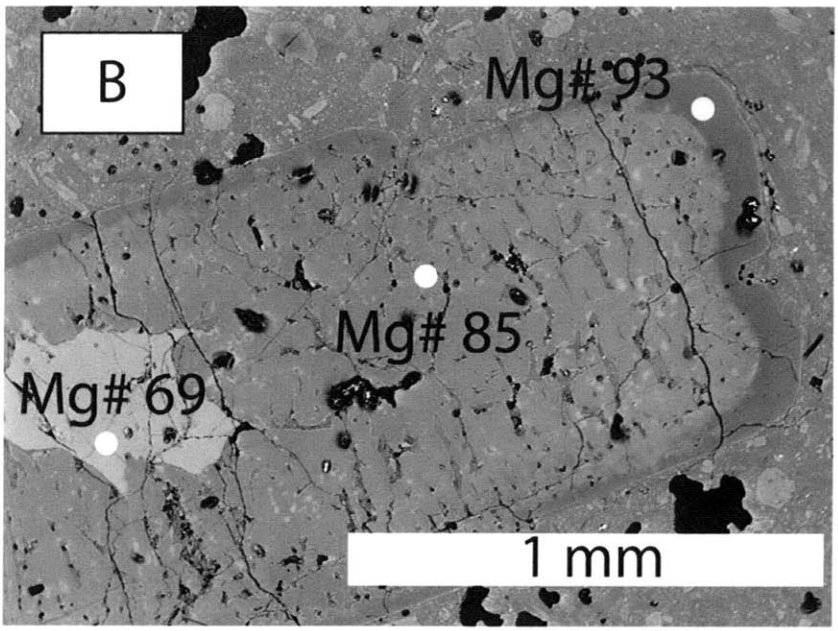

Figure 3.

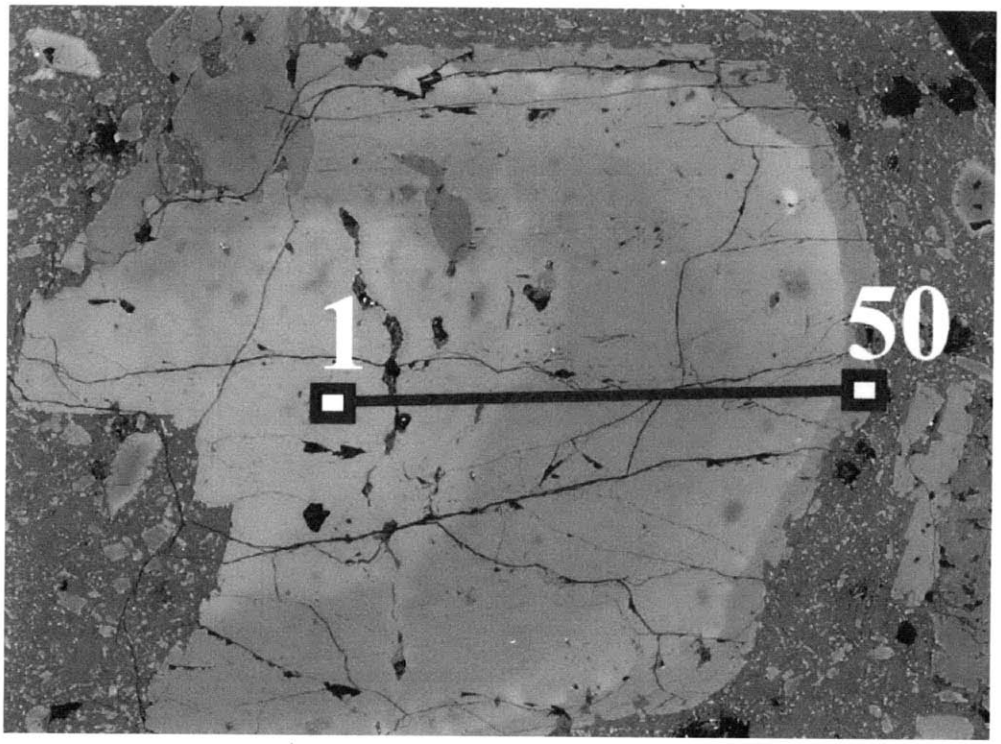
1
50

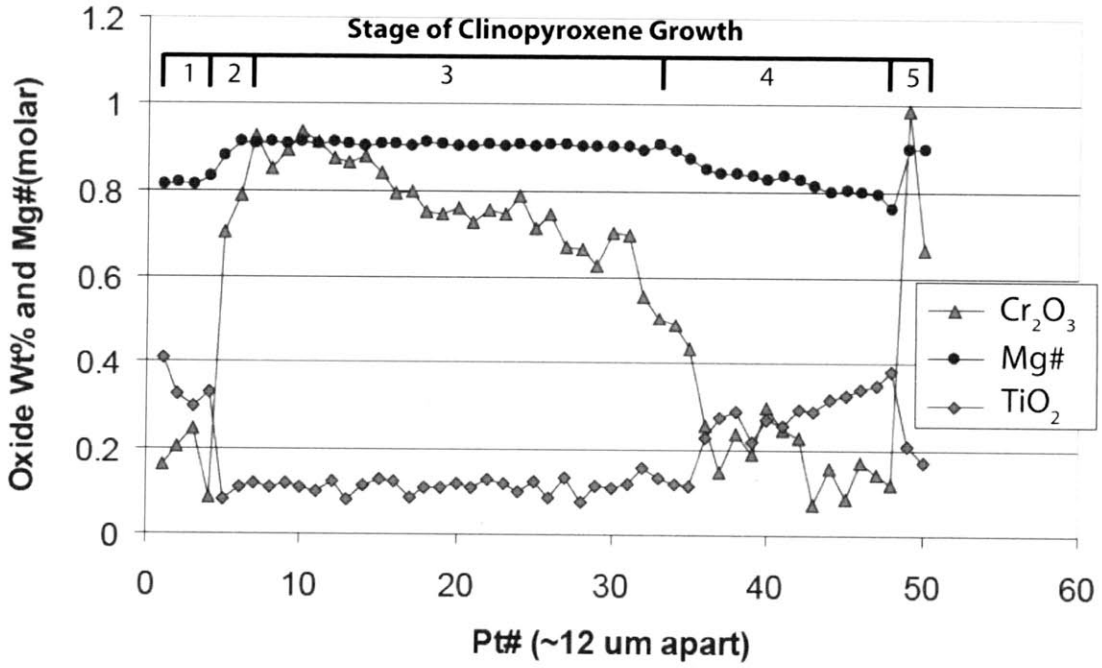
Stage of Clinopyroxene Growth
1
2
3
4
5
Oxide Wt% and Mg#(molar)
1.2
1
0.8
0.6
0.4
0.2
0
0
10
20
30
40
50
60
Pt# (~12 um apart)
Cr2O3
Mg#
TiO2

Figure 4.

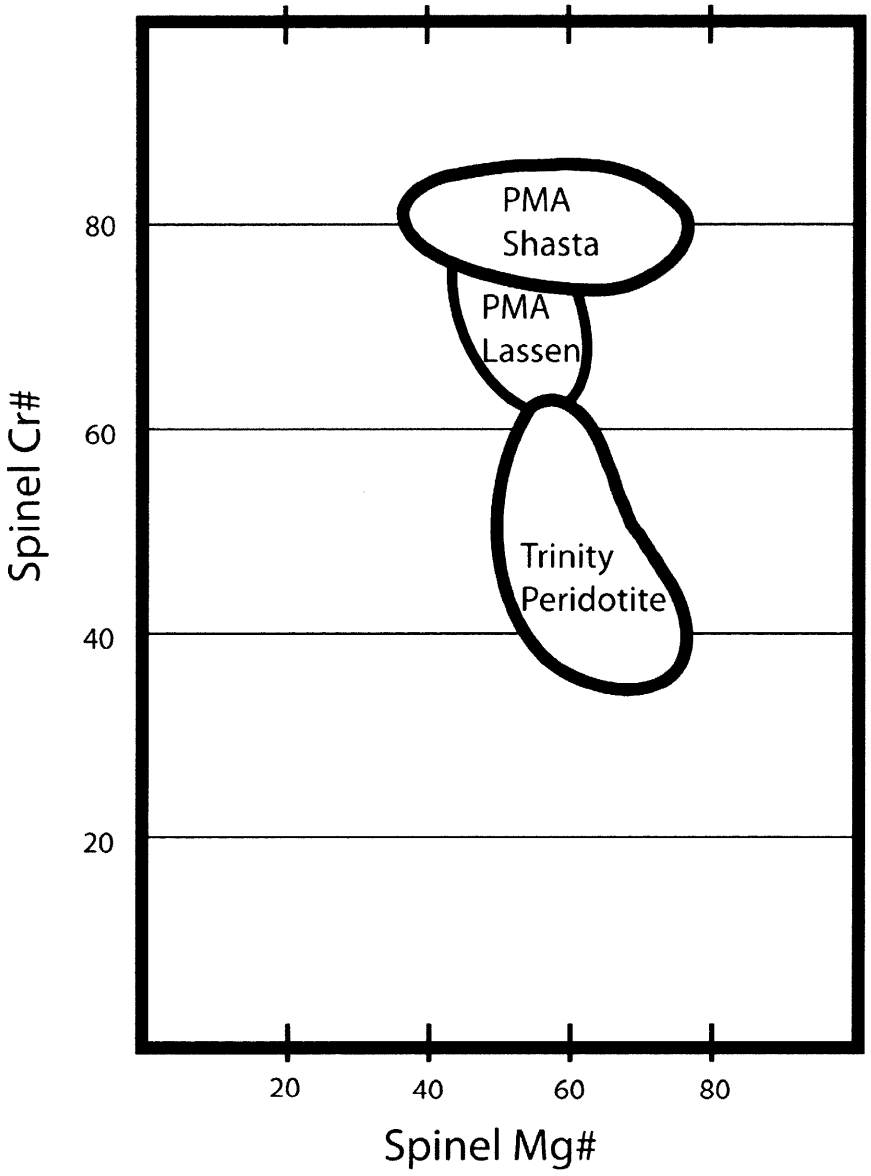
PMA
Shasta
PMA
Lassen
Trinity
Peridotite
80
60
40
20
Spinel Cr#
20
40
60
80
Spinel Mg#

Figure 5.

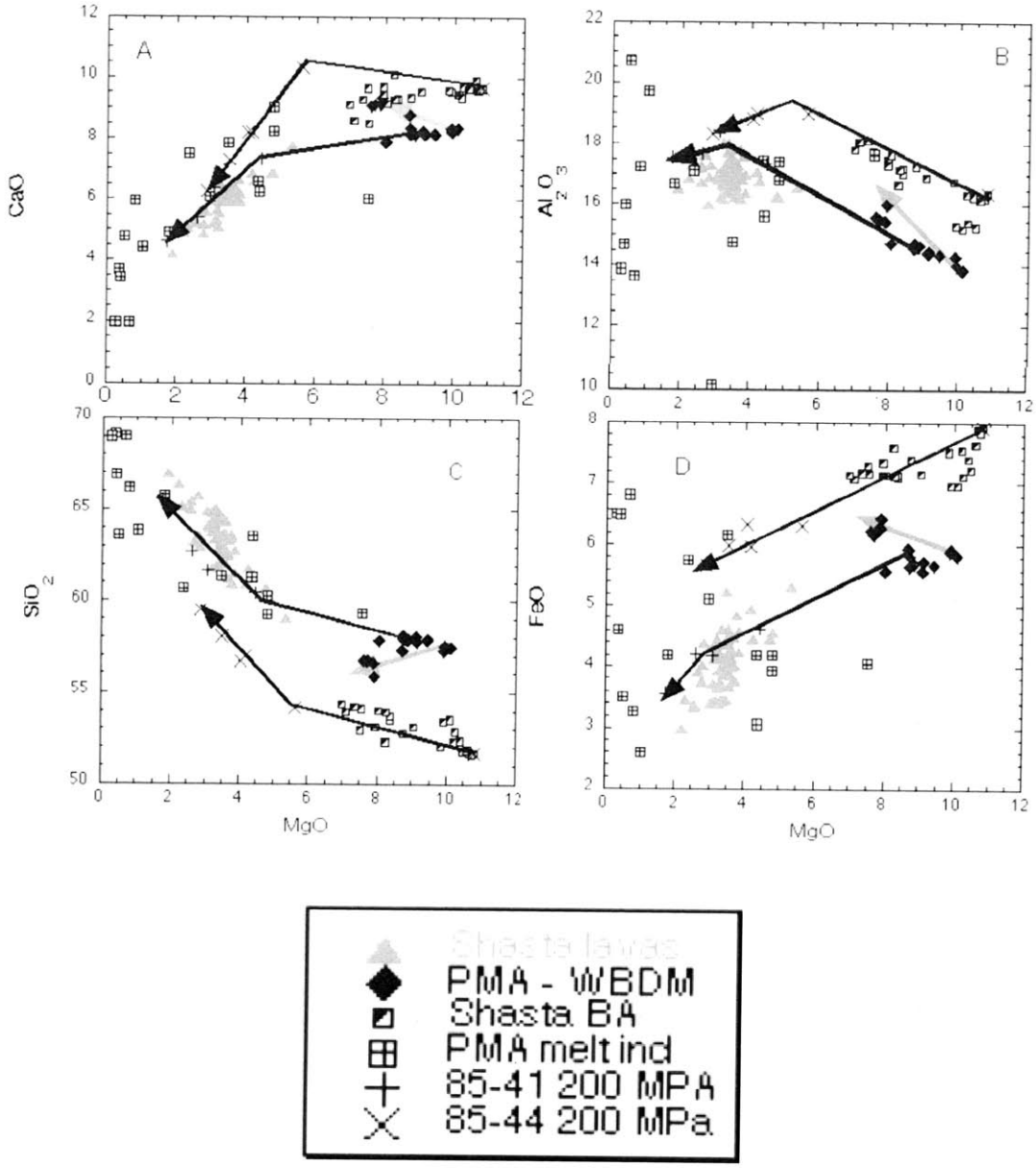
A
B
C
D
CaO
Al2O3
SiO2
FeO
MgO
MgO
Shasta lavas
PMA - WBDM
Shasta BA
PMA melt ind
85-41 200 MPA
85-44 200 MPa

Figure 6.

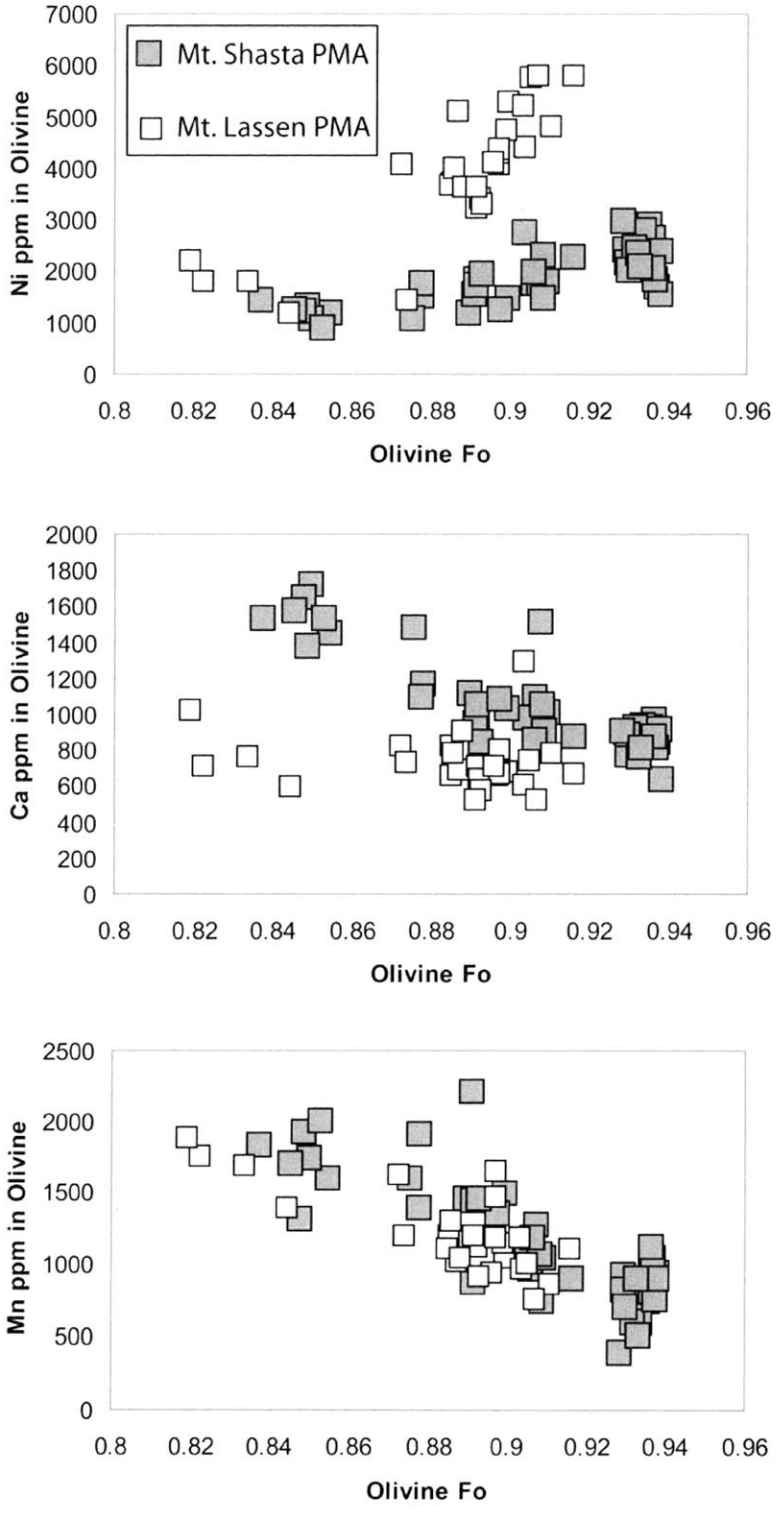
Mt. Shasta PMA
Mt. Lassen PMA
Ni ppm in Olivine
Ca ppm in Olivine
Mn ppm in Olivine
Olivine Fo
0.8
0.82
0.84
0.86
0.88
0.9
0.92
0.94
0.96

Figure 7.

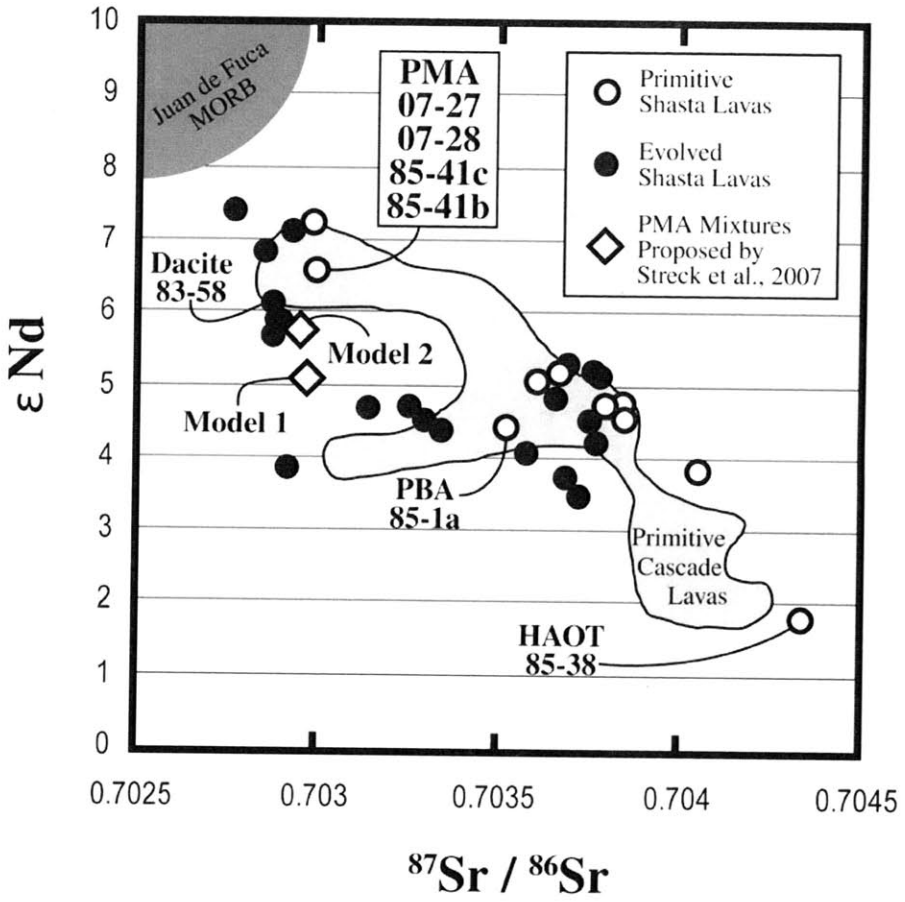
Juan de Fuca MORB
PMA
07-27
07-28
85-41c
85-41b
Primitive Shasta Lavas
Evolved Shasta Lavas
PMA Mixtures Proposed by Streck et al., 2007
Dacite 83-58
Model 2
Model 1
PBA 85-1a
Primitive Cascade Lavas
HAOT 85-38
ε Nd
87Sr / 86Sr
10
9
8
7
6
5
4
3
2
1
0
0.7025
0.703
0.7035
0.704
0.7045

Figure 8.

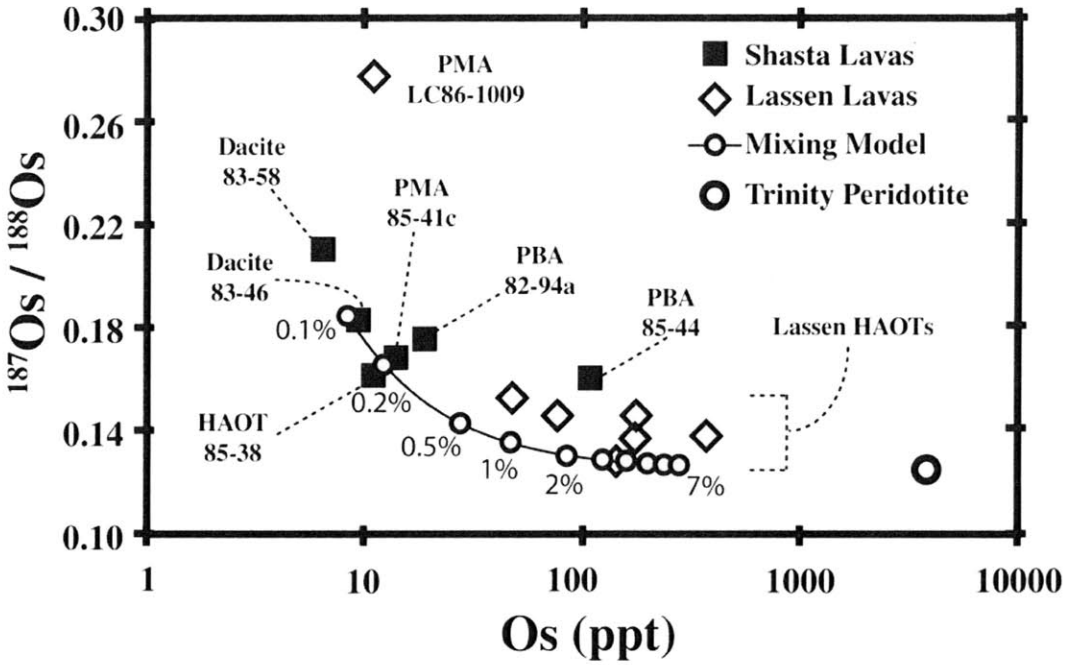
0.30
0.26
0.22
0.18
0.14
0.10
^{187}Os / ^{188}Os
1
10
100
1000
10000
Os (ppt)
PMA
LC86-1009
Shasta Lavas
Lassen Lavas
Mixing Model
Trinity Peridotite
Dacite
83-58
PMA
85-41c
Dacite
83-46
PBA
82-94a
PBA
85-44
Lassen HAOTs
0.1%
0.2%
0.5%
1%
2%
7%
HAOT
85-38

Figure 9.

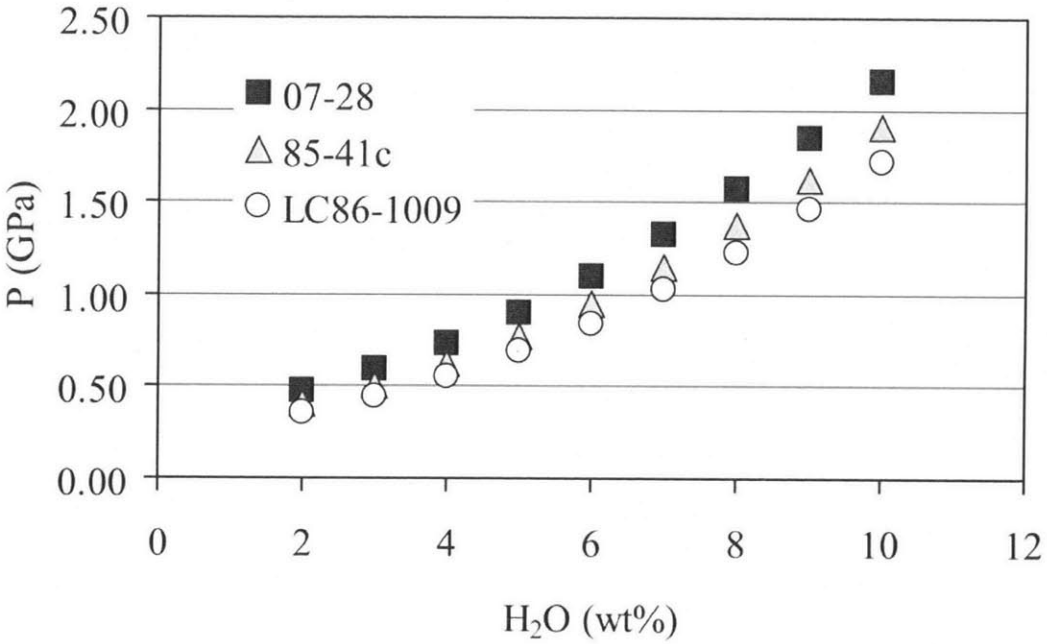
2.50
2.00
1.50
1.00
0.50
0.00
P (GPa)
07-28
85-41c
LC86-1009
0
2
4
6
8
10
12
H2O (wt%)

Chapter 4: AuPdFe Ternary Solution Model and Applications to Understanding the fO_2 of Hydrous, High-Pressure Experiments

Abstract

This study provides an experimental calibration of the equilibrium constant for AuPdFe alloys with Fe-bearing silicate melts. The ideal metal capsules for H_2O-bearing experiments is pure Au, because of its slow hydrogen diffusivity. However, above the melting point of Au, other materials must be used. The solution to this problem is to use AuPd alloy capsules. However, under most relevant fO_2 conditions this alloy absorbs Fe from the coexisting silicate melt, thus changing the bulk composition of the experimental charge. This study combines previous work on the Au-Pd, Pd-Fe, and Au-Fe binary systems to develop a ternary thermodynamic solution model for AuPdFe. This solution model is used with experiments to calculate an equilibrium reaction coefficient for the $FeO_{melt} \rightarrow Fe_{alloy} + \frac{1}{2} O_2$ exchange reaction. Using a non-ideal ternary solution model, the fO_2 conditions of hydrous, piston cylinder experiments can be estimated by analyzing the sample capsule alloy and the coexisting liquid composition.

Introduction

Understanding the role of volatiles in subduction zone magmas is an outstanding problem in igneous petrology. Paramount to our understanding of these systems is a full understanding of how volatiles affect magma generation and evolution. Estimates of pre-eruptive volatile contents using phase equilibria (e.g. Sisson and Grove 1993) or melt inclusions (e.g. Anderson 1974) can provide insight magmatic processes, however effects of these volatiles on the melting reactions and phase chemistry requires extensive experimental petrologic investigation. The use of volatiles in experiments requires changes to traditional methodology to minimize reaction with the experimental capsules and to maintain a constant bulk composition, including volatile composition.

Advances have been made in the experimental methods used in H_2O rich experiments since early studies (e.g. Shaw 1963). These early studies often used simplified systems that didn't include minor elements or Fe due to the added difficulty of maintaining constant bulk compositions, or these experiments used Au capsules, which limited the temperature range. Modern hydrous experiments using natural rock compositions can be performed above the melting point of Au by using AuPd alloy capsules, however this can create problems with loss of Fe from the silicate melt to the capsule alloy:

$$FeO_{melt} \leftrightarrow Fe_{alloy} + \tfrac{1}{2}(O_2) \quad (1)$$

Using Au capsules can minimize loss of H_2O from experimental charges by limiting the diffusive loss of hydrogen, and when used under fO_2 conditions typically encountered by terrestrial magmas, at or above the quartz-fayalite-magnetite (QFM) buffer, it has minimal exchange of Fe with the melts. However, the use of Au capsules is limited by the relatively low melting point of the capsule material (1064°C, IPTS-68, at 1-atm, with a P-T slope of ~ 58°C/GPa; Akella and Kennedy, 1971), which is too low for many melting and crystallization experiments performed on primitive mafic or ultramafic magmas. For these higher temperature experiments, the use of AuPd alloy capsules increases the upper temperature limit that can be achieved and can help maintain the volatile contents of the experimental charge, but the addition of

Pd to the alloy increases the solubility of Fe in the alloy. This can result in Fe-loss to the capsule, which changes the bulk composition of the experimental charge and alters the phase equilibria.

Researchers currently use a variety of techniques to minimize the Fe-exchange in AuPd alloy capsule experiments. One method is to equilibrate the AuPd alloy capsules with an Fe bearing silicate melt, whereby Fe is absorbed into the alloy capsule (e.g. Gaetani and Grove 1998). A second method is to use a second capsule to isolate the experimental charge from coming in contact with the alloy capsule, a commonly used technique for running experiments in Pt capsules (e.g. Takahashi and Kushiro 1983). A third method is to enclose the sealed sample capsule inside a second capsule also filled with the same starting material in an attempt to supply enough starting material to saturate the alloy capsule and maintain a relatively constant bulk composition at the same time (e.g. Kägi et al. 2005). A fourth method is to perform experiments at very oxidizing conditions, which reduces the amount of Fe-loss to the AuPd capsules due to the exchange reaction's dependence on fO_2 (Kawamoto and Hirose 1994). The use of a secondary capsule of graphite creates another reaction problem since it can react with the hydrous melt to change the volatile speciation. The arbitrary saturation of alloy capsules with Fe helps to eliminate the Fe-loss problem, however it can add its own problem when the alloy contains more Fe than the equilibrium would dictate, which causes the capsule to add Fe to the experimental melt. Using large volumes of starting material in a double capsule can be limited by the amount of space available in a piston cylinder experiment and may also lead to significantly larger thermal gradients due to the increased volume of the capsule assembly.

The ideal resolution to the problem of Fe exchange between melt and the AuPd alloys is to model the thermodynamics of the ternary AuPdFe system and experimentally calibrate an equilibrium constant for the Fe-exchange reaction between silicate melt and AuPdFe alloy. This is the focus of the current study, where we use existing binary solution models for the alloys and develop a ternary solution model. The model is then used in conjunction with experiments that equilibrate AuPdFe alloys with natural basaltic and andesitic melts to develop an equilibrium constant for the Fe exchange as a function of fO_2, temperature, and melt composition. The resulting equilibrium constants are then used in conjunction with

the equilibrium constants for the same reaction in the PtFe alloy – silicate melt system to constrain the misfit-parameter for the difference between the PtFe system and the AuPdFe system. Under equilibrium conditions, this solution model will provide estimates of fO_2 for AuPdFe alloy capsule experiments directly, from measurements of the alloy and coexisting melt compositions.

Development of the Ternary Solution Model

To develop a ternary solution model for the AuPdFe system, excess molar Gibbs free energy values, calculated for the three binary systems Au-Pd, Pd-Fe, and Au-Fe, are combined into a ternary solution. The binary excess parameters are taken from two studies: Borisov and Palme (2000) and Tomiska (1990), described below.

The behavior of the AuPd binary alloy system was summarized and reevaluated in the study of Tomiska (1990). The authors used computer-aided Knudsen cell mass spectrometry to investigate the excess Gibbs energies of solid AuPd alloys. Their ion-current intensity data were converted to molar thermodynamic variables by applying the Thermodynamic Adapted Power series (T.A.P) to their "Enlarged Algebraic Intensity Ratio" method. This allowed the authors to model their measured intensity ratios to determine excess molar enthalpy and entropy of different alloy compositions at a constant temperature (Table 2 and 3 of Tomiska, 1990). For the purpose of this study, the data on excess enthalpy and entropy are refit, and asymmetric Margules parameters for entropy and enthalpy are extracted.

The study of Borisov and Palme (2000) investigated the solubility of noble metals in Fe-bearing melts. As a consequence of the study the investigators modeled the two solid alloy systems, Au-Fe and Pd-Fe, as asymmetric solid solutions as per the method of Thompson (1967). This method uses asymmetric Margules parameters for excess enthalpy and entropy like that described for the AuPd binary above.

The temperature dependent excess Gibbs free energy parameters for the three binary systems are combined into an asymmetric Margules solution model, where the ternary Margules parameter (W_{AuFePd}) is set equal to zero. The form of the equation follows that of Fuhrman and Lindsley (1988):

$$RT\ln\gamma_{Fe} = \begin{bmatrix} W_{AuFe}[(2X_{Au}X_{Fe})\cdot(1-X_{Fe}) + (X_{Au}X_{Pd})\cdot(\tfrac{1}{2}-X_{Fe})] + \\ W_{FeAu}[(X_{Au})^2\cdot(1-2X_{Fe}) + (X_{Au}X_{Pd})\cdot(\tfrac{1}{2}-X_{Fe})] + \\ W_{PdFe}[(2X_{Pd}X_{Fe})\cdot(1-X_{Fe}) + (X_{Au}X_{Pd})\cdot(\tfrac{1}{2}-X_{Fe})] + \\ W_{FePd}[(X_{Pd})^2\cdot(1-2X_{Fe}) + (X_{Au}X_{Pd})\cdot(\tfrac{1}{2}-X_{Fe})] + \\ W_{AuPd}[(X_{Au}X_{Pd})\cdot(\tfrac{1}{2}-X_{Fe}-2X_{Pd})] + \\ W_{PdAu}[(X_{Au}X_{Pd})\cdot(\tfrac{1}{2}-X_{Fe}-2X_{Au})] + \\ W_{AuPdFe}[(X_{Au}X_{Pd})\cdot(1-2X_{Fe})] \end{bmatrix} \quad (2)$$

The solution model can be used to compute the thermodynamic activity of Fe, Au, or Pd in an alloy sample based on the measured alloy composition and the temperature of equilibration. In particular the a_{Fe} for an alloy in an experiment can be calculated and used in the development of an equilibrium constant for the exchange of Fe between the alloy and melt.

Experimental Methods and Analysis

All of the experiments for this study were performed at the MIT Experimental Petrology Laboratory. Powders of natural primitive basalts and basaltic andesites were ground by hand in ethanol using an agate mortar and pestle to produce homogenous, fine grained starting materials. An exception was B1104, which used a hydrous, partially glassed (glass + crystals) starting material. For the alloy-melt calibration experiments, the powders were packed into open-topped capsules made from the AuPd alloys. The alloy and silicate charges were allowed to equilibrate at 0.0001GPa (1 atm) in a vertical DelTech gas-mixing furnace. These experiments are hereby referred to as the low pressure experiments. Mixtures of H_2 and CO_2 were streamed through the furnace to achieve desired fO_2 conditions, which were monitored using Ca-doped ZrO_2 oxygen cells. The temperature of the samples was measured by a Type S (Pt-

$Pt_{90}Rh_{10}$ alloy) thermocouple, calibrated to the melting point of NaCl, Au, and Pd, and is accurate to ±2°C. The thermocouple, sample capsules, and oxygen cell were all held at the same height within the furnace to maximize accuracy for each run, and long run times (Table 1) were used to allow the melt to equilibrate with the alloy capsule. The low pressure experiments were quenched by dropping them into water, quenching the melt to an anhydrous glass.

Experiments performed at high-pressure were run in a ½" Boyd-England style end-loaded piston cylinder apparatus (Boyd and England 1960). The experiments were performed using a graphite capsule or a capsule fabricated from AuPd alloy tubing. The graphite capsules were packed with powdered starting material, into which a small AuPd bead was placed to act as a monitor of the experimental fO_2, and then topped by a lid before placing inside a dense alumina ring. For experiment B1104 the graphite capsule did not contain a AuPd bead but was encased in a AuPd jacket similar to Pt-jacketed graphite capsules of the Medard et al. (2008) study, however the AuPd breached the capsule and made contact with the melt allowing for the solution of Fe into the alloy. The AuPd alloy capsules had one end of the capsule triple crimped, welded and flattened and the other was triple crimped and welded after the powdered starting material and H_2O were added. The capsule was then formed to be approximately the same size and shape as the graphite capsules before being placed inside an unfired pyrophyllite ring, instead of alumina. Experiment B1153 utilized a crushable MgO ring instead of pyrophyllite to investigate the effect the surrounding material has on the fO_2 of the charge. Both of the capsule types were carefully measured and centered within a straight-walled 1.25" graphite resistance furnace by using crushable MgO spacers (see Medard et al. 2008 for experimental assembly diagram and pressurization procedure). For the graphite capsule runs B1099 and C405 the graphite capsules, with starting materials inside, and the MgO spacers were dried in an oven at 120°C for greater than 24 hrs, removed from the oven and assembled immediately prior to performing the experiment. The furnace assembly was then placed inside a sintered witherite ($BaCO_3$) pressure cell. The experimental temperature was measured a fixed distance above the center of the capsule using a Type D ($W_{97}Re_3$,$W_{75}Re_{25}$) thermocouple threaded through a 4-holed alumina ceramic sleeve. The distance between the sample capsule and the

thermocouple was held constant for each run and the temperature correction has been calibrated by using off-set thermocouples and spinel growth kinetics (Medard et al. 2008). Temperature gradients across the sample capsules in this run assembly are ~5°C (Medard et al. 2008). The alloy capsules were packed with a hydrous mixture of synthetic oxides recreating the composition of a basaltic andesite (Barr et al. 2007), and welded shut. The graphite capsules were packed with anhydrous rock powder, dried at 120°C for >24 hrs, into which a small AuPd alloy bead was placed. The capsule was topped with a graphite lid before placing in the run assembly to ensure isolation of the melt. One experiment shown in Table 2, ComW-1, is from the study of Barr et al. (2009), and was performed under H_2O-saturated conditions, at 0.2 GPa inside an externally-heated pressure vessel. The experiment utilized the double capsule technique to buffer the fO_2 at the Ni-NiO buffer. See Barr et al. (2009) for further discussion of the experimental procedure.

Compositions of the alloys and glasses were analyzed on a 5 spectrometer JEOL 733 electron microprobe at the electron microprobe facility at MIT. Natural and synthetic primary and secondary standards were used, and the CITZAF online data correction package was used for all analyses (Armstrong, 1995). Pure Au, Pd, and Fe were used as standards for the metal. The Fe standard was checked against freshly polished Fe metal standard to ensure that no oxide interferences occurred. Background levels for Au, Pd, and Fe were analyzed on each alloy to limit matrix interferences produced by alloys of varying Fe content. The beam size was set to ~2um to allow analyses of the alloy nearest the contact with the melt. Analyses were performed with a 15kV accelerating voltage and a beam current of 10nA. All glasses analyzed in this study used a defocused beam (~10um), 10nA beam current and 15kV accelerating voltage as per the routine analytical procedure of the facility. Care was taken to bring the experiments to equilibrium by allowing sufficient run times, which produced homogenous alloys and silicate melts.

Experimental Results

The glass and alloy analyses for the high and low pressure experiments of this study are presented in Tables 1 and 2. The low pressure experiments range in composition from basalt through andesite, with SiO_2 contents from 47.8 wt% to 60.7 wt%. The FeO contents of these experiments also cover a wide range, from 2.21 wt% to 7.89 wt%, with Mg#'s ranging from 0.65 to 0.89. The temperature range of the low pressure experiments ranges from 1158°C to 1300°C. The Fe contents of the alloys exhibit a strong fO_2 and temperature dependence. Two experiments at 1235°C, performed at log fO_2 values from -11.2 and -5.5, show a range in X_{Fe}^{alloy} from 13.1 to 8.3, respectively. These two experiments have liquid FeO contents of 2.55 wt% and 7.18 wt% respectively, exhibiting the opposite effect as is to be expected whereby the greater melt FeO should be in equilibrium with the higher X_{Fe}^{alloy}. Two other experiments at similar log fO_2 values, -9.1 and -9.2, but different temperatures, 1250°C and 1180°C respectively, show a variation in X_{Fe}^{alloy} from 4.1 mol% to 2.4 mol% respectively. The liquid FeO contents varied from 4.5 wt% to 7.4 wt%. Both results illustrate that changing the FeO content of the liquid has a smaller influence than changing the fO_2 of the experiment. The high pressure experiments fall within the range of the low-pressure experiments in terms of melt FeO wt% (except B1123; 2.03 wt% and B1153; 10.15 wt%), temperature (except B1123; 1100°C), and X_{Fe}^{alloy} (except B1104; 18.26 mol% Fe). The log fO_2 values for the high pressure experiments shown in Table 3 are calculated as described later in this manuscript.

The alloy compositions used in the experiments of this study began as either $Au_{80}Pd_{20}$ or $Au_{90}Pd_{10}$, by weight. The variation in alloy composition, as a function of the X_{Fe}^{alloy} is shown in Figure 1. The data show that the alloy compositions retain their original Au:Pd ratio even with significantly high Fe contents, displaying the similarities between the solubility of Au and Pd in silicate melts.

Calculating the Silicate-Alloy Equilibrium Constant

Calculation of the equilibrium reaction coefficient, K, for exchange of Fe between the alloy and melt:

$$K = \frac{a_{FeO}^{melt}}{a_{Fe}^{alloy} \times \sqrt{f_{O_2}}} \quad (4)$$

Requires measurements of fO_2, a_{Fe}^{alloy} and a_{FeO}^{melt}, so only the low-pressure (fO_2 buffered) experiments are used in the following calculations. In the experiments of this study, the fO_2 was controlled by equilibrating the experiments in a mixture of gases, verified by direct measurement with an oxygen sensor as described above. For the purpose of this study, the a_{FeO}^{melt} has been set equal to the X_{FeO}^{melt} as determined by the algorithm of Sack et al. (1980) or Kress and Carmichael (1991), so as to remain comparable to the models of Grove (1981) and Medard et al. (2008) respectively. This and other methods for the calculation of a_{FeO}^{melt} were discussed in Grove (1981) and Medard et al (2008), but the conclusions of those studies were that the methods of Sack et al. (1980) and Kress and Carmichael (1991) produced the best fit to the thermodynamic models. As discussed in Medard et al. (2008), this formulation method assumes a constant γ_{FeO} for the melts (Holzheid et al. 1997). To determine the thermodynamic activity of Fe in the AuPdFe alloy, the concentrations of the three elements were analyzed and along with temperature, were inputs into the alloy solution model outlined above. The resulting equilibrium constants are shown in Figure 2. A linear fit to the data returns a correlation coefficient of $R^2 = 0.98$ when using either Sack et al. (1980) or Kress and Carmichael (1991). Compared to the calculated equilibrium constants determined by Grove (1981) and Medard et al. (2008) for the PtFe binary system, the values determined in this study are distinctly different (Figure 2). Because the solutions to Eq. 4 determined in this study utilize the same methods employed by both of the previous studies of the PtFe system, including the same experimental laboratory, the discrepancy appears to be in the formulation of the solution models for the two alloy systems. Kessel et al. (2001) discusses problems with previous PtFe solution models, such as the one employed by the Grove (1981) study, however the results of the Medard

et al. (2008) investigation employed the solution model developed in that earlier review by Kessel et al. (2001). The discrepancy seen in the equilibrium constants could be from short comings of the AuPdFe solution model (e.g. ternary excess term equal to zero), however errors in the determinations of the binary excess Gibbs free energy parameters for the three binary systems of the AuPdFe system or for the parameters in the PtFe binary system (or in both solution models) could also lead to an offset of the values. The exchange reaction used in this study is the same reaction modeled in the studies of the PtFe system by Grove (1981) and Medard et al. (2008), and since Au, Pd, and Pt all share the same crystal structure, although different than that of Fe, direct comparison of the alloy models should be possible. One way to bring agreement to the systems is to calculate a misfit parameter, Δ_{misfit}, that can be added to the solution model (Eq. 2) to bring agreement to the K values for the Fe-exchange reaction calculated from PtFe and the AuPdFe solution models.

Using the PtFe Alloy Model to Calculate a Misfit Parameter

One way to calculate the misfit parameter for the AuPdFe alloy solution model is to assume that this term can account for the entire difference between the two alloy models. The misfit parameter, Δ_{misfit}, is formulated so that the value of K produced by the use of the AuPdFe solution model matches that of the value of K calculated from the fits to PtFe solution models, and can thus be added directly to the solution model of Eq. 2. The Δ_{misfit} can be calculated for each individual experiment as if it were an additional excess free energy term:

$$\Delta_{misfit} = RT(\ln K_{PtFe} - \ln K_{AuPdFe}) \quad (5)$$

Since Δ_{misfit} is calculated for each experiment individually, all of the parameters for the calculation of K are the same except for the formulation of the solution model.

This study performed the calculation of Δ_{misfit} utilizing the results of Grove (1981) and Medard et al. (2008) for the PtFe alloy model inputs into Eq. 5. The calculated misfit terms can then be linearly regressed versus 1000/T, yielding a temperature dependent equation for Δ_{misfit}, which is used in the final

formulation of the solution model. This final solution model is then used to recalculate all of the experiments in the original calibration set for the exchange equilibrium between melt and AuPdFe alloys. The final calculated values are shown in Figure 2 along with a least squares regression line to these new values. The fit to the recalculated data, lnK vs. 1000/T, is $R^2 = 0.95$ for Model 1 (Δ_{misfit} calculated using the results of Grove 1981) and $R^2 = 0.96$ for Model 2 (Δ_{misfit} calculated using the results Medard et al. 2008).

Determining the fO_2 for Unbuffered Graphite Capsule and AuPd Alloy Capsule Piston Cylinder Experiments

High pressure experiments performed in a piston cylinder apparatus can only accommodate small volumes of silicate material in order to limit pressure and temperature gradients over the volume of the sample capsules. For many experimental setups this precludes the inclusion of a separate capsule of oxygen buffering material. This allows piston cylinder experiments to equilibrate with the ambient fO_2 of the experimental run assembly, or the fO_2 is set by the capsule material. The study of Medard et al. (2008) illustrated the reducing effect of graphite capsules in barium carbonate pressure assemblies, drawing the fO_2 of more oxidized experimental charges to near that of the CCO buffer. The study by Medard et al. (2008) examined experiments performed in Pt-jacketed graphite capsules, and they speculate that the Pt-jacket might affect the buffering capacity of the capsule, due to the inhibition of gaseous diffusion by the Pt outer capsule. This suggests that unjacketed graphite capsules might not exhibit the same buffering characteristics. Those researchers pointed out, however, that a single experiment performed in a non-jacketed graphite capsule agreed well with their Pt-jacketed data, leaving the effect of the Pt outer capsule open to discussion. Also, because Pt alloys have such a large affinity for Fe, the fO_2 buffering capacity of alloy capsules was not investigated by the Medard et al. (2008) study. The current study uses both unjacketed graphite capsules (with an AuPdFe alloy monitor) and all metal (AuPdFe alloy) capsules, along with the experimentally calibrated equilibrium constants and solution

model described above, to measure the fO_2 of piston cylinder experiments performed in barium carbonate pressure assemblies. For experiment ComW-1, the capsule material was analyzed from an experiment reported in Barr et al. (2009). This experiment was performed in an externally heated gas pressure vessel instead of a piston cylinder. The experiment was buffered by a solid Ni-NiO buffer in communication with the sample via an H_2O-rich fluid. This experiment provides an independent evaluation of the results of this fO_2 measurement technique at elevated pressure and under hydrous conditions.

The PtFe alloy studies of Grove (1981) and Medard et al. (2008) used the Fe^{3+} correction procedures of Sack et al. (1980) and Kress and Carmichael (1991), respectively, to calculate the X_{FeO}^{melt}; ($X_{FeO}^{melt} = a_{FeO}^{melt}$). Our Model 1 and Model 2 calculations employ the same X_{FeO}^{melt} correction procedures as used in the corresponding PtFe study. Both Fe^{3+} correction models require knowledge of the fO_2 in order to calculate the X_{FeO}^{melt}. Initially, the calculation of fO_2 for the high pressure experiments was performed assuming $X_{FeO^*}^{melt}$ equaled a_{FeO}^{melt}. The resulting fO_2 was then reused in the Fe^{3+} correction algorithm to recalculate the X_{FeO}^{melt} and thus the fO_2 for the experiment. This was performed five times to minimize the effect of the initial X_{FeO} assumption on the final calculated fO_2.

Calculated values of log fO_2 for the high pressure experiments using Model 1 and Model 2 agree within 0.4 log units (Table 3). The following discussion will only use the values from Model 2 results since it is derived from the most comprehensive PtFe alloy study considered in the present work. The study of Medard et al. (2008) calculated the pressure dependence of the PtFe equilibrium, which can be used to correct back the estimated fO_2 values to 0.0001 GPa (1-atm) where fO_2 buffer reactions are well determined (Model 2[b]; Table 3).

To test the performance of our technique, we analyzed capsule material available from the Barr et al. (2009) study, experiment ComW-1. The estimated log fO_2 for experiment ComW-1, corrected back to 0.0001 GPa, is -6.44, corresponding to NNO +0.30 log units relative to the NNO buffer of Huebner (1971) at the same pressure. This result is consistent with the coexistence of solid Ni and NiO in the buffer capsule, and consistent with the observation that similar experiments sometimes finish with a fully oxidized buffer, only NiO. Additionally, the possible incorporation of a small amount of Pt, from the

buffer capsule, into the Ni metal of the buffer would result in an fO_2 slightly higher than that of the pure buffering assemblage. This indicates that our technique works for hydrous experiments at elevated pressures, however a more extensive study of the pressure limitations of the technique should be the subject of future work.

The graphite capsule experiments in this study exhibit a range of $\log fO_2$ values from CCO – 0.97 to CCO – 3.19, calculated relative to the CCO buffer of Jakobsson and Oskarsson (1994) at the pressure and temperatures of the experiments (Table 3). This agrees with the results of Medard et al. (2008), which showed that graphite capsules maintain the fO_2 of barium carbonate piston cylinder experiments at or below the CCO buffer. The results also illustrate that the buffering capacity of an unjacketed graphite capsule is similar to that of the Pt-jacketed graphite capsules. The discussion of Medard et al. (2008) suggests the possibility that the Pt-jacket could inhibit the escape of gaseous species involved in the buffering reaction (e.g. CO_2), however if this is the case the wide range of fO_2 values obtained in this study would suggest that the loss of these gaseous species would serve to reduce rather than oxidize the experimental charge. Evidence of this possible reduction by gaseous species loss is found in the most reduced of the experiments in this study, B1104, which initially used a hydrated glass + crystals starting material. The experiment ended in an anhydrous state, with an fO_2 below that of the CCO buffer. This illustrates the inability of graphite capsule experiments to oxidize beyond that of the CCO buffer.

The $\log fO_2$ values for the alloy capsule experiments of this study range from CCO – 1.48 to CCO + 1.44 (Table 3). The alloy capsule experiments were all performed using Fe-free AuPd capsules and undersaturated with respect to H_2O. The experiments performed in graphite did not lose Fe to the capsule, and with the exception of B1104, they were performed using anhydrous starting materials. This would suggest that the alloy capsule experiments would be expected to be more oxidized than those performed in graphite capsules for two reasons: 1. The incorporation of Fe into the capsule from the Fe_xO_y species in the melt (Eq. 1) would leave behind excess oxygen in the melt and 2. The loss of hydrogen from the H_2O dissolved in the melt would also leave behind excess oxygen. Both of these processes were observed in each of the alloy capsule experiments in the form of Fe in the alloy and lower dissolved H_2O than initially

present. Experiments B1123, B1128, and B1129 exhibit slightly more oxidized values than those done in the graphite capsules, but they still remain below that of the CCO buffer. The only experimental charge that exhibits an fO_2 above that of the CCO buffer is B1153, with a value of CCO + 1.44. The difference between this experiment and those that remain below the CCO buffer is that it was performed with a crushable MgO ring encircling the charge rather than an unfired pyrophyllite ring. The alloy in experiment B1153 contains only 1.27 mol% Fe, compared to the 1.62 - 2.78 mol% Fe contained in the alloys of the other experiments. Assuming similar internal surface area of the capsules and a constant initial bulk composition, the loss of Fe plays a minor role in the oxidation of these experimental charges. B1153 has a low melt H_2O content, ~1.4 wt% (Table 2), indicating a loss of water as compared to B1123, B1128, and B1129, all of which started with the same amount of water. This loss of water is likely the driving force for the oxidized nature of the experimental charge, due to hydrogen diffusing out of the capsule at a rate greater than that of the oxygen. The pyrophyllite ring used in the other H_2O-undersaturated alloy capsule experiments of this study have been used in past experimental studies of hydrous melts (e.g. Freda et al. 2001), and may either limit the driving force for diffusive loss of hydrogen or act as a source of hydrogen to reduce the silicate experimental charge. If the pyrophyllite is not acting to buffer or reduce the experimental charge, then perhaps the use of graphite furnaces sets the ambient fO_2 of the experimental run assembly to the same conditions as a graphite capsule. When the pyrophyllite is exchanged for MgO, it appears that the fO_2 of AuPd alloy capsules can be increased above that of the CCO buffer and even beyond that of the NNO buffer, suggesting that the ambient fO_2 of the run assembly can be overwhelmed when large quantities of oxygen are produced by loss of hydrogen from experimental charges. Further investigation of other run assemblies (e.g. talc-pyrex) and furnace materials (e.g. $LaCrO_3$) is needed to fully understand what is controlling the ambient redox conditions of alloy capsule piston cylinder experiments. Additionally, experimentation with other materials surrounding the alloy capsules may provide a balance of H_2O retention and fO_2 control, needed to allow investigation of volatile content and redox controls on melting and crystallization.

Conclusions

Combining the excess free energy parameters for the Au-Pd, Pd-Fe and Pd-Au binary solid solutions allows for the calculation of a normal solution model for the ternary alloy system for solid AuPdFe alloys. When the Fe exchange reaction (Eq. 1), between the silicate melt and the alloy, is characterized it does not produce an equilibrium constant similar to that produced by the PtFe binary system, which models the same Fe exchange reaction. By using previous studies of the PtFe alloy system, a temperature dependent misfit parameter can be calculated that brings the ternary alloy model into agreement with the binary alloy models. The new AuPdFe solution model allows for the calculation of fO_2 in high pressure experiments that are performed with AuPdFe capsules in contact with Fe-bearing silicate melts.

Bibliography

Akella J, Kennedy G (1971) Melting of Gold, Silver, and Copper-- Proposal for a New High-Pressure Calibration Scale. J Geophys Res 76:4969-4977

Anderson AT (1974) Chlorine, Sulfur, and Water in Magmas and Oceans. Geol Soc Am Bull 85:1485-1492

Armstrong JT (1995) Citzaf - a package of correction programs for the quantitative Electron Microbeam X-Ray- Analysis of thick polished materials, thin-films, and particles. Microbeam Anal 4:177-200

Barr J A, Till CB, Grove TL (2007) Shallow mantle melting beneath Newberry Volcano, central Oregon, USA. Eos Trans AGU 88(52), Fall Meet. Suppl., Abst V32C-02

Barr JA, Grove TL, Wilson AH (2009) Hydrous komatiites from Commondale, South Africa: An experimental study. Earth Planet Sci Lett 284:199-207

Borisov A, Palme H (2000) Solubilities of noble metals in Fe-containing silicate melts as derived from experiments in Fe-free systems. Am Mineral 85:1665-1673

Boyd FR, England JL (1960) Apparatus for phase equilibrium studies at pressures up to 50 kilobars and temperatures up to 1750 °C. J Geophys Res 65:741-748

Freda C, Baker DR, Ottolini L (2001) Reduction of water loss from gold-palladium capsules during piston-cylinder experiments by use of pyrophyllite powder. Am Min 86:234-237

Fuhrman ML, Lindsley DH (1988) Ternary-feldspar modeling and thermometry. Am Mineral 73:201-215

Gaetani GA, Grove TL (1998) The influence of water on melting of mantle peridotite. Contrib Mineral Petrol 131:323-346

Grove TL (1981) Use of PtFe alloys to eliminate the iron-loss problem in 1 atmosphere gas mixing experiments: Theoretical and practical considerations. Contrib Mineral Petrol 78:298-304

Holzheid A, Palme H, Chakraborty S (1997) The activities of NiO, CoO, and FeO in silicate melts. Chem Geol 139:21-38

Huebner JS (1971) Buffering Techniques for Hydrostatic Systems at Elevated Pressures. In: Ulmer GC (ed) Research Techniques for High Pressure and High Temperature, Springer-Verlag, New York, pp 123-177

Jakobsson S, Oskarsson N (1994) The system C-O in equilibrium with graphite at high pressure and temperature: An experimental study. Geochim Cosmochim Acta 58:9-17

Kägi R, Müntener O, Ulmer P, Ottolini L (2005) Piston-cylinder experiments on H2O undersaturated Fe-bearing systems: An experimental setup approaching fO_2 conditions of natural calc-alkaline magmas. Am Mineral 90:708-717

Kawamoto T, Hirose K (1994) Au-Pd sample containers for melting experiments on iron and water bearing systems. Eur J Mineral 6:381-385

Kessel R, Beckett JR, Stolper EM (2001) Thermodynamic properties of the Pt-Fe system. Am Mineral 86:1003-1014

Kress VC, Carmichael ISE (1991) The compressibility of silicate liquids containing Fe_2O_3 and the effect of composition, temperature, oxygen fugacity and pressure on their redox states. Contrib Mineral Petrol 108:82-92

Médard E, McCammon CA, Barr JA, Grove TL (2008) Oxygen fugacity, temperature reproducibility, and H_2O contents of nominally anhydrous piston-cylinder experiments using graphite capsules. Am Mineral 93:1838-1844

Sack RO, Carmichael ISE, Rivers M, Ghiorso MS (1980) Ferric-Ferrous Equilibria in Natural Silicate Liquids at 1 Bar. Contrib Mineral Petrol 75:369-376

Shaw H (1963) The Four-Phase Curve Sanidine-Quartz-Liquid-Gas Between 500 and 4000 Bars. Am Mineral 48:883-896

Sisson TW, Grove TL (1993) Experimental investigations of the role of H_2O in calc-alkaline differentiation and subduction zone magmatism. Contrib Mineral Petrol 113(2):143-166

Takahashi E, Kushiro I (1983) Melting of a dry peridotite at high pressure and basalt magma genesis. Am Mineral 68:859-879

Thompson JB (1967) Thermodynamic properties of simple solutions. In: Abelson PH (ed) Researches in Geochemistry, vol 2. Wiley, New York, pp 340-361

Tomiska J (1990) Computer-aided Thermodynamics of Solid Au-Pd Alloys by Knudsen Cell Mass Spectrometry and Calculation of the Phase Diagram. Z Metallkde 81:912-918

Appendix

Solution Model Parameters

The following equations were used to determine the values to be used in the solution model (Eq. 2) (Temperature in Kelvin):

$$W_{PdAu} = -8373 - T(-3.488) \quad \text{(Eq. A1)}$$

$$W_{AuPd} = -60900 - T(-24.071) \quad \text{(Eq. A2)}$$

The Margules parameters W^{H}_{AuPd}, W^{S}_{AuPd}, W^{H}_{PdAu}, and W^{S}_{AuPd} where determined by refitting the data of Tomiska (1990) for the Au-Pd alloy binary system.

$$W_{AuFe} = 63051 - T(22.517) \quad \text{(Eq. A3)}$$

$$W_{FeAu} = 68757 - T(56.095) \quad \text{(Eq. A4)}$$

$$W_{PdFe} = 19565 - T(23.124) \quad \text{(Eq. A5)}$$

$$W_{FePd} = -90388 - T(2.386) \quad \text{(Eq. A6)}$$

The Margules parameters for the Au-Fe and Pd-Fe binary alloy systems were taken from the study of Borisov and Palme (2000).

Estimation of the Misfit parameter is outlined in the text. Shown here are the formulations of these parameters used in conjunction with Eq. 2 for of the AuPdFe solution model. As described earlier, Model 1 is based on the correction to the predicted K values (Eq. 4) of the Pt-Fe alloy study of Grove (1981) and Model 2 is based on the correction to the predicted K values (Eq. 4) of the Pt-Fe alloy study of Medard et al. (2008).

Model 1 $$\Delta_{Misfit} = 146986(1000/T) - 105615 \quad \text{(Eq. A7)}$$

Model 2 $$\Delta_{Misfit} = 143095(1000/T) - 102632 \quad \text{(Eq. A8)}$$

Table 1. Compositions of experimental glasses and alloys for 0.0001 GPa experiments with known oxygen fugacity. Glass and alloy totals are the average of actual microprobe analyses, however oxide wt% and alloy mol% are given as normalized to 100%. The summation of the oxide wt% in the glass analyses to a quantity less than 100% represents trace amounts of other elements, e.g. P2O5, that are not reported here. Values to the right of the oxide wt% are 1-sigma variations in the probe analyses. All Fe in glasses analyzed as FeO and reported here as FeO*.

	Experiment	8071-1		8071-2		8071-3		8071-4		8061		8062		109-1b	
	Analyses (glass/alloy)	8 / 11		10 / 5		11 / 15		9 / 15		8 / 5		4 / 10		7 / 8	
Glass Composition (oxide wt%)	SiO_2	58.34	0.28	58.41	0.17	47.81	0.23	48.07	0.30	54.41	0.39	50.93	0.07	52.80	0.28
	TiO_2	0.60	0.03	0.58	0.05	0.61	0.05	0.61	0.05	0.84	0.03	0.73	0.06	2.14	0.08
	Al_2O_3	14.39	0.10	14.40	0.08	18.71	0.15	18.70	0.15	17.46	0.06	17.39	0.09	15.01	0.10
	Cr_2O_3	0.07	0.02	0.08	0.02	0.03	0.03	0.03	0.02	0.04	0.03	0.03	0.02	0.08	0.02
	FeO*	5.48	0.16	5.49	0.10	7.89	0.07	7.86	0.09	2.55	0.06	7.18	0.14	7.42	0.35
	MnO	0.13	0.02	0.15	0.02	0.18	0.03	0.17	0.01	0.10	0.02	0.12	0.02	0.19	0.02
	MgO	9.16	0.14	9.05	0.08	10.51	0.11	10.57	0.17	11.44	0.12	11.32	0.06	7.61	0.12
	CaO	8.15	0.14	8.09	0.07	11.66	0.08	11.62	0.12	12.10	0.13	11.53	0.29	11.38	0.13
	Na_2O	3.04	0.09	3.14	0.11	2.46	0.11	2.25	0.17	0.66	0.07	0.53	0.05	3.19	0.12
	K_2O	0.56	0.02	0.53	0.01	0.10	0.01	0.08	0.01	0.41	0.01	0.23	0.01	0.18	0.01
	Total	98.88		99.57		99.72		99.51		99.65		99.94		100.52	
	Mg#	0.75		0.75		0.70		0.71		0.89		0.74		0.65	
Alloy (mol%)	Au	69.18	0.44	69.48	0.35	69.32	0.31	69.45	0.27	54.89	0.24	60.75	0.17	68.05	0.16
	Pd	30.59	0.43	30.23	0.36	30.31	0.30	30.23	0.27	31.98	0.16	30.93	0.18	29.55	0.16
	Fe	0.23	0.03	0.29	0.05	0.37	0.07	0.32	0.06	13.13	0.15	8.32	0.10	2.40	0.05
	Total	100.05		100.65		100.16		99.97		98.83		100.58		100.61	
Temperature (°C)		1300		1300		1300		1300		1235		1235		1180	
log $fO2$		-5.511		-5.511		-5.511		-5.511		-11.230		-9.760		-9.283	
Duration (h)		50		50		50		50		99		140		124	

Table 1. cont.

	Experiment	109-1c		109-2c		109-2d		ECap 2		ECap 5		ECap 6		ECap 8	
	Analyses (glass/alloy)	6 / 9		7 / 9		5 / 7		6 / 7		5 / 6		6 / 7		6 / 6	
Glass Composition (oxide wt%)	SiO_2	53.05	54.85	0.32	55.10	0.06	49.70	0.11	50.48	0.08	49.81	0.30	60.65	0.39	0.28
	TiO_2	2.48	1.83	0.09	1.83	0.12	0.56	0.06	0.71	0.06	0.57	0.06	0.67	0.07	0.08
	Al_2O_3	14.63	17.16	0.07	17.16	0.14	19.14	0.08	18.65	0.07	19.22	0.07	15.63	0.07	0.10
	Cr_2O_3	0.08	0.07	0.02	0.07	0.01	0.03	0.02	0.02	0.02	0.03	0.01	0.01	0.01	0.02
	FeO*	7.02	2.21	0.03	2.28	0.07	4.73	0.10	4.50	0.04	4.59	0.13	3.69	0.07	0.35
	MnO	0.24	0.16	0.03	0.16	0.02	0.12	0.01	0.13	0.03	0.11	0.01	0.07	0.02	0.02
	MgO	7.93	8.40	0.04	8.43	0.12	11.08	0.07	10.92	0.13	11.16	0.15	5.88	0.09	0.12
	CaO	11.12	11.84	0.19	11.65	0.48	12.19	0.08	12.23	0.09	12.22	0.12	8.85	0.06	0.13
	Na_2O	3.19	3.33	0.12	3.18	0.11	2.28	0.21	2.20	0.07	2.18	0.09	3.61	0.16	0.12
	K_2O	0.25	0.15	0.00	0.15	0.01	0.16	0.00	0.15	0.01	0.11	0.01	0.94	0.02	0.01
	Total	100.52	100.68		100.31		99.85		99.90		99.85		100.29		
	Mg#	0.67	0.87		0.87		0.81		0.81		0.81		0.74		
Alloy (mol%)	Au	67.99	64.02	0.29	65.88	0.36	67.95	0.17	66.06	0.24	67.16	0.21	83.62	0.09	0.16
	Pd	29.97	31.25	0.21	30.26	0.13	30.39	0.13	29.81	0.24	30.40	0.22	15.94	0.10	0.16
	Fe	2.05	4.73	0.23	3.86	0.25	1.66	0.06	4.13	0.02	2.44	0.04	0.44	0.02	0.05
	Total	100.31	100.27		99.95		98.64		98.75		98.51		98.80		
Temperature (°C)		1180		1215		1215		1270		1250		1250		1158	
				-		-									
log $fO2$		-9.283		10.162		10.162		-7.657		-9.134		-8.472		-8.876	
Duration (h)		124		95		95		48		86		90		87	

Table 2. Compositions of high-pressure experimental glasses and alloys of unknown oxygen fugacity. All Fe in glasses analyzed as FeO and reported here as FeO*.

	Experiment	ComW-1[a]		B1099[b]		C405[b]		B1104[b]		B1123[c]		B1128[c]	
	Analyses (glass/alloy)	5 / 10		11 / 4		5 / 9		8 / 8		11 / 6		8 / 6	
Glass Composition (oxide wt%)	SiO_2	52.50	0.10	49.71	0.11	56.00	0.24	50.34	0.24	64.19	0.28	55.20	0.33
	TiO_2	0.10	0.04	0.63	0.06	0.87	0.07	1.07	0.10	0.36	0.04	1.41	0.07
	Al_2O_3	11.20	0.20	20.10	0.09	21.16	0.10	15.88	0.13	18.83	0.17	20.80	0.14
	Cr_2O_3	0.21	0.02	0.03	0.01	0.01	0.01	0.02	0.02	0.00	0.01	0.03	0.02
	FeO*	4.55	0.22	4.14	0.08	5.93	0.15	3.36	0.10	2.03	0.03	2.33	0.10
	MnO	0.13	0.02	0.14	0.02	0.09	0.01	0.07	0.02	0.10	0.03	0.11	0.02
	MgO	19.40	0.10	9.27	0.10	4.60	0.16	11.95	0.14	1.43	0.03	5.47	0.22
	CaO	6.58	0.17	11.56	0.08	7.07	0.17	11.56	0.10	2.76	0.17	6.64	0.21
	Na_2O	0.28	0.06	3.49	0.15	5.20	0.10	3.83	0.14	2.99	0.12	3.59	0.12
	K_2O	0.01	0.01	0.11	0.01	0.21	0.01	1.10	0.02	2.56	0.05	1.56	0.03
	Total	94.93		99.18		101.14		99.72		95.81		97.92	
	H_2O (wt%)	5.04		n/a		n/a		n/a		4.19		2.08	
Alloy (mol%)	Au	69.42	0.23	61.12	0.15	65.45	0.35	56.87	0.24	82.81	0.25	81.79	0.06
	Pd	30.20	0.20	26.95	0.18	29.21	0.29	24.87	0.18	15.57	0.24	15.86	0.08
	Fe	0.38	0.05	11.94	0.04	5.34	0.08	18.26	0.17	1.62	0.04	2.35	0.08
	Total	100.11		100.79		100.18		100.76		100.38		100.32	
	Capsule	$Au_{80}Pd_{20}$		Graphite		Graphite		Graphite		$Au_{90}Pd_{10}$		$Au_{90}Pd_{10}$	
	Temperature (°C)	1275		1300		1300		1180		1100		1200	
	Duration (h)	3		52		50		21		25		23	
	Pressure (GPa)	0.2		1.0		2.0		1.0		1.0		1.0	

Table 2. cont.

	Experiment	B1129[c]		B1153[d]	
	Analyses (glass/alloy)		8 / 13		
Glass Composition (oxide wt%)	SiO_2	49.14	0.66	50.34	0.24
	TiO_2	2.22	0.19	1.07	0.10
	Al_2O_3	17.31	0.12	15.88	0.13
	Cr_2O_3	0.02	0.02	0.02	0.02
	FeO*	10.15	0.43	3.36	0.10
	MnO	0.17	0.03	0.07	0.02
	MgO	4.93	0.11	11.95	0.14
	CaO	6.09	0.40	11.56	0.10
	Na_2O	4.15	0.19	3.83	0.14
	K_2O	2.88	0.10	1.10	0.02
	Total	98.62		99.72	
	H_2O (wt%)	1.38		n/a	
Alloy (mol%)	Au	68.85	0.18	56.87	0.24
	Pd	29.89	0.18	24.87	0.18
	Fe	1.27	0.10	18.26	0.17
	Total	100.28		100.76	
	Capsule	$Au_{80}Pd_{20}$		$Au_{80}Pd_{20}$	
	Temperature (°C)	1175		1200	
	Duration (h)	27		28	
	Pressure (GPa)	1.2		1.0	

[a] Alloy capsule analyzed from experiment performed as a part of the study by Barr et al., 2009. This experiment was buffered by Ni-NiO under H_2O saturated conditions. H_2O measured by ion-microprobe, see Barr et al., 2009.

[b] Graphite capsules were used with a bead of AuPd packed inside with the sample powder.

[c] Experiments were performed H_2O undersaturated. H_2O contents calculated by difference assuming 100% glass total.

[d] Experimental capsule encircled by MgO instead of Pyrophyllite

Table 3. Calculated oxygen fugacities for high-pressure experiments.

Experiment	ComW-1	B1099	C405	B1104	B1123	B1128	B1129	B1153
Capsule	$Au_{80}Pd_{20}$	Graphite	Graphite	Graphite	$Au_{90}Pd_{10}$	$Au_{90}Pd_{10}$	$Au_{80}Pd_{20}$	$Au_{80}Pd_{20}$
	Calculated log fO_2							
$X_{FeO^*}^{melt} = a_{FeO}^{melt}$ (no Fe^{3+} correction)								
Model 1	-6.64	-10.25	-8.73	-12.97	-11.95	-10.39	-9.97	-8.12
Model 2[a]	-6.25	-9.83	-8.31	-12.68	-11.77	-10.08	-9.69	-7.81
Model 2[b]	-6.34	-10.28	-9.21	-13.17	-12.28	-10.57	-10.28	-8.29
$X_{FeO}^{melt} = a_{FeO}^{melt}$ (stable iterative solution using Fe^{3+} correction models[c])								
Model 1	-6.74	-10.27	-8.79	-12.99	-12.00	-10.44	-10.04	-8.25
Model 2[a]	-6.35	-9.84	-8.33	-12.69	-11.78	-10.11	-9.72	-7.87
Model 2[b]	-6.44	-10.29	-9.23	-13.18	-12.30	-10.58	-10.31	-8.34
ΔCCO[c]								
Model 1	2.79	-1.82	-1.43	-3.48	-1.69	-1.12	-0.72	1.06
Model 2[a]	3.18	-1.40	-0.97	-3.19	-1.48	-0.79	-0.41	1.44
ΔQFM[d]								
Model 2[b]	1.18	-2.93	-1.87	-4.47	-2.55	-2.11	-1.53	0.13
ΔNNO[d]								
Model 2[b]	0.30	-3.80	-2.74	-5.38	-3.50	-3.02	-2.45	-0.78

[a] Ln K value not back corrected for pressure

[b] Ln K value corrected back to 0.0001 GPa using the correction term in Equation 4 of Medard et al. (2008)

[c] Stable fO_2 calculation relative to the buffer curve at experimental conditions (Jakobsson and Oskarsson, 1994)

[d] Stable fO_2 calculation relative to the buffer curve at 0.0001 GPa (Heubner, 1971)

[c] Fe^{3+} correction uses the Sack et al. (1980) algorithm for the Model 1 and the Kress and Carmichael (1991) algorithm for Model 2. These are the same melt correction models used by the PtFe alloy studies, from which the corresponding Δ_{misfit} parameters were determined (Grove (1981) for Model 1 and Medard et al. (2008) for Model 2).

Figure Captions

Figure 1. Shown are alloy compositions of the experiments measured in this study. The line represents the effect of adding Fe to the original $Au_{80}Pd_{20}$ (wt%) alloy, thus diluting the percentage of Au and Pd, assuming no partitioning of either elements in the silicate melt. The data points lying far from the line (above for Au and below for Pd) are alloy compositions for experiments starting with $Au_{90}Pd_{10}$ (wt%) alloys. The strong correlation with the predicted dilution line illustrates the similarly incompatible nature of Au and Pd in silicate melts, and allows for the prediction of the X_{Fe} content of an alloy based on the calculated a_{Fe} of the alloy.

Figure 2. **a** Linear regression of the low-pressure experiments produces a strong correlation. These points are calculated using solution model with no Δ_{misfit} (Eq. 2). Using the temperatures of these experiments and the fitting equations of two PtFe alloy studies (Grove 1981 and Medard et al. 2008), the resulting ln K values are displayed. The line fit to the AuPdFe data has a distinct and different trend than the trends of the PtFe studies. **b** Shown are the low-pressure calibration experiments, recalculated using a solution model that includes a Δ_{misfit} parameter. The Δ_{misfit} was calculated relative to the models of Grove (1981), Model 1 of this study, and Medard et al. (2008), Model 2 of this study. See text for further discussion.

Figure 3. With the inclusion of the Δ_{misfit} parameter, the solution model described herein can be used to calculate the a_{Fe} for an alloy based on the X_{Fe} in the alloy and the composition of the starting alloy (see Figure 1). Shown here are the results of this calculation at three different temperatures and four different starting alloy compositions (note that the alloy compositions are given in wt% values). It is important to notice that the scale of the X_{Fe} axis is preserved through the three plots; however, the scale of the a_{Fe} axis changes due to the strong temperature dependence of the a_{Fe} for a given alloy starting composition.

Figure 1.

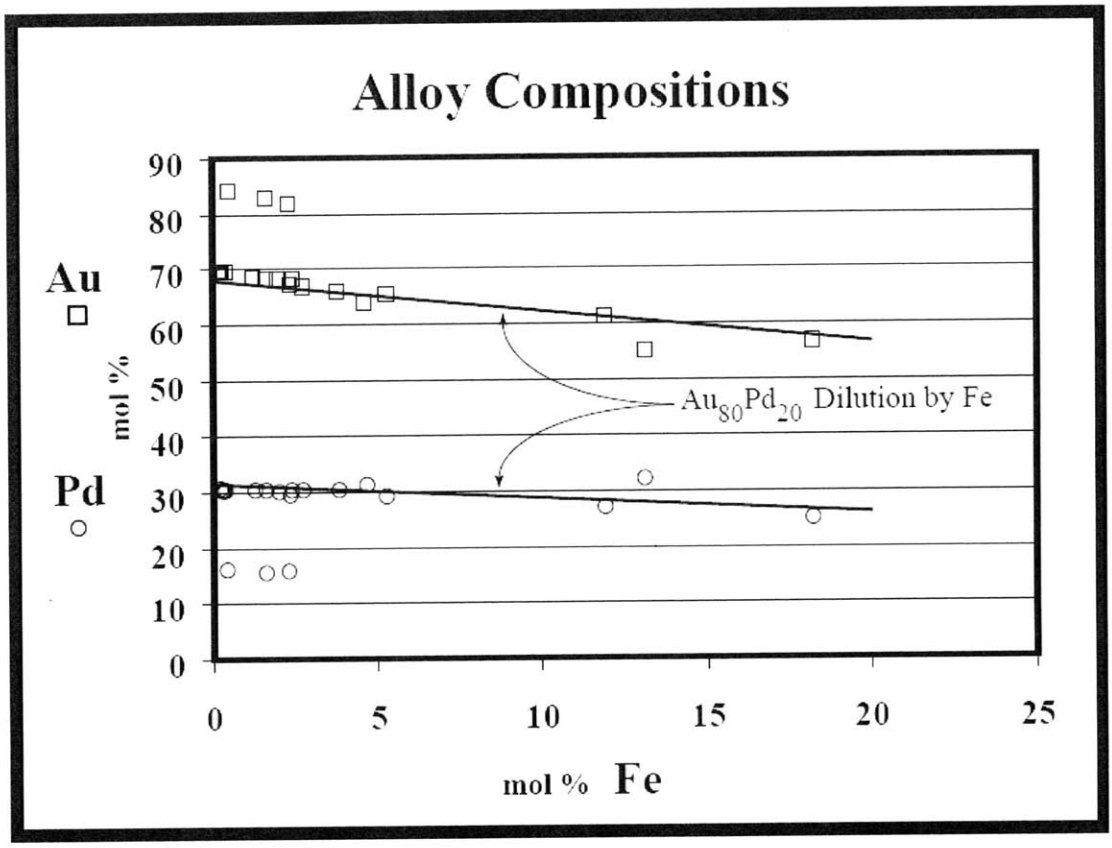
Alloy Compositions
Au
Pd
mol %
90
80
70
60
50
40
30
20
10
0
0
5
10
15
20
25
mol % Fe
$Au_{80}Pd_{20}$ Dilution by Fe

Figure 2.

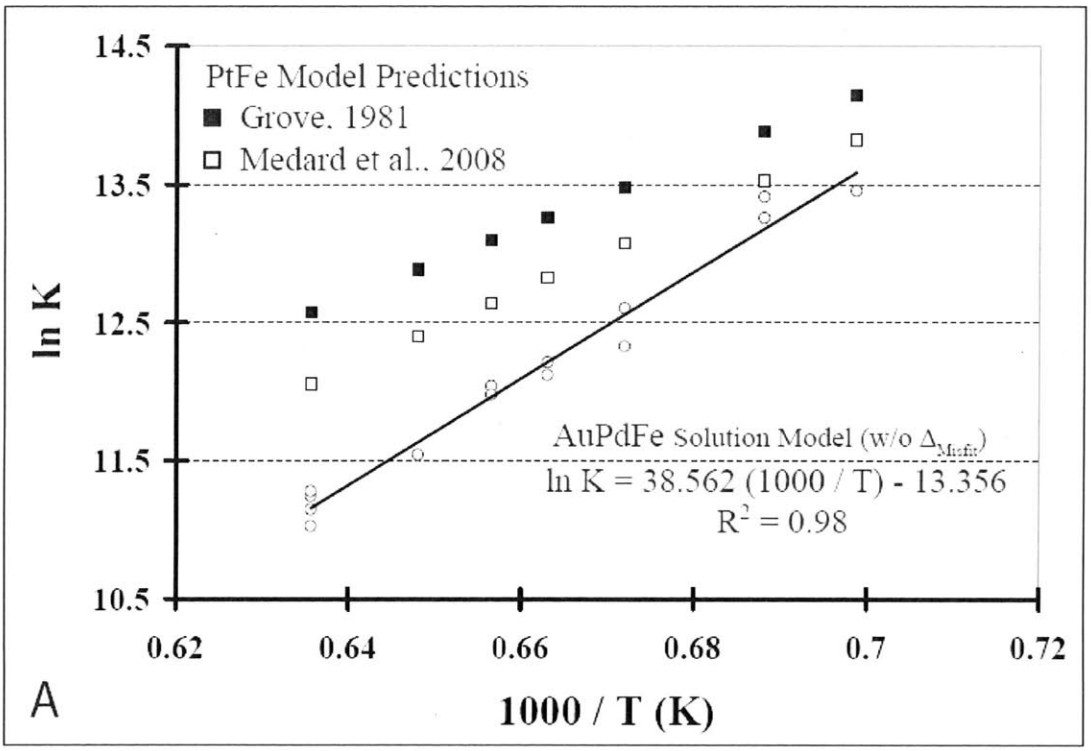
14.5
13.5
12.5
11.5
10.5
ln K
PtFe Model Predictions
Grove, 1981
Medard et al., 2008
AuPdFe Solution Model (w/o Δ_{Misfit})
ln K = 38.562 (1000 / T) - 13.356
R^2 = 0.98
0.62
0.64
0.66
0.68
0.7
0.72
1000 / T (K)
A

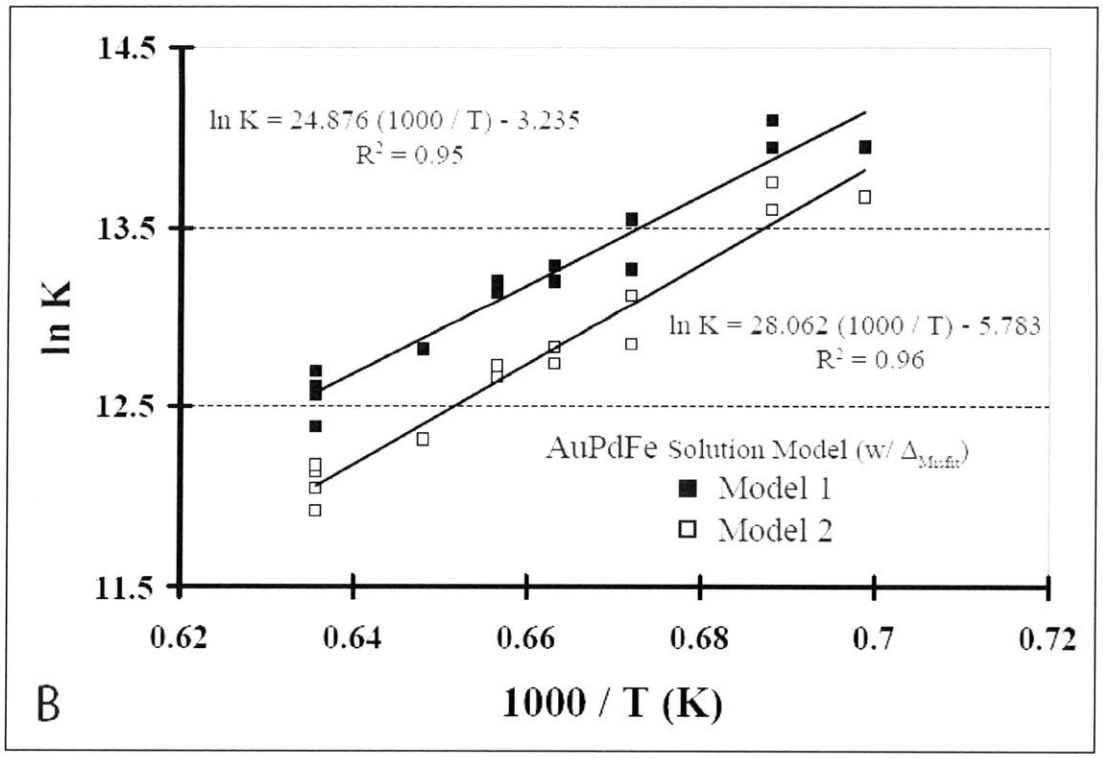
14.5
13.5
12.5
11.5
ln K
ln K = 24.876 (1000 / T) - 3.235
R^2 = 0.95
ln K = 28.062 (1000 / T) - 5.783
R^2 = 0.96
AuPdFe Solution Model (w/ Δ_{Misfit})
Model 1
Model 2
0.62
0.64
0.66
0.68
0.7
0.72
1000 / T (K)
B

Figure 3.

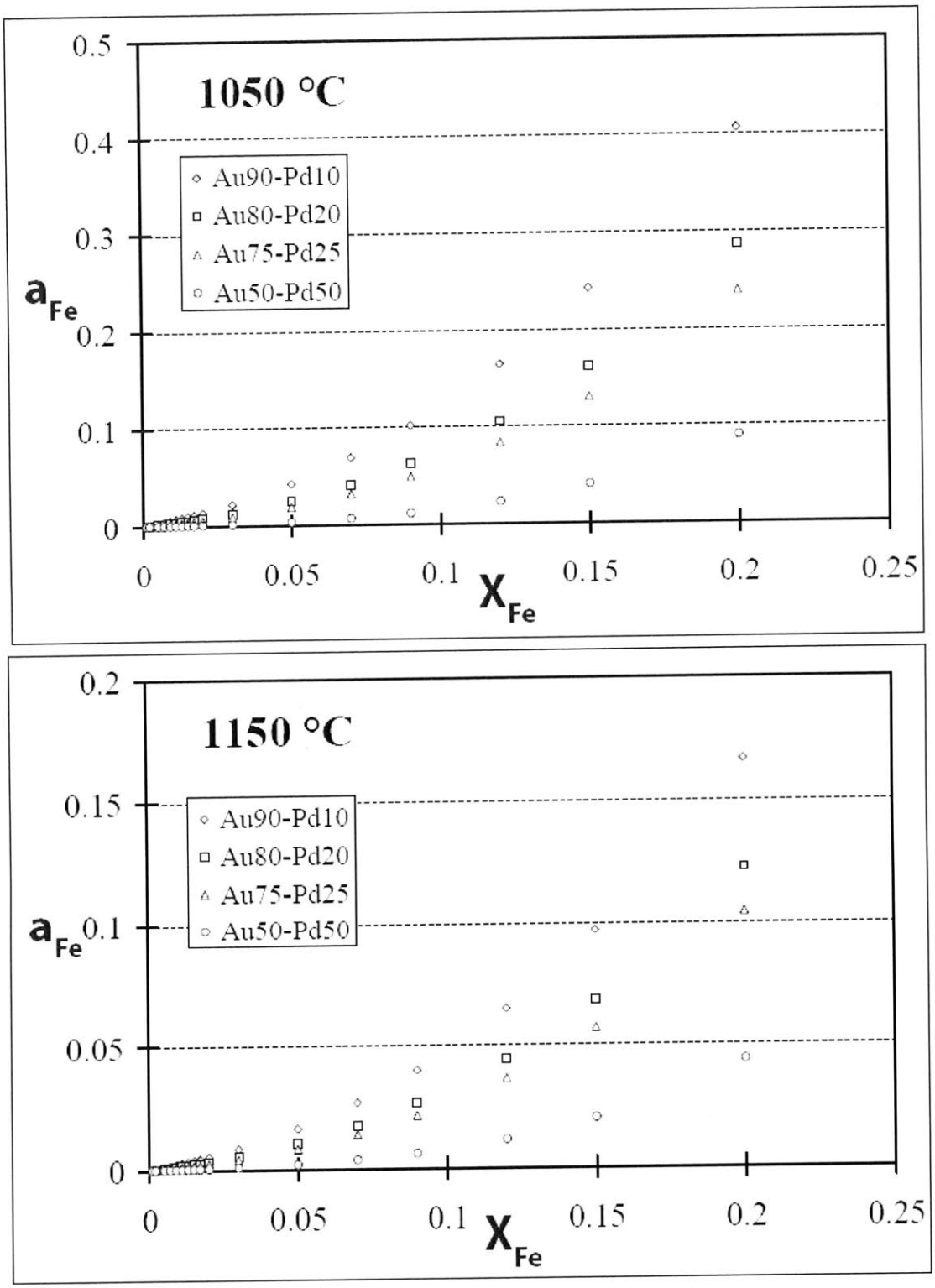
1050 °C
Au90-Pd10
Au80-Pd20
Au75-Pd25
Au50-Pd50
a_{Fe}
X_{Fe}
0.5
0.4
0.3
0.2
0.1
0
0.05
0.15
0.25
1150 °C
Au90-Pd10
Au80-Pd20
Au75-Pd25
Au50-Pd50
a_{Fe}
X_{Fe}
0.2
0.15
0.1
0.05
0
0.05
0.15
0.25

Figure 3. cont.

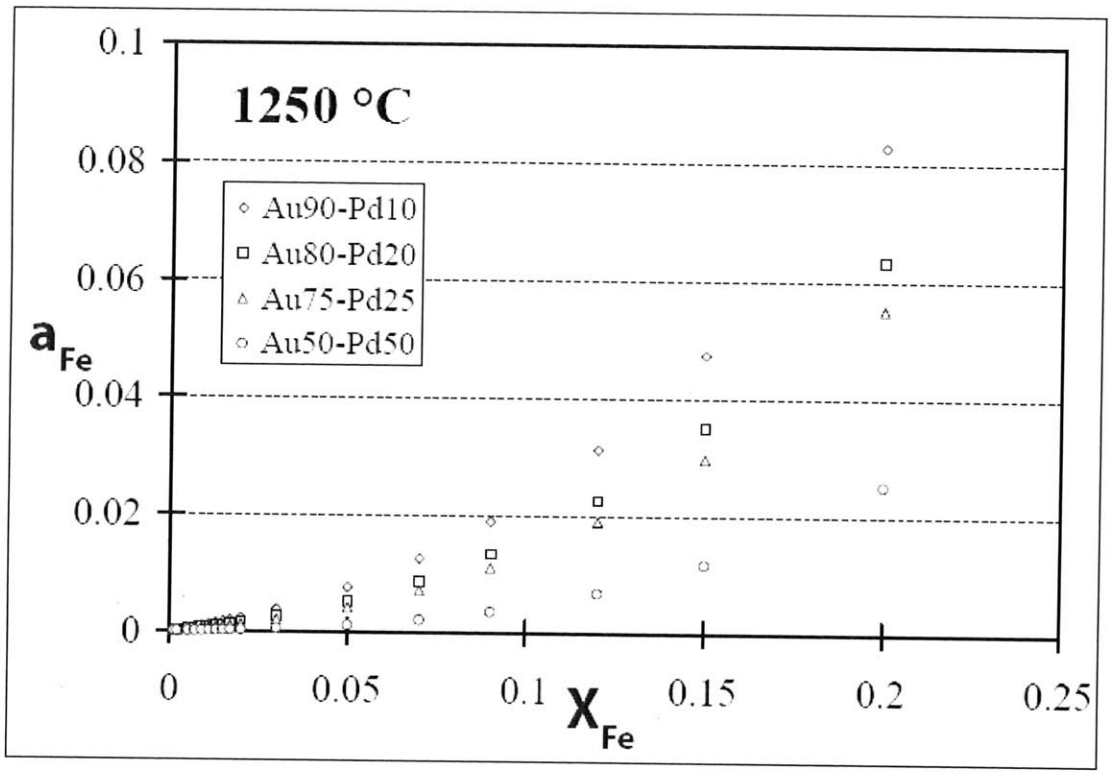

Chapter 5: Kansas Dinosaur Bone Discovery and Evidence of Shark Scavenging

Abstract

During the Barr Expedition of 2009 to Gove County, Kansas a solitary bone was discovered in the lower Smoky Hill Chalk member of the Niobrara Formation. This bone includes traces of scavenging marks thought to have been made by two variety of shark, Cretoxyrhina and Pseudocorax. Preserved embedded in one end of the bone is the tip of a shark tooth thought to be from a *Cretoxyrhina mantelli*. This bone has been identified as the fibula of *Niobrarasaurus coleii*, and represents the first dinosaur find in Kansas with direct physical evidence of shark scavenging on remains of terrestrial dwelling animals, and only the 9th identified find of dinosaur material in the Smoky Hill Chalk of Kansas.

Introduction

Remains of dinosaurs have been previously discovered in Kansas, including a substantial portion of an ankylosaurian dinosaur Niobrarasaurus coleii (e.g. Sternberg, 1909 and Carpenter et al. 1995). To date only eight other specimens of dinosaur remains have been identified from the chalkbeds of western Kansas (Everhart and Ewell, 2006 and Everhart, M.J. pers. comm). These animals are thought to have died near the shoreline of the western interior seaway, where their bodies could be carried out to sea by the rising tide after their carcasses blaoated. These carcasses eventually came to rest on the seafloor and were preserved in the marine sedimentary sequences of western Kansas.

Marks left by *Cretoxyrhina mantelli* have been found on bones of mosasaurs found in the Niobrara Formation of Kansas, including direct evidence in the way of tooth fragments embedded within mosasaur bones themselves (Rothschild et al., 2005). Evidence of scavenging by C. mantelli on the remains of dinosaurs was speculated by Everhart and Hamm (2005), however no direct evidence of the shark involved was preserved in their spefimen. Direct evidence of the *C. mantelli* scavenging the remains of floating dinosaurs has never been documented until this report.

The Bone

Figure 1 is a photograph of the fibula of *Niobrarasaurus coleii* found during the Barr Expedition of 2009. Figure 2 is a close up view of the shaft of the fibula. Visible along and across the long axis of the bone are scratches that are thought to have been made by two varieties of shark based upon the sizes of the marks. The smaller scratches are thought to have been made by *Squalicorax sp.* and the larger ones are thought to have been made by *Cretoxyrhina mantelli.* Visible in Figure 3. is the cross section of the tooth fragment, identified as *Cretoxyrhina mantelli*, that is embedded in the bone.

The Location

The specimen in this report was found in the lower Smoky Hill Chalk of southeastern Gove County, Kansas. The chalk outcrop in which the bone was discovered is small and difficult to determine the precise stratigraphic location, however based on faunal occurrences in the outcrop the location is determined to be in the lower most Smoky Hill Chalk, of Coniacian age (Hattin, 1982). These fauna include occurrence of *Protosphyreana sp.*, *Volviceramus grandis* and fragments of *Durania maxima.*

Bibliography

Carpenter, K., Dilkes, D., Weishampel, D. B., 1995. The dinosaurs of the Niobrara Chalk Formation (upper Cretaceous Kansas). J. Vert. Paleo. 15, 275-297.

Everhart, M.J., Ewell, K., 2006. Shark-bitten dinosaur (Hadrosauridae) vertebrae from the Niobrara Chalk (Upper Coniacian) of western Kansas. Kansas Academy of Science, Trans. 109(1/2), 27-35.

Everhart, M.J., Hamm, S.A., 2005. A new nodosaur specimen (Dinosauria: Nodosauridae) from the Smoky Hill Chalk (Upper Cretaceous) of western Kansas. Kansas Academy of Science, Trans. 108 (1/2), 15-21.

Hattin, D.E., 1982. Stratigraphy and depositional environment of the Smoky Hill Chalk Member, Niobrara Chalk (Upper Cretaceous) of the type area, western Kansas. Kansas Geological Survey Bull. 225, 108 pp.

Rothschild, B.M., Martin, L.D., Schulp, A.S., 1995. Sharks eating mosasaurs, dead or alive?. Neatherlands J. Geosciences. 84, 335-340.

Sternberg, C.H., 1909. An armored dinosaur from the Kansas chalk. Kansas Academy of Science, Trans. 22, 257-258

Figure Captions

Figure 1. Two images of the *Niobrarasaurus coleii* fibula. The bone was found in place with a large crack between the two sections that had infilled with ~2mm of chalk sediment. This crack was repaired using a thick acetone soluable, completely reversible glue.

Fiugre 2. Negative photographic image of a close up of the shaft of the fibula near the repair documented in Figure 1. Large and small scratches concordant and discordant with the long dimension of the bone are traces of scavenging by sharks.

Figure 3. The circle indicates the location of the tip of a *Cretoxyrhina mantelli* tooth was found embedded in the bone at the proximal end of the fibula. The tooth fragment is 0.5 cm in the long dimension. This end of the bone also shows evidence of having been partially digested in the stomach of the shark.

Figure 1.

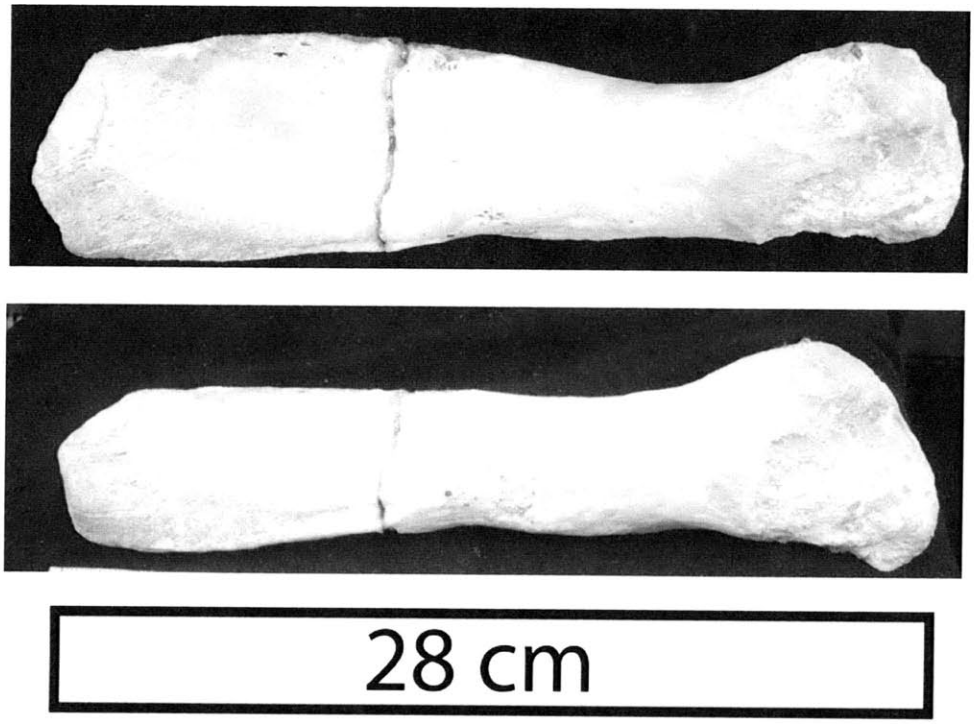

Figure 2.

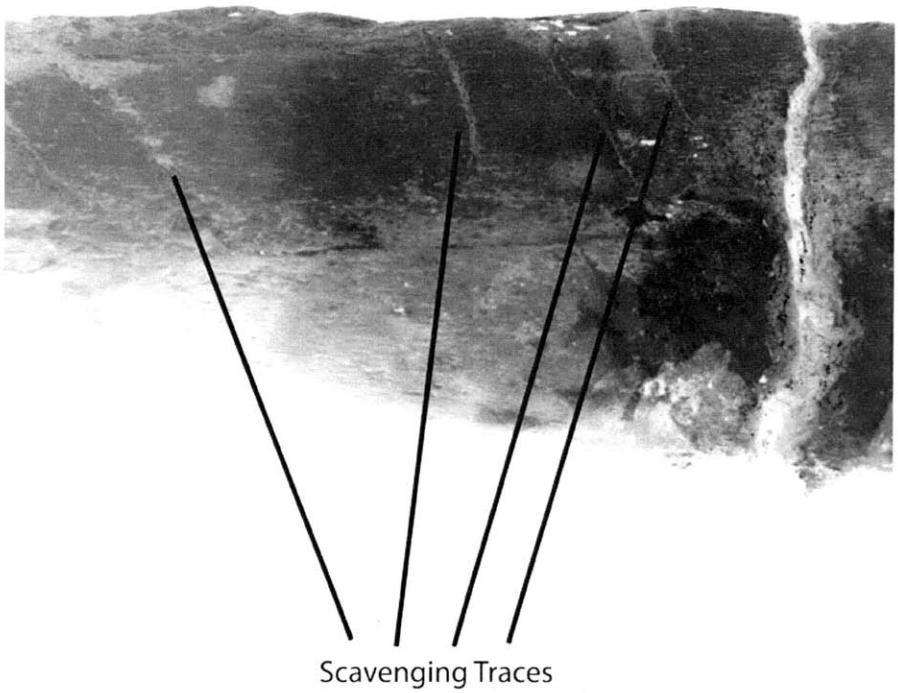

Figure 3.